TAMPEREEN TEKNILLINEN YLIOPISTO
TAMPERE UNIVERSITY OF TECHNOLOGY

Tero-Petri Ruoko

Charge Carrier Dynamics in Solar Water Oxidation

Julkaisu 1473 • Publication 1473

Tampere 2017

Tampereen teknillinen yliopisto. Julkaisu 1473
Tampere University of Technology. Publication 1473

Tero-Petri Ruoko

Charge Carrier Dynamics in Solar Water Oxidation

Thesis for the degree of Doctor of Science in Technology to be presented with due permission for public examination and criticism in Rakennustalo Building, Auditorium RG202, at Tampere University of Technology, on the 24th of May 2017, at 12 noon.

Tampereen teknillinen yliopisto - Tampere University of Technology
Tampere 2017

ISBN 978-952-15-3951-0 (printed)
ISBN 978-952-15-3955-8 (PDF)
ISSN 1459-2045

Abstract

The search for sustainable energy sources is one of the greatest problems facing mankind in the 21st century. Most renewable sources do not have adequate potential to cover the growing need for energy in order to sustain economic and population growth. Solar power is a plausible way to fully cover mankind's continuously growing need for energy. However, sunlight is diurnal, and the amount of sunlight received at different latitudes of the Earth varies drastically. Harnessing solar energy into chemical bonds is an attractive approach to enable the storage of energy for transportation and later use. Direct photoelectrochemical water splitting produces only oxygen and hydrogen, of which hydrogen can be used to sustain a possible hydrogen based economy. The materials used in this Thesis are metal oxide semiconductors that act as photoanodes, performing the water oxidation reaction on their surface and supplying electrons for the water reduction reaction.

Hematite is an n-type metal oxide semiconductor that has a band gap suitable for the absorption of a noticeable fraction of solar radiation. The absorption of light leads to the generation of electron-hole pairs that are separated due to a built-in electric field. However, the conduction band level of hematite is not suitable for unassisted water splitting and it suffers from poor intrinsic charge transport properties. For this reason the photoanodes studied in this Thesis have been modified with doping and by forming heterojunctions with other metal oxide semiconductors, namely titanium dioxide.

This Thesis studies the evolution of the primary charge carriers responsible for water splitting in modified hematite photoanodes. The method selected to probe the charge carrier dynamics is transient absorption spectroscopy that enables the monitoring of charge carriers from the subpicosecond timescale up to seconds. The measurements were performed in a three electrode photoelectrochemical cell to see the effects of additional bias voltage on the charge carrier dynamics and how the recombination and oxygen evolution reaction are changed when a photocurrent is generated.

The results of this Thesis indicate that the modification of hematite has a profound effect on the charge carrier behaviour. The observed effects range from changes in recombination on the picosecond timescale, to nanosecond timescale trapping of electrons into intraband or surface states, and all the way to changes in the reaction rates of long-lived holes in the hundreds of milliseconds timescale.

Preface

The research presented in this Thesis was carried out in the Laboratory of Chemistry and Bioengineering at Tampere University of Technology (TUT) during the years 2013 – 2016. I would like to kindly acknowledge The European Union FP7 project SOLAROGENIX (NMP4-SL-2012-310333) for financially supporting this research.

I would like to thank my supervisor Prof. Nikolai Tkachenko for his guidance on optical spectroscopy and for allowing me the necessary academic freedom to grow as a researcher while finishing this work. I would also like to sincerely thank my original supervisor Prof. Helge Lemmetyinen for allowing me to begin my research career under his guidance, a fact that will surely be of great influence during my whole research career. My sincere gratitude goes to Dr. Kimmo Kaunisto, whose input regarding the research and writing was of paramount importance. I would also like to extend my personal gratitude to SOLAROGENIX project coordinator Prof. Dr. Sanjay Mathur for inviting me to visit his excellent research group at the University of Cologne

I am grateful to all of the people at the chemistry laboratory for the pleasant working atmosphere. I want to thank everybody from the lunch group, especially Kirsi Virkki, Venla Manninen, and Arto Hiltunen, for the peer support I needed when the research and Thesis writing was not going as planned.

I want to thank my family for their constant support and love during these years. I thank my parents for their support that was extremely important during my studies. Finally, my sincerest gratitude goes to my wife Liisa and our two beautiful children, Sointu and Tempo, for enabling me to forget the negative sides of research every single day.

Tampere, May 2017

Tero-Petri Ruoko

Contents

Abbreviations and symbols

APCE	Absorbed photon-to-current efficiency
BER	Back-electron recombination
CVD	Chemical vapor deposition
FTO	Fluorine doped tin dioxide
FWHM	Full width at half maximum
HER	Hydrogen evolution reaction
IPCE	Incident photon-to-current efficiency
ITO	Indium tin oxide
Nd:YAG	Neodymium-doped yttrium aluminium garnet
Nd:YLF	Neodymium-doped yttrium lithium fluoride
Nd:YVO_4	Neodymium-doped yttrium vanadate
OER	Oxygen evolution reaction
OPA	Optical parametric amplifier
PEC	Photoelectrochemical
PECVD	Plasma-enhanced chemical vapor deposition
RHE	Reference hydrogen electrode
SEI	Semiconductor-electrolyte interface
SEM	Scanning electron microscopy
STH	Solar-to-hydrogen
TCO	Transparent conducting oxide
Ti:Al_2O_3	Titanium doped sapphire, also Ti:sapphire
XPS	X-ray photoelectron spectroscopy
XRD	X-ray diffraction

α	Absorption coefficient
α^{-1}	Light penetration depth
λ	Wavelength of light
λ_{re}	Reorganization energy
η	Efficiency
τ	Lifetime
$\tau_{1/2}$	Half-life
$\Phi_{\mathrm{H_2}}$	Hydrogen generation rate
A	Absorbance, optical density
ΔA	Change in absorbance
c	Speed of light
d	Thickness
e	Euler's number
E	Energy

ΔE	Width of electron transfer probability distribution
E°	Standard electrode potential
E°_{cell}	Standard potential for a redox reaction
G°_{f,H_2}	Gibbs free energy of hydrogen formation
ΔG°	Gibbs free energy change
h	Planck constant
I	Light intensity
ΔI	Change in light intensity
J	Current density
J_{ph}	Photocurrent density
k	Rate constant
$\overline{\mathbf{k}}$	Wave vector
P_{light}	Illumination power density
q	Elementary charge
R	Reflectance
T	Transmittance
V	Voltage
V_{bias}	Bias voltage
V_{redox}	Voltage associated with an electrochemical cell reaction

List of Publications

Paper I Tero-Petri Ruoko, Kimmo Kaunisto, Mario Bärtsch, Juuso Pohjola, Arto Hiltunen, Markus Niederberger, Nikolai V. Tkachenko, and Helge Lemmetyinen, "Subpicosecond to second time-scale charge carrier kinetics in hematite–titania nanocomposite photoanodes", *Journal of Physical Chemistry Letters*, vol. 6, no. 15, pp. 2859–2864, 2015

Paper II Davide Barreca, Giorgio Carraro, Alberto Gasparotto, Chiara Maccato, Michael E. A. Warwick, Kimmo Kaunisto, Cinzia Sada, Stuart Turner, Yakup Gönüllü, Tero-Petri Ruoko, Laura Borgese, Elza Bontempi, Gustaaf Van Tendeloo, Helge Lemmetyinen, and Sanjay Mathur, "Fe_2O_3–TiO_2 nano-heterostructure photoanodes for highly efficient solar water oxidation", *Advanced Materials Interfaces*, vol. 2, no. 17, p. 1500313, 2015

Paper III Ali Kaouk, Tero-Petri Ruoko, Yakup Gönüllü, Kimmo Kaunisto, Andreas Mettenbörger, Evgeny Gurevich, Helge Lemmetyinen, Andreas Ostendorf, and Sanjay Mathur, "Graphene-intercalated Fe_2O_3/TiO_2 heterojunctions for efficient photoelectrolysis of water", *RSC Advances*, vol. 5, iss. 123, pp. 101401–101407, 2015

Paper IV Ali Kaouk, Tero-Petri Ruoko, Myeongwhun Pyeon, Yakup Gönüllü, Kimmo Kaunisto, Helge Lemmetyinen, and Sanjay Mathur, "High water-splitting efficiency through intentional In and Sn codoping in hematite photoanodes", *The Journal of Physical Chemistry C*, vol. 120, no. 49, pp. 28345–28353, 2016

Author contribution

The author was responsible for planning, performing, and interpreting the photodynamic studies in all four publications. The author also built the optical setup of the flash-photolysis transient absorption system that was used in **Paper I**, **Paper II**, and **Paper IV**. The author also took part in sample design and preparation in **Paper III** and **Paper IV**.

The author was the main author in **Paper I**, responsible for the transient absorption spectroscopy and charge transport section in **Paper II**, and a shared main author in **Paper III** and **Paper IV**. Ali Kaouk, the other main author in **Paper III** and **Paper IV**, was responsible for sample preparation and material characterization in both publications. All coauthors contributed to the realization of the research in each publication.

The work was performed under the supervision of Prof. Helge Lemmetyinen in all publications and also Prof. Dr. Sanjay Mathur in **Paper III** and **Paper IV**. The contributions of the author are illustrated in the Table below.

Summary of the contributions of the author to the publications included in this Thesis.

Publication	Research design	Photodynamic study	Manuscript preparation
Paper I	70 %	90 %	100 %
Paper II	30 %	80 %	40 %
Paper III	50 %	100 %	50 %
Paper IV	70 %	100 %	70 %

1 Introduction

Mankind consumed 110 petawatthours of energy in 2014.[1] The energy consumption has been estimated to more than double by 2050 due to economic and population growth.[2] Currently over 80 % of the total energy supply comes from the burning of fossil fuels, mainly oil, coal, and natural gas.[1] Even though fossil fuels are by nature non-renewable, they are estimated to support our increasing demand for energy for several centuries to come.[3] However, carbon dioxide emissions from fossil fuel combustion exceeded 32 gigatons of CO_2 in 2014.[1] Increasing CO_2 emissions have lead to a rapid growth in atmospheric CO_2 levels, exceeding 400 ppm (parts per million) for the foreseeable future in 2016.[4] A doubling of the preindustrial CO_2 level of 278 ppm has been estimated to carry a high risk of global warming of more than 2 °C, the results of which will likely have severe adverse effects on both ecosystems and human society. The CO_2 level has grown by approximately 2 ppm yearly in the 21st century, indicating that a doubling of the preindustrial CO_2 level will occur sometime in the next 20 – 30 years unless drastic action is undertaken to reduce our dependency on fossil fuels.[5] Currently there exist three viable options that supply sufficient amounts of energy by themselves in a carbon neutral way:[2]

- Continued use of fossil fuels in conjunction with carbon sequestration
- Nuclear power
- Solar energy

Each of the above-listed options suffer from specific setbacks. Carbon sequestration is energy intensive, and even minuscule leaks in carbon reservoirs will nullify the end result with time. Nuclear waste remains radioactive for hundreds of thousands of year, and the uranium resources are finite. Solar energy also suffers from setbacks, the main one being that it is diurnal and diffuse when it reaches the Earth.[2]

However, solar energy is by far the most prominent option. Practically exploitable renewable resources are very limited: 0.5 TW for hydroelectric, less than 2 TW in all tides and waves in oceans, 12 TW for the total geothermal energy at the surface of the Earth, and 2 – 4 TW of technical potential for wind power. On the other hand, 120 000 TW of solar radiation reaches the surface of the Earth. Covering only 0.16 % of the surface of Earth with 10 % efficient solar cells would suffice to fulfill the whole yearly energy demand.[2,3] However, this area is larger than those of Germany and Finland combined. Sustainable energy production requires a simultaneous contribution from multiple renewable sources.

The storing and transporting of solar energy remains a major challenge for large scale utilization. One attractive solution to this problem is storing the energy of sunlight into

chemical bonds, i.e. solar fuels. Viable solar fuels include the direct photoelectrochemical conversions of CO_2 to methanol or methane and water to hydrogen. However, the half-reactions for the conversion of CO_2 into methanol or methane involve complex six- and eight-electron transfer steps, respectively, while the reduction of water into hydrogen requires a two-electron pathway. Water is also very abundant, with just 0.01 % of the annual global rain fall containing enough hydrogen to store the annual energy need.[6] Another benefit of hydrogen is that it can be used directly to produce electricity in a fuel cell, with the only emission being water.

Fujishima and Honda [7, 8] were the first to report on a complete water photoelectrolysis system. The system was based on an *n*-type titanium dioxide (TiO_2) metal oxide photoanode that was connected to a platinum counter electrode through an external voltage supply and immersed into a NaOH electrolyte. When the TiO_2 anode was illuminated a current was generated between the two electrodes. The photogenerated electrons drove the hydrogen evolution reaction (HER) at the counter electrode, whereas holes left in the TiO_2 valence band drove the oxygen evolution reaction (OER) at the anode. The overall reaction is the cleavage of water, or photoelectrochemical water splitting. The HER is a two-electron reaction, whereas the OER requires four electrons to produce one molecule of oxygen. The OER can further be seen as the primary stage in photosynthesis,[7] and a large amount of research into various metal oxide photoanodes used for water photoelectrolysis has been published after the seminal work done by Fujishima and Honda.

TiO_2 suffers from one major setback regarding it's potential use for large scale water splitting. It's band gap is approximately 3.2 eV (anatase crystal form), meaning that it only absorbs ultraviolet radiation. This results in a maximum photoconversion efficiency of only 1.3 %.[9] An optimal material for water splitting should have a band gap of approximately 2 eV, absorbing light with a wavelength below 600 nm. Hematite (α-Fe_2O_3) has a near optimal band gap of 2.2 eV, leading to a theoretical maximum efficiency of 12.9 %.[9] Other benefits of hematite include natural abundance, high chemical stability, and low production costs.[10,11] However, the conduction band level of hematite is too low to drive the HER alone, it requires a high overpotential to drive the OER, the electron mobility is low, and the hole diffusion length is short.[12–15] Numerous different strategies have been adopted to improve these intrinsic shortcomings of hematite. These include tuning the electrode morphology,[16–23] activating the surface with the use of catalysts,[24–30] doping with various metal cations,[31–38] passivating interfaces with inactive metal oxide layers or high temperature annealing,[39–45] and forming heterojunctions with other metal oxides.[19,46–50]

1.1 Aim and scope of this work

Transient absorption spectroscopy studies of charge recombination and transfer dynamics in doped, heterostructured, and interfacially modified hematite photoanodes form the core of this Thesis. The main aim of this research was to study the primary processes that drive charge carrier generation, recombination, trapping, and transfer. These processes are of paramount importance in order to optimize metal oxide photoanode materials used for solar water splitting, since charge transfer is the basis of all photoelectrochemical reactions.

The modification of hematite photoanodes resulted in increased photoelectrochemical performance. However, the source of this increased performance is difficult to identify.

Especially the interfacial hole transfer into a surface adsorbed water oxidation precursor gives direct information on the water splitting capabilities of a photoanode. Transient absorption spectroscopy was used in this Thesis to monitor photogenerated charge carriers spanning their whole lifetime, from generation in the subpicosecond timescale to the transfer of long-lived holes in the hundreds of milliseconds timescale. The research question in this Thesis was studying dynamic charge carrier processes in hematite photoanodes in order to elucidate how they affect the photoelectrochemical performance.

The purpose of these studies was to shine light on the ways in which the charge carrier dynamics, and by extension the photoelectrochemical performance, are changed as a result of modifying the photoanode with interfacial layers. These studies constitute the first transient absorption studies of charge carrier dynamics in mixed or multilayered titania–hematite based photoanodes under water oxidation conditions to the best of the author's knowledge.

1.2 Outline

This Thesis presents the basis of photoelectrochemical water oxidation, transient absorption methods that were used to study charge carrier dynamics, and the results of four original articles published in peer-reviewed journals in the fields of physical chemistry and materials science. The thesis is divided into 5 chapters.

Chapter 2 is an introduction into the field of photoelectrochemical hydrogen production. The focus is on the properties and utilization of n-type metal oxide water splitting photoanodes. The properties of hematite and titanium dioxide are summarized. The chapter covers the requirements needed for efficient performance, with an emphasis on interfacial phenomena and charge transfer.

Chapter 3 introduces the reader to time-resolved transient absorption methods. The measurement systems are described in depth, along with the constraints inherent to each system. The chapter also presents how kinetic analysis is performed for transient absorption measurements.

Chapter 4 is the results section of the Thesis. The transient absorption results are discussed in this chapter, along with their implications. The transient absorption results are also tied with the performance of hematite. Chapter 4.1 contains additional data not published in the four articles included into this Thesis, comprising the effects of excitation density and the transient absorption features of a reference hematite photoanode under nitrogen atmosphere.

Chapter 5 concludes the Thesis. A review of the results is presented in this chapter. The Thesis concludes with a discussion on the further research that is considered important to further advance this field.

The four original research papers that form the basis of this Thesis include photodynamic studies on the charge carrier recombination and transfer dynamics of modified hematite photoanodes using transient absorption spectroscopy. The samples in **Paper I** and **Paper II** were obtained from collaborators directly, however, the author was involved in designing the samples with regard to the specifications dictated by the measurement setups. The author was involved in the sample design and preparation in **Paper III** and **Paper IV**, in which they were initiated during the author's four month research visit to Department of Chemistry, University of Cologne. All four research papers were prepared within the framework of the EC-FP7 project SOLAROGENIX (NMP4-SL-2012-310333), coordinated by Prof. Dr. Sanjay Mathur from the University of Cologne.

Paper I The first contribution presents the effects on charge transport properties from preparing photoanodes from a mixed hematite and titanium dioxide nanoparticle dispersion. The resulting mesoporous photoanode exhibited segregation of the different metal oxide layers, leading to a formation of a surface pseudobrookite layer on top of the mesoporous hematite structure. The surface layer was seen to greatly affect the charge separation, leading to increased photocurrent performance due to an increased amount of long-lived surface holes that are required for the OER. The publication was realized in collaboration with the Laboratory of Multifunctional materials, Department of Chemistry, ETH Zürich.

Paper II The second contribution presents the effects of growing an ALD titanium dioxide overlayer on a PECVD grown hematite structure. The formation of a heterojunction was observed to promote in charge separation mainly due to enhanced electron extraction from the titanium dioxide overlayer. The overlayer was also observed to aid in the dynamics of long-lived hole transfer into water splitting intermediates. The publication was realized in collaboration with the Department of Chemistry and Department of Physics and Astronomy at Padova University, the Electron Microscopy for Materials Research group at University of Antwerp, the Department of Chemistry at University of Cologne, and the Chemistry for Technologies Laboratory at University of Brescia.

Paper III The third contribution is an indirect continuation of the second contribution. Here a PECVD grown few layer graphene sheet was incorporated between a PECVD grown hematite underlayer and titanium dioxide overlayer. The graphene middle layer was observed to aid in charge separation between the two layers, noticeably lowering the photocurrent onset potential of the photoanode. Retarded primary electron-hole recombination in the picosecond timescale was observed for the graphene intercalated photoanode. The publication was realized in collaboration with the Department of Chemistry at University of Cologne and Applied Laser Technologies research group at Ruhr Universität Bochum.

Paper IV The fourth contribution arose from an interest to study the doping induced into a hematite layer from the transparent conducting oxide (TCO) on which it is grown. Hematite is generally annealed at high temperatures to passivate recombination states. This results in a loss of conductivity in indium tin oxide substrates (ITO), so fluorine doped tin dioxide (FTO) is typically the preferred substrate. The high annealing temperatures lead to ion diffusion from the TCO, thus doping the photoanode unintentionally. The use of FTO in stead of ITO results in increased tin doping of the photoanode due to the fact that FTO is doped tin oxide, whereas ITO only contains roughly 10 % tin dioxide. The unintentional high temperature doping was taken advantage of by sputtering thin layers of ITO on top of FTO substrates, thus leading to indium doping and reduced tin doping while maintaining the conductivity of the TCO. The doping was observed to affect millisecond to second timescale charge transfer dynamics drastically, leading to increased PEC performance due to a noticeably increased long-lived hole population. On the other hand, the subnanosecond charge carrier dynamics were observed to remain unchanged between the hematite layers deposited on different substrates. The publication was realized in collaboration with the Department of Chemistry at University of Cologne.

2 Photoelectrochemical water splitting

This chapter introduces the reader to the field of photoelectrochemical water splitting using n-type metal oxide semiconductors. The chapter focuses on the properties of n-type metal oxide semiconductors and the formation of the semiconductor-electrolyte interface (SEI). The properties of the SEI are important to understand the primary processes in water splitting, namely interfacial charge transfer and recombination.

2.1 Cell reactions and energetics

The water splitting half reactions are typically written as they occur in acidic conditions (pH=0) along with the associated half cell potentials versus the standard hydrogen electrode.[51]

$2\ H^+ + 2\ e^- \longrightarrow H_2$	$E^\circ = 0.000$ V (HER)
$2\ H_2O \longrightarrow O_2 + 4\ H^+ + 4\ e^-$	$E^\circ = -1.229$ V (OER)
$2\ H_2O \longrightarrow 2\ H_2 + O_2$	$E^\circ_{\text{cell}} = -1.229$ V (overall)

In an alkaline electrolyte (pH=14) the half reactions can be written as follows by taking the dissociation reaction of water to protons and hydroxyl ions into account.[51]

$2\ H_2O + 2\ e^- \longrightarrow H_2 + 2\ OH^-$	$E^\circ = -0.828$ V (HER)
$4\ OH^- \longrightarrow O_2 + 2\ H_2O + 4\ e^-$	$E^\circ = -0.401$ V (OER)
$2\ H_2O \longrightarrow 2\ H_2 + O_2$	$E^\circ_{\text{cell}} = -1.229$ V (overall)

The Gibbs free energy change for the overall reaction is given by the equation

$$\Delta G^\circ = -nFE^\circ_{\text{cell}}, \tag{2.1}$$

where ΔG° is the Gibbs free energy change, n is the number of moles of electrons transferred in the reaction, F is the Faraday constant (charge per mole of electrons), and E°_{cell} is the reaction cell potential. Under standard conditions the Gibbs free energy change for the conversion of H_2O to H_2 and 1/2 O_2 is $\Delta G^\circ = +237$ kJ/mol. The positive Gibbs free energy change shows that the reaction is thermodynamically uphill, unlike in photocatalysis reactions where the reactions are spontaneous (negative ΔG°).[6]

For sunlight to be able to drive the water splitting reaction, the energy of a photoexcited electron needs to surpass the reaction's thermodynamic potential. The photon energy thus needs to be at least 1.23 eV. This energy can be converted to the wavelength of incident light by using equation 2.2

$$\lambda = \frac{hc}{E} \approx \frac{1240 \text{ nm/eV}}{E}, \tag{2.2}$$

where λ is the wavelength of the incident photon, h is the Planck constant, c is the speed of light, and E is the required energy in eV.

According to equation 2.2 the photon wavelength needs to be under 1000 nm for it to have sufficient energy to enable the water splitting reaction. This covers the whole ultraviolet – visible range all the way into the near infrared region, containing 78 % of the total solar irradiance of 1000 W/m^2 (or 100 mW/cm^2). The solar spectrum at the top of atmosphere and surface of the Earth are shown in Figure 2.1 to illustrate the relative amount of energy contained in the irradiation band below 1000 nm.

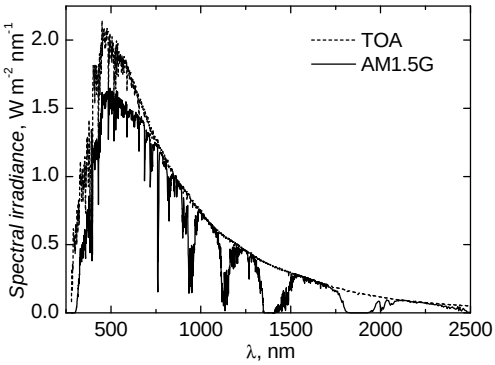

Figure 2.1: Solar irradiance at the top of atmosphere (TOA) and for air mass 1.5 global (AM1.5G) according to ASTM G173-03.[52]

However, the above calculation does not give an accurate description of the efficiency obtainable with PEC water splitting. First, assuming that one photon can only excite one electron, a majority of the energy contained in a short wavelength high energy photon is lost thermally. The AM1.5G solar photon flux is shown in Figure 2.2, illustrating the number of photons at each wavelength arriving to the surface of the Earth. Second, the Gibbs free energy change of the water splitting reaction does not take into account the overpotential needed to overcome the entropic loss associated with the generation of conduction band electrons and the kinetic losses due to the overpotentials for the OER and HER. Together these losses amount to approximately 0.8 eV,[9] meaning that the photon energy should exceed 2.03 eV, or have a wavelength smaller than 620 nm according to equation 2.2.[9,23] This leads to a maximum photoconversion efficiency of 16.8 % for water splitting using a single photoanode made of a hypothetical ideal material with a band gap of 2.03 eV.[9]

The overall solar-to-hydrogen (STH) efficiency for a single photoanode can be calculated with[6]

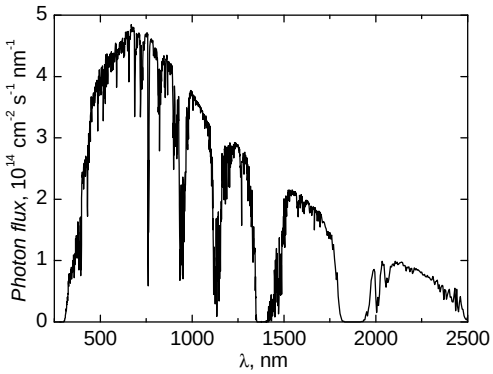

Figure 2.2: Solar photon flux in the AM1.5G spectrum.[52]

$$\eta_{\mathrm{STH}} = \frac{J_{\mathrm{ph}}(V_{\mathrm{redox}} - V_{\mathrm{bias}})}{P_{\mathrm{light}}}, \tag{2.3}$$

where J_{ph} is the photocurrent density per illuminated area, V_{redox} is usually the voltage calculated from either the more commonly used Gibbs free energy change (1.23 V) or the enthalpy change (1.48 V) of the overall cell reaction, V_{bias} is the potential difference between the working and counter electrodes (not the bias applied in a three-electrode cell), and P_{light} is the illumination power density (100 mW/cm^2 for AM1.5G).

The STH efficiency can be more directly determined by measuring the rate of hydrogen generation ($\Phi_{\mathrm{H_2}}$) and multiplying it with the Gibbs free energy of hydrogen formation ($G^{\circ}_{f,\mathrm{H_2}} = 237$ kJ/mol)

$$\eta_{\mathrm{STH}} = \frac{\Phi_{\mathrm{H_2}} G^{\circ}_{f,\mathrm{H_2}}}{P_{\mathrm{light}}} \tag{2.4}$$

However, for this calculation the water splitting reaction needs to be stoichiometric, no sacrificial agent should be used, and no external bias should be applied. In an optimal case these two methods give the same result for STH efficiency.

The incident photon-to-current efficiency (IPCE) gives the external quantum efficiency of a photoanode as a function of illumination wavelength

$$\mathrm{IPCE}(\lambda) = \frac{hc}{q}\frac{J_{\mathrm{ph}}(\lambda)}{\lambda P(\lambda)}, \tag{2.5}$$

where $J_{\mathrm{ph}}(\lambda)$ and $P(\lambda)$ are the photocurrent and illumination power at wavelength λ, respectively, and q is the elementary charge. IPCE can also be used to calculate the internal quantum efficiency, or absorbed photon-to-current efficiency (APCE)

$$\mathrm{APCE}(\lambda) = \frac{\mathrm{IPCE}}{1 - R - T}, \tag{2.6}$$

where R and T are the reflectance and transmittance of the sample, respectively. The absorbance A, or optical density, of a sample can be calculated from transmittance and reflectance with $A = -\log\left[T/(1-R)\right]$.

Absorbance is further related to the absorption coefficient α and sample thickness d with $\alpha = \ln(10)\ A/d$. Light penetration depth is defined as the inverse of the absorption coefficient, α^{-1}. It is the distance in which the intensity of the illumination light has dropped to $1/e$ (37 %) of the original value. The absorption coefficient can be used to determine the optical band gap of a semiconducting material with Tauc plots. Tauc plots are obtained by extrapolation from a $(\alpha h\nu)^m$ vs. $h\nu$ plot, where the $h\nu$ intercept gives the band gap of the material. The constant $m = 1/2$ for an indirect band gap and $m = 2$ for a direct band gap transition.[6]

2.2 Metal oxide semiconductors

Materials can be divided into three groups according to their electronic properties; insulators, semiconductors, and metals. In crystalline solids with a periodic structure the linear combinations of atomic orbitals leads to the formation of a band structure, where the individual atomic orbitals form continuous bands of energies available for electrons. The bands are split into two, the filled valence band and the unfilled conduction band, with the energy difference between the bands known as the band gap. In metals the conduction band is either partially filled or the two bands overlap, leading to high electrical conductivity due to electrons travelling in the conduction band. On the other hand, in insulators the valence band is completely filled and the conduction band remains empty. Semiconductors have a band structure similar to those found in insulators, however, the band gap in these materials is small enough to allow the thermal excitation of electrons from the valence band to the conduction band. Thus semiconductors typically have conductivities between those found in metals and insulators.[53]

Intrinsic semiconductors have the same amount of holes in the valence band as they have electrons in the conduction band. Semiconductors that have a more electrons in the conduction band than they have holes in the valence band are called n-type, and the majority charge carriers in these materials are the conduction band electrons. If the situation is reversed the majority carriers are holes and the semiconductor is called p-type. The semiconductor type can be changed with doping, where either donor or acceptor atoms are infused in the crystal lattice. The donor atoms donate a conduction band electron, whereas the acceptors remove one electron from the valence band, increasing the number of valence band holes. Thus by increasing the number of donors or acceptors in an intrinsic semiconductor it can be made into an n-type or a p-type semiconductor, respectfully.[53] Increasing the number of donors in an n-type semiconductor leads to an increase in the number of majority carriers, increasing the conductivity of the material. However, the concentration of dopants is typically limited to 1 – 2 %, with higher concentrations leading to a segregation of the dopant phase.[6]

A valence band electron can be optically excited to the conduction band by the absorption of a photon with energy larger than the band gap. If the valence band maximum and conduction band minimum of the semiconductor occur for the same wave vector ($\overline{\mathbf{k}}$) value the electron transition is called direct.[53] However, if the valence band maximum and conduction band minimum are displaced from each other the transition requires a change in the crystal momentum and is called indirect. Since photons carry negligible momentum the transition requires the absorption of a phonon (lattice vibration) along with the absorption of the photon. This makes the transitions less likely to occur, lowering the absorption coefficient of indirect semiconductors near the band gap energy.[6,54]

In conventional semiconductors, such as silicon or germanium, the atoms bond together

covalently. The bonds are composed of the outer 3s and 3p orbitals that form sp^3 hybridized orbitals. The bonding is different in metal oxide semiconductors due to the high electronegativity of oxygen. Since metals are much less electronegative than oxygen, the valence electrons are at least partially transferred to the oxygen atoms. Therefore the bonds have a highly polar character in metal oxide semiconductors. In hematite and titanium dioxide the valence band is occupied by electrons in oxygen 2p orbitals that have been transferred from the iron or titanium atoms when the bond was formed. On the other hand, the conduction band has mainly iron or titanium 3d character.[6,10] However, the initial orbital assignment of the band structure suggested that the band gap in hematite is due to an indirect Fe^{3+} d−d transition, whereas a higher energy direct transition occurred from oxygen 2p to iron 3d, leading to two different types of holes in hematite. More recent electronic structure calculations, supported by X-ray absorption and emission spectroscopy, indicate that the valence band in hematite is mostly oxygen 2p in character.[10,55–58] Metal oxide semiconductors typically have lower charge carrier mobilities and conductivity than conventional semiconductors, with pure hematite exhibiting the characteristics of either a charge transfer or a Mott-Hubbard type insulator.[10]

Charge carriers in many transition metal oxide semiconductors are not free in the same sense as they are in conventional semiconductors. Because the charge carriers in metal oxide semiconductors move relatively slowly through the lattice they displace the surrounding atoms. The potential well due to the lattice displacement may lead to the charges becoming self-trapped, only moving forward when the surrounding atoms suitably alter their position. This is called a polaron. Two types of polarons exist; large polarons occur when the lattice distortion spreads over many structural units and small polarons occur when the distortion collapses into a singe unit. Polaron formation is spontaneous when the energy gained by the lattice due to charge trapping exceeds the displacement strain of the nearby ions, thus minimizing the free energy. The charge transport in transition metal oxides occurs mainly by small-polaron hopping, in which the highly localized charge carrier moves to the next suitable position along with the lattice distortion. A hop can only occur if the initial and final sites have equal electronic energies. The small-polaron hopping typical to metal oxides has an Arrhenius type temperature dependence. This means that the drift mobility in metal oxide semiconductors is temperature dependent, increasing with higher temperatures.[59]

2.3 Semiconductor-electrolyte interface

Water molecules dissociatively adsorb on a metal oxide semiconductor surface when it is brought into contact with an aqueous electrolyte (and even in humid air).[6] This results in the surface being terminated with hydroxyl groups, breaking the bulk symmetry of the lattice and forming electronic surface states within the band gap of the semiconductor. Since the energy levels of these surface states are below the conduction band minimum, free electrons from the conduction band occupy them. The ionized donors from which the free carriers originated remain in the bulk, forming a positive space charge and inducing an electric field in the topmost layer of the semiconductor bulk. This field induces a potential drop across the space charge region due to the inbuilt electric field, also known as band bending. The free electrons will continue transferring to the surface states until the potential barrier due to the electric field grows too large for electrons to cross. After this no net electron transport takes place, and a dynamic equilibrium is established.[6] An external anodic bias voltage can be employed to lower the Fermi level of the semiconductor,

further increasing the electric field strength and widening the space charge region. When the semiconductor is in equilibrium the Fermi levels for both holes and electrons will remain at the level where the probability of finding an electron is $\frac{1}{2}$. However, when the equilibrium is disturbed, for example with illumination, the Fermi levels will split into quasi Fermi levels. In an n-type semiconductor the quasi Fermi level for electrons will remain at approximately the same level as in the equilibrium situation since changes in charge carrier concentration do not affect the distribution of majority carriers much. However, the quasi Fermi level for holes will drop to a noticeably lower level than in the equilibrium situation.[60] The quasi Fermi levels for holes and electrons can be interpreted as the thermodynamic driving force behind the reactions in which they take part.[6]

The counter charges to the surface trapped electrons are provided by the ionized donors in the bulk of the semiconductor and an accumulation of oppositely charged ions in the solution. The ions are surrounded by a solvation cloud of polar water molecules, that forces the ions to remain 2–5 Å away from the semiconductor surface. The region between the surface and the closest solvated ions is called the Helmholtz layer. When an external bias voltage is applied to the semiconductor with respect to a reference electrode, the potential difference is distributed over the space charge and Helmholtz layers. Since the capacitance of the Helmholtz layer is much larger than the capacitance of the space charge layer, changes to the applied voltage will fall across the space charge layer. This means that applying an anodic external bias voltage (reverse bias) will result in an increase of the space charge layer width in n-type semiconductors. This is different for the case of a metal counter electrode, where any overpotential applied must fall across the Helmholtz layer.[6]

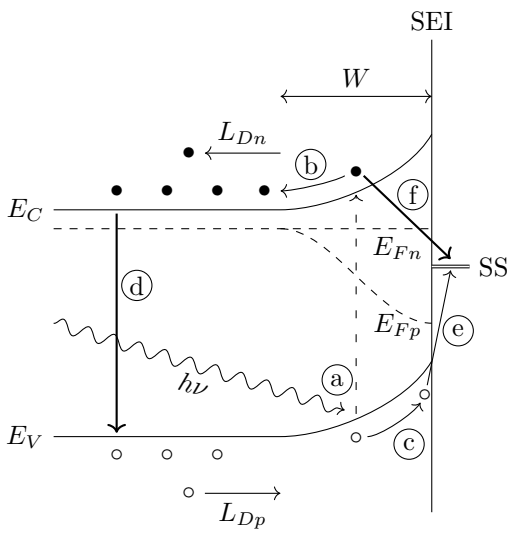

Figure 2.3: Charge carrier behaviour after excitation.

The processes occurring in an illuminated metal oxide semiconductor in contact with an electrolyte are illustrated in Figure 2.3. The space charge region is marked with W, illustrating the space charge region width. The absorption of a photon with energy $h\nu$ that is larger than the band gap leads to the generation of an electron-hole pair (a). Within the space charge region rapid charge carrier separation takes place, resulting in the electrons travelling towards the bulk due to electron drift (b) and holes travelling

towards the semiconductor-electrolyte interface due to hole drift (c). The electron-hole pair may also separate due to diffusion or recombine directly (d) or through a bulk trap state (not shown). The electrons must diffuse to the external circuit through the bulk. The distance and direction that the electrons must diffuse for water reduction at the counter electrode is illustrated with the electron diffusion length L_{Dn}. The introduction of excess carriers due to illumination leads to the splitting of the Fermi levels into quasi Fermi levels for electrons and holes, E_{Fn} and E_{Fp}, respectively. Holes that are generated within the hole diffusion length L_{Dp} can travel to the space charge region, where they are swept up by the inbuilt electric field. The valence band holes can react with water splitting intermediates or recombination centers on the surface (e), marked as surface states SS. The conduction band electrons can also recombine with the holes in the surface states (f).[6,61,62] There may also be recombination centers in the surface that are not associated with water splitting intermediates. If the density of these surface states is high they may cause Fermi level pinning.[6,39]

Marcus [63] developed a theory to describe the dynamics of electron transfer reactions between a donor and acceptor molecule using potential surface coordinate diagrams of the Gibbs free energy of the species involved. An important concept in this theory is that every molecule or ion is surrounded by a cloud of oriented solvent molecules forming the inner sphere. In addition, the ions have coulomb interactions with solvent molecules and ions at a longer distance, known as the outer sphere. This leads to a concept of fluctuating energy levels in the electrolyte. Gerischer [64] later used a similar approach to electron transfer reactions between a semiconductor and an electrolyte species using the electronic energy levels of the redox species involved. After reduction or oxidation of an ion, the surrounding solvent molecules will rearrange themselves due to the different charge of the ion. The energy required for this is given by the reorganization energy (λ_{re}). The probability distribution of the fluctuating energy levels depends on the standard potentials of the redox species as well as the required reorganization energy. At room temperature the widths of the reduced and oxidized species probability fluctuations are given by $\Delta E \approx 0.53\sqrt{\lambda_{\mathrm{re}}}$. The reorganization energy ranges typically from 0.3 eV to more than 1 eV. Charge transfer in the case of an illuminated n-type semiconductor in contact with a basic electrolyte takes place by hole transfer from the top of valence band to a water splitting intermediate, if charge transfer via surface states is neglected. The charge transfer itself takes place by tunneling. Tunneling is an iso-energetic process, indicating that the fluctuating energy level of the reductant species should be equal to the energy of the hole in the valence band. This means that a large overlap of the energy level distribution in the electrolyte and valence band level in the semiconductor are required for more probable charge transfer. Another conclusion is that the probability of charge transfer decreases if the valence band energy is at a much lower energy level than the energy distribution of the reductant, in this case hydroxyl species and water splitting intermediates in the oxygen evolution reaction.[6] However, it is important to note that this analysis does not take into account that water oxidation requires the transfer of four separate holes to produce one molecule of oxygen, changing the energy levels of the reductant in each step, and that charge transfer from metal oxide semiconductors often occurs through surface states.[65]

2.4 Requirements for efficient photoanodes

Efficient water splitting requires high absorption of light in the optimal spectral window between 400 – 620 nm. The higher end of the range comes from the thermodynamic

requirements specified earlier, and the lower end is due to the solar photon flux dropping rapidly below 400 nm, as can be seen in Figure 2.2. This imposes a band gap limit of 2.0 – 3.1 eV on the material. The light penetration depth should also be less than the distance in which charge carriers can be efficiency separated, indicating that the optimal film thickness is $d \approx \alpha^{-1} \approx L_D + W$. This ties a material's absorption coefficient to its electronic properties, since with a high light penetration depth a sample also requires more efficient charge transport in the semiconductor for efficient water splitting to occur. One way to affect the problem of penetration depth rarely coinciding with the depletion region width and diffusion length is nanostructuring the photoanode so that photogenerated holes have a shorter distance to reach the SEI from where they are generated. Since the electron diffusion length is much longer than the hole diffusion length in hematite, nanostructuring enables the optimization of charge collection efficiency for both majority and minority carriers. It also increases the electrode's surface area, leading to an increased number of active surface sites that leads to enhanced charge transfer dynamics. [6]

A photoanode also needs to be chemically stable in basic conditions under illumination and external voltage. This limits the usefulness of many photoactive materials, since under these conditions most non-oxide semiconductors either dissolve or form a thin oxide layer that prevents charge transfer. [6] Oxide semiconductors are typically more stable, but may be prone to anodic decomposition due to surface holes, as is the case with zinc oxide. [66] The hole transfer across the SEI should be sufficiently fast for it to outcompete the anodic decomposition reaction. The reaction should also be fast enough to minimize the accumulation of surface charges, since this decreases the built-in electric field and increases electron-hole recombination as a direct result. Catalytically active surface species can be added to metal oxide photoanodes, such as RuO_2 or IrO_x, however, catalytically active surface sites can also act as efficient recombination centers. The catalysts may also increase the back reaction between hydrogen and oxygen if they are not well separated in the photoelectrochemical cell. [6]

Stability against photocorrosion typically increases with increasing bad gap, which means that good absorption properties are a trade-off with photoanode stability. In addition to the band gap affecting the absorption and stability of a semiconductor, the conduction and valence band edges should straddle the HER and OER potentials. No semiconducting material exist that straddle both potentials while remaining stable under operating conditions with a small enough band gap for visible light absorption. Most metal oxide semiconductors favour water oxidation due to their low valence band level. The band gaps and band edge positions of hematite, anatase titanium dioxide and tin dioxide are shown in Figure 2.4. The conduction band level of hematite is approximately 0.3 eV lower than the HER potential. This means that an external bias voltage is required to supply the conduction band electrons energy to take part in the HER. Raising the electron energy by 0.3 eV is not enough due to the overpotentials required for the OER and HER. [6]

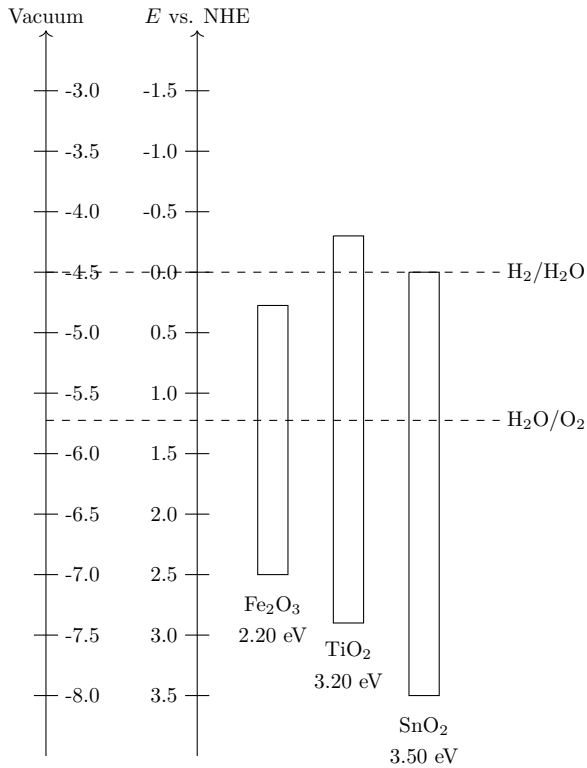

Figure 2.4: Energy band levels for Fe_2O_3, TiO_2, and SnO_2.[67]

3 Transient absorption spectroscopy

This chapter introduces the transient absorption equipment and kinetic analysis methods used in all of the publications in this Thesis. The chapter focuses on device specifications and requirements needed for efficient determination of charge carrier behaviour in n-type hematite photoanodes. An in-depth explanation of the methods used for kinetic analysis of the recorded transient data is also given.

The fundamental idea behind transient absorption spectroscopy is to use short pulses of light to excite the material under study. The excitation results in either increased or decreased absorption due to changes in the system states. The absorption dynamics can be studied to determine the pathways of charge transfer processes and reaction rates. Typically the excitation pulse width determines the fastest possible time response of a given system, although the monitoring light intensity and detector choice do play a major role in the time and absorption resolutions. The systems used for transient absorption measurements in this Thesis are nanosecond flash-photolysis and femtosecond pump-probe spectroscopies.

3.1 Nanosecond flash-photolysis spectroscopy

The flash-photolysis method was developed by George Wreyford Norrish and George Porter in the 1950's.[68,69] Their system used short pulses from a flash lamp to excite gas molecules, triggering a chain of reactions that could be followed spectroscopically. They were awarded the Nobel prize in chemistry in 1967 "for their studies of extremely fast chemical reactions, effected by disturbing the equilibrium by means of very short pulses of energy" along with Manfred Eigen.[70] Flash-photolysis measurements were performed for **Paper I**, **Paper II**, and **Paper IV**.

The key to the flash-photolysis method is the use of short pulses of excitation light, known as pump pulses, to disturb the equilibrium ground state of a molecule or material. The absorption of a photon raises one electron to a higher energetic state. The excited molecule can relax back to the ground state directly or through intermediate states, or take part in a photoreaction such as charge transfer. The transient excited and intermediate states have their own absorption spectra, which can be monitored via the change in the intensity of monitoring light, or probe beam, passing the excited material. The probe beam can be either pulsed or continuous.

A simplified optical scheme of the flash-photolysis system is presented in Figure 3.1, along with a scheme of the PEC cell. Continuous probe monitoring light from a halogen lamp is collimated with a plano-convex lens L1 into the photoelectrochemical (PEC) cell. The sample is excited with a pulsed nanosecond laser with quasi-parallel orientation of the pump and probe beams. The laser beam width is adjusted with lenses to cover the

whole monitored area of the sample inside a PEC cell. The excitation pump beam comes from the SEI side through the electrolyte to enable efficient charge separation at the interface. The probe beam is collected into a detection monochromator that is coupled with a photodetector. The signal from the photodetector is recorded with an oscilloscope, showing the transient decay at the selected detection wavelength.

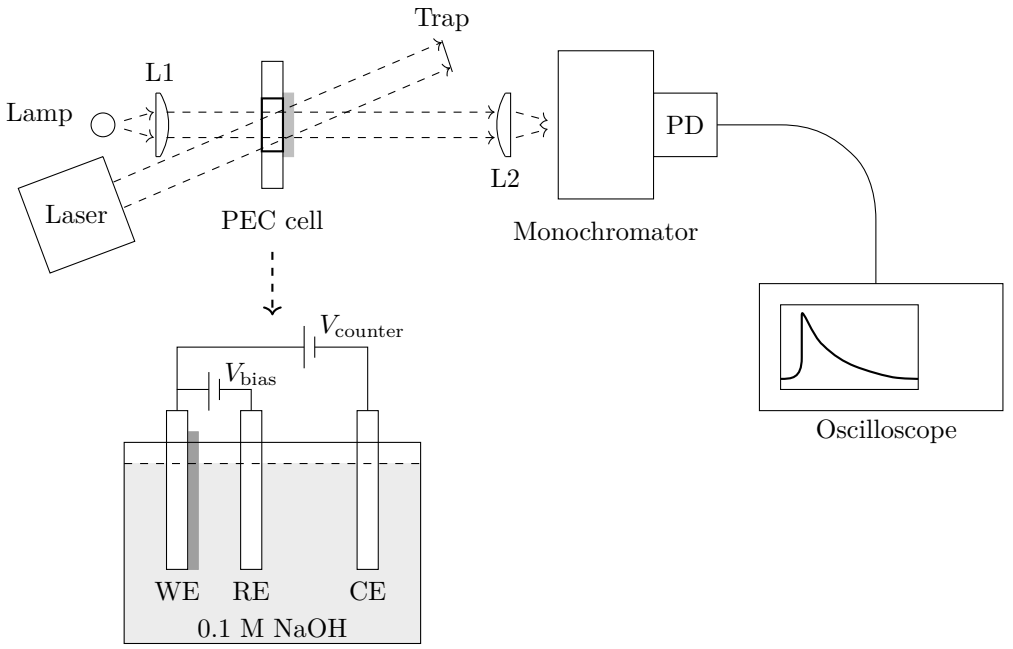

Figure 3.1: Optical scheme of the flash-photolysis method. For measurements with bias voltage a three electrode PEC cell was filled with 0.1 M NaOH electrolyte, with the sample connected as working electrode (WE) with a Ag/AgCl reference electrode (RE) and a platinum wire counter electrode (CE). V_{bias} is the applied bias voltage between the working and reference electrodes and V_{counter} is the voltage applied to the counter electrode to ensure that the counter electrode passes the same current as the working electrode.

The absorption change with respect to time and wavelength, or transient absorption decay, can be calculated using

$$\Delta A(t,\lambda) = -\log_{10}\left(1 + \frac{\Delta I(t,\lambda)}{I_0(t,\lambda)}\right), \tag{3.1}$$

where $\Delta I(t,\lambda)$ is the change in monitoring light intensity after excitation and $I_0(t,\lambda)$ is the intensity before excitation. Since the photodetector signal is linearly proportional to the light intensity, the absorption change can be calculated from the voltage data recorded by the oscilloscope using

$$\Delta A(t,\lambda) = -\log_{10}\left(1 + \frac{\Delta V(t,\lambda)}{V_0(t,\lambda)}\right), \tag{3.2}$$

where $\Delta V(t,\lambda)$ is the change in recorded voltage after excitation and $V_0(t,\lambda)$ is the voltage recorded before excitation. The oscilloscope is pre-triggered with a fast photodiode that

sends a voltage signal to the oscilloscope when the excitation laser flash is generated. $V_0(t, \lambda)$ is then calculated from the average voltage recorded before the excitation beam arrives at the sample.[71] A transient absorption spectrum can be obtained by scanning the detection monochromator and repeating the measurement for the desired probe wavelengths.

The third harmonic of a neodymium-doped yttrium aluminium garnet (Nd:YAG) laser operating in Q-switched mode was used as the excitation pump. The excitation wavelength in each above-mentioned paper is 355 nm, generated by sum frequency generation of the primary 1064 nm and second harmonic 532 nm pulses. The third harmonic FWHM (full width at half maximum) was approximately 10 ns. The laser was pumped with a flash lamp discharged with a 10 Hz repetition rate. The Q-switch was operated so that the actual excitation repetition rate was 0.33 – 0.17 Hz, exciting the sample once every 3 – 6 seconds. The low repetition rate was necessary to allow the sample to return to the steady state condition before the next excitation pulse. The excitation densities used ranged from 200 to 1000 μJ/cm^2.

The components in the flash-photolysis system used in this Thesis are given in Table 3.1.

Table 3.1: Flash-photolysis system components

Pump laser	Solar TII LF 117 with F015 third harmonic generator
Probe source	Thorlabs SLS201/M 9 W stabilized halogen lamp
Monochromator	Digikröm CM110
Photodetector	New Focus 2107-FS-M 10 MHz balanced Si photoreceiver
Oscilloscope	Tektronix TDS3032B or TDS 5032B
System control	Luzchem mLFP-111 or in-lab program

A stabilized halogen lamp was used as the monitoring probe. Typically high power xenon lamps are used to provide the monitoring light, since higher probe power increases the signal to noise ratio. However, the output of a xenon lamp often has relatively large vibrations in intensity coming from plasma fluctuations due to power supply instability that are absent from halogen lamps due to the light originating from a heated metal coil. The xenon fluctuations disturb mainly long-lived signals (> 1 ms) with very low signal intensities ($\Delta A < 10^{-3}$ mOD). Since the long-lived transient absorption in metal oxide semiconductors is often very low in intensity, the halogen lamp provided increased monitoring light stability in the millisecond to second time scale.

However, since the time resolution of a flash-photolysis measurement is inversely proportional to the monitoring light intensity,[71] the use of a low power halogen lamp inherently limits the time resolution to some extent. The other factors that limit the time resolution of a flash-photolysis measurement are the laser FWHM and the photodetector response time. Nanosecond time resolution with Nd:YAG lasers and photomultiplier tube detectors are achievable if the monochromatic monitoring light intensity is much higher than that obtainable from the halogen source. The excitation laser has a FWHM of 10 ns, whereas the photodetector rise time is 80 ns. This results in a maximum time resolution of approximately 80 ns, when used with a high intensity monitoring light source. However, the time resolution of the photodetector was further reduced by the need to increase the signal gain in the balanced photoreceiver to achieve higher recorded voltages due to the low intensity of the halogen lamp. At maximum gain amplification of 3×10^4 the 10 MHz

bandwidth of the photodiode is reduced to 250 kHz, corresponding to a signal rise time of 4 μs.

The system used for the measurements in this Thesis was built to optimize the detection of long-lived low amplitude signals, limiting the time resolution obtainable in the same measurement. Indeed, since the transient absorption signal was often below 10^{-4} mOD, even electrical noise from the photodiode amplifier needed to be accounted for to achieve a reasonable signal to noise ratio. To obtain the highest reasonable signal to noise ratio for millisecond – second timescale measurements the electrical noise was reduced with a 40 μs RC-filter in front of the oscilloscope input. The practical time resolution in the flash-photolysis measurements presented in this Thesis is 40 μs.

The measurements were repeated 30 – 300 times for each wavelength, depending on if the measurement was controlled by the Luzchem mLFP-111 or the in-lab system. Since repeating the measurements N times improves the signal to noise ratio by $\sqrt{N}$,[71] increasing the amount of averaging tenfold improves the signal to noise ratio by a factor of $\sqrt{10} \approx 3.2$. However, the Luzchem mLFP-111 measurement program suffered from 16-bit integer overflow, resulting in an inversion of the transient absorption data if a value of 32 767 was surpassed for the product of monitoring light read out voltage and number of averages. This severely limited the signal to noise ratio of the Luzchem system.

The mLFP-111 program also worked only with the Tektronix TDS 3032B oscilloscope, limiting the number of data points per measurement to 10 000. This means that a measurement with 40 μs time resolution could only be 400 ms long in total. Thus separate measurements had to be made to distinguish between submillisecond and second timescale processes. An in-lab control program was coded to surpass the problems of data inversion and to enable using a Tektronix TDS 5032B oscilloscope that can handle 4 000 000 data point measurements. The in-lab program could thus be used for an unlimited number of averaging of 2 second long data sets with just 50 000 data points using 40 μs time resolution. Unfortunately, the in-lab program was finalized after each paper included in this Thesis was published. However, data measured with the new in-lab program will be included into the results of this Thesis in Chapter 4.

3.2 Femtosecond pump-probe spectroscopy

Flash-photolysis is limited to the hundreds of picoseconds response time due to the continuous monitoring light used for the system. The pump-probe method was developed to overcome these limitations with the use of a short monitoring pulse in addition to the short excitation pulse. One of the first groups to study chemical reaction dynamics in the tens of femtoseconds time range was led by Ahmed Zewail,[72,73] who received the Nobel price in chemistry in 1999 "for his studies of the transition states of chemical reactions using femtosecond spectroscopy".[74] Femtosecond pump-probe measurements were performed for all publications included to this Thesis.

A simplified optical scheme of the pump-probe system is presented in Figure 3.2. Ultrashort laser pulses from a titanium doped sapphire (Ti:Al_2O_3 or Ti:sapphire) laser are split into two beams with uneven energy. Approximately 90 % of the primary pulse energy is directed into an optical parametric amplifier (OPA) for the generation of excitation pulses of desired wavelength. The excitation pulse is then focused at the sample inside a PEC cell. The remaining 10 % of the primary pulse energy is directed to a motorized translational stage, or delay line. After crossing the delay line the pulses are directed to a 2 mm thick sapphire crystal (S) or water cuvette for the generation of short white continuum probe

pulses. The spectrum of the white continuum depends on the transparent medium in which it is generated. The white continuum generated from a water cuvette is higher in intensity in the visible range close to UV but the intensity in the near IR is lower than from the sapphire crystal. The probe is then split into two pulses of roughly equal energy before they are directed to the sample. The signal probe pulse crosses the sample at the exact same position at the SEI where the excitation pump hits, whereas the reference probe pulse crosses the sample away from the excitation spot. Both probe pulses are collected at a spectrograph with a Si photodiode array for the calculation of absorbance change.

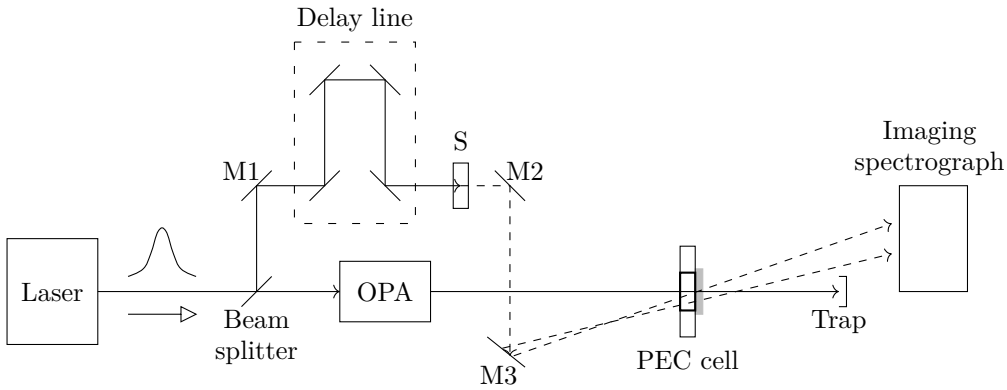

Figure 3.2: Optical scheme of the pump-probe method.

The spectra of both the signal and reference probe pulses are used to calculate the change in absorbance between them. The ratio of the two spectra is calculated as $R(\lambda) = I_S(\lambda)/I_R(\lambda)$. However, this ratio contains unwanted noise since the spectra are not identical in intensity due to imperfections in the optical components. This is solved by measuring two consecutive sets of probe pulses, first a baseline without the excitation pulse and second with the excitation pulse allowed to hit the sample. This is implemented with an optical chopper that is synchronized with the laser pulses, blocking every second pump pulse. The spectral ratios are then used as baseline R_0 and excitation R for the calculation of absorbance change[71]

$$\Delta A(\lambda) = -\log_{10}\left(\frac{R}{R_0}\right), \tag{3.3}$$

The delay line is used to retrieve transient absorption data with regard to time. The system is calibrated so that at time zero the pump and probe pulses arrive at the sample surface simultaneously. The measurement is started so that the probe pulses arrive at the sample a few hundred femtoseconds before the pump pulse. Since the sample is not in an excited state, there is no change in absorbance. After this the delay line is consecutively lengthened so that the probe pulses arrive at the sample later in time. At time zero the pump and probe pulses coincide, and scanning the delay line further returns absorbance change with respect to the difference in time between the excitation pump and monitoring probe pulses. The maximum optical path length of the delay line is approximately two meters, corresponding to a maximum delay of 6.6 ns between the pump and probe pulses.

The laser system providing the base pulses for the optical scheme shown in Figure 3.2 is a sub-100 femtosecond Ti:sapphire laser. A mode-locked Ti:sapphire seed laser is pumped

with a diode-pumped frequency doubled Nd:YVO_4 (neodymium-doped yttrium vanadate) laser in continuous wave mode. The seed laser generates sub-100 femtosecond pulses at 800 nm with a repetition rate of 80 MHz. The pulses from the seed laser need to be amplified for the generation of high power ultrashort pulses. This is performed by first pumping an amplifier Ti:sapphire crystal with a diode-pumped frequency doubled Nd:YLF (neodymium-doped yttrium lithium fluoride) high power amplifier laser operating at 1 kHz repetition rate. The seed pulses are passed through the excited amplifier Ti:sapphire crystal. Since the peak power of the ultrashort pulses is in the gigawatt range, the pulses need to be amplified using a beam extender-amplifier-compressor scheme. This limits the peak power of the pulses so that they do not self-focus destructively when passing through the optical components. The final laser output is 1 mJ sub-100 femtosecond pulses at 800 nm with a repetition rate of 1 kHz.

The components in the pump-probe system used in this Thesis are given in Table 3.2

Table 3.2: Pump-probe system components

Pump laser	Coherent Inc. Libra F with Vitesse seed and Evolution 15/30 amplifier lasers
Laser output	sub-100 ps pulses at 800 nm, 1 kHz repetition rate, 1 mJ energy
OPA	Light Conversion TOPAS-C with output range 240 – 2600 nm
Probe source	White continuum from 2 mm thick sapphire crystal or water cuvette
Measurement system	CDP Systems Excipro
Detector	Si photodiode array

The transient absorption spectra were recorded by averaging 2 500 – 10 000 consecutive spectra at each delay time. Furthermore, the whole measurement scan was repeated 1 – 5 times to compensate for possible excitation intensity fluctuations.

3.3 Kinetic analysis

Transient absorption measures the change in the absorbance of the sample with respect to time and the ground state absorbance.[71] Intermediate states are formed after photoexcitation due to photochemical reactions, such as charge transfer or trapping. The change in the population of a state n_i with time can be written for a chain of first order reactions as

$$\frac{dn_i}{dt} = -\left(\sum_{j=1}^{n} k_{ji}\right) n_i + \sum_{j=1}^{n} k_{ij} n_j, \tag{3.4}$$

where k_{ji} are the rate constants with which n_i is reduced to form other states, k_{ij} are the rate constants with which n_i is increased through the relaxation of other states, n is the total number of possible states, and $i \neq j$. k_{ji} and k_{ij} are intrinsic rate constants for single reactions. The total population of all states must remain constant, since a decrease in the population of one state must lead to an increase in population for another. The general solution for the occupancy of a single population is the sum of exponential terms

$$n_i(t) = \sum_{j=1}^{n} c_{ij} e^{-k_j t}, \tag{3.5}$$

where c_{ij} are pre-exponential factors that can be positive or negative if the population n_i is increased or decreased, respectively, k_j are the observable rate constants, and $i \neq j$. The observable rate constant is associated with the lifetime of a species via $\tau = 1/k$. If the number of states in a reaction scheme is N, the temporal population of any state can be described with a sum of $N - 1$ exponents, although there may be at most $N(N - 1)$ intrinsic rate constants.

The absorbance of a specific state depends on it's relative population at any given time. The transient absorbance can be expressed as

$$\Delta A(\lambda, t) = \sum_{j=1}^{N-1} A_j(\lambda) n_j(t) - A_g(\lambda) n_j(t), \tag{3.6}$$

where the sum is taken over all intermediate states with absorbance A_j and population n_j. Since the transient absorbance is calculated relative to the ground state, and the excited state population is formed by excitation from the ground state, the reduction in the ground state absorption (A_g) must be included in equation 3.6. Since the excited state populations often change according to first order kinetics, the transient absorption can be mathematically expressed as

$$\Delta A(\lambda, t) = \sum_{j=1}^{N-1} b_j(\lambda) e^{-k_j t}, \tag{3.7}$$

where $b_j(\lambda)$ are the pre-exponential factors like in equation 3.5.[71] However, some processes may decay with different dynamics. For example, a stretched exponential function of the form $e^{-(kt)^\beta}$, where β is the stretching coefficient, can be used for fitting transient absorption decays associated with trap states.[75]

The transient absorption decays obtained from flash-photolysis or pump-probe measurements are fit using global fitting with function 3.7, fitting the decays at separate wavelengths with the same set of rate constants. This results in global lifetimes with different amplitudes for each component at different wavelengths. The transient absorption spectra can thus be deconvoluted by the separate exponential rate constants or lifetimes obtained for different processes. The wavelength dependent amplitudes of the separate exponential decay components can be drawn together to obtain decay component spectra. The sum of the amplitudes of the components gives the spectrum that is measured immediately after excitation.

4 Charge carrier dynamics in modified hematite photoanodes

This chapter forms the core of this Thesis, presenting the experimental results along with a discussion on their implications. Here the results obtained for hematite based photoanodes with transient absorption measurements are covered thoroughly. The first section discusses ultrafast recombination in hematite photoanodes and how it was changed after modifying the hematite layer or interfaces. The second section focuses on electron trapping and the timescales in which it is associated. The third section ties the long-lived hole population together with the PEC performance of the photoanodes by comparing water splitting dynamics from TAS measurements. All of the measurements presented in this chapter were performed in a three electrode photoelectrochemical cell with a Ag/AgCl reference electrode and platinum counter electrode in 0.1 M NaOH electrolyte, unless otherwise stated.

The absorption spectra and Tauc plots for a mesoporous hematite layer from **Paper I** are given in Figure 4.1. Since the layer is porous, the absorption coefficient was calculated using the sample thickness of 250 nm. However, this changes only the value of the absorption coefficient uniformly, and does not lead to a difference in the determination of optical band gap with Tauc plots.

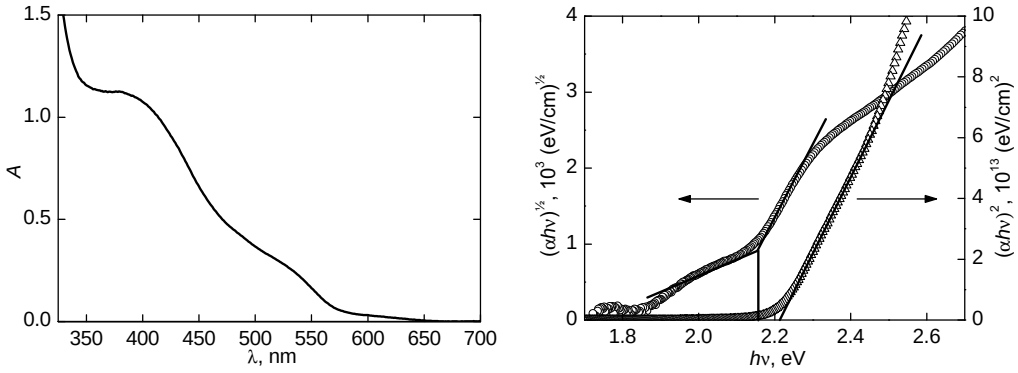

(a) Absorption spectrum. **(b)** Tauc plots.

Figure 4.1: (a) The absorption spectrum of a 250 nm thick mesoporous hematite layer from **Paper I** and (b) the associated Tauc plots.

The Tauc plots give 2.16 eV for the indirect and 2.22 eV for the direct band gaps. The indirect band gap was determined from the onset of the steepest slope due to a slight

interference wave in the absorption spectrum. Thus, both the indirect and direct band gaps are approximately 2.2 eV, corresponding to the literature value.[9,67]

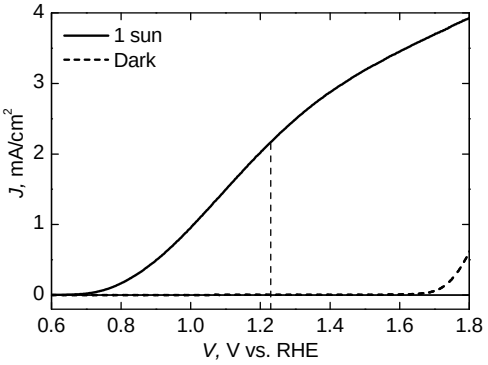

(a) Current density – voltage curves. The solid line is the photocurrent under simulated 1 sun illumination and the dashed line is under dark conditions. A vertical dashed line is used to mark the location of 1.23 V vs. RHE.

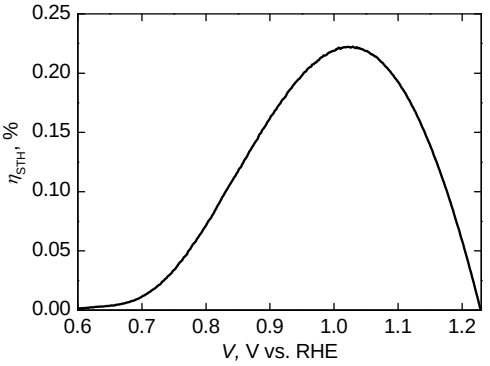

(b) Solar-to-hydrogen efficiency as calculated from the photocurrent values with equation 2.3. The photocurrents were measured in a three electrode cell, meaning that the efficiencies presented here are only for illustrative purposes.

Figure 4.2: (a) Current density – voltage curves of a PECVD grown hematite layer on top of ITO/FTO from **Paper IV** and (b) the associated solar-to-hydrogen efficiency as calculated with equation 2.3 in 1.0 M NaOH.

The photocurrent density – voltage curve of a PECVD grown hematite layer from **Paper IV** is presented in Figure 4.2a. The photocurrent onset voltage is 0.7 V versus the reversible hydrogen electrode (RHE), and reaches a value of 2.2 mA/cm^2 at 1.23 V vs. RHE. The shape is typical for a hematite electrode, with a plateau in the photocurrent observable at higher potential values. The solar-to-hydrogen efficiency as a function of bias voltage is presented in Figure 4.2b, calculated according to equation 2.3. However, the bias voltage is shown against the reference electrode, not the counter electrode. The maximum STH efficiency is 0.22 %, obtained at 1.02 V vs. RHE. The high onset potential that is typical for hematite photoanodes is one of the main reasons for the very low STH efficiency.

4.1 Ultrafast decay dynamics

Fast recombination in hematite has long been known to be a major problem for efficient PEC performance.[76–79] This section presents ultrafast transient absorption spectroscopy results for hematite photoanodes measured with the pump-probe method. The focus of the section is on ways in which the ultrafast decay dynamics are affected by recombination and modification of the hematite layer. The section begins with a discussion on the effects that excitation energy density has on the transient absorption dynamics, followed by a discussion on the fast recombination inherent to hematite, as measured for a reference hematite sample under an inert nitrogen atmosphere. The section concludes with a discussion on the ultrafast recombination observed in the publications included into this Thesis.

4.1.1 Excitation density

The effects of excitation energy density on the charge carrier dynamics in the sub-picosecond to nanosecond timescale are illustrated in Figure 4.3 for a PECVD grown hematite layer. Increasing the excitation density over a certain threshold value leads to faster sub-picosecond band to band recombination due to the increased charge carrier concentration.[53] Excitation densities under this threshold result typically in first-order kinetics for the fast recombination component that are not changed any more by reducing the excitation density. Increasing the energy density leads also to an increase in the transient absorption, as shown in Figure 4.3a. The energy density at which the fast recombination accelerates occurs at > 1 mJ/cm^2, as can be seen from the normalized transient absorption decays in Figure 4.3b. This limit corresponds to a single pulse energy of 2 μJ when focused to a 0.5 mm diameter spot on the sample surface. To avoid this increased recombination all transient absorption measurements were performed with an excitation density of 100–1000 μJ/cm^2.

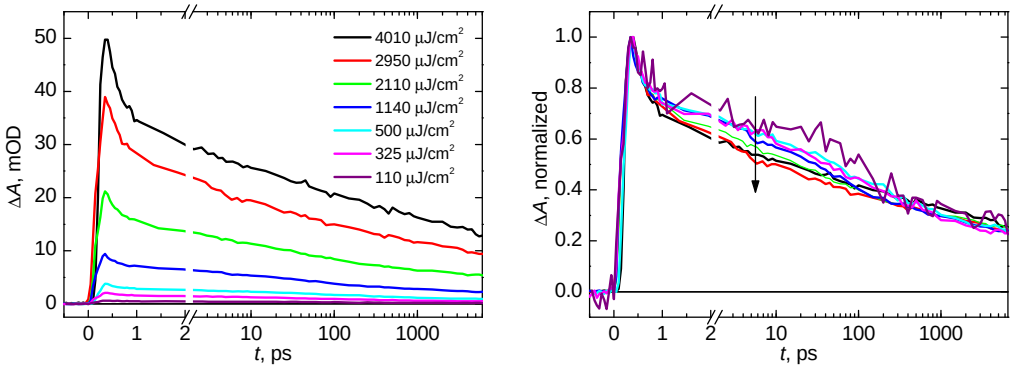

(a) Transient absorption decays. **(b)** Normalized transient absorption decays.

Figure 4.3: Effect of excitation energy density with 500 nm excitation on the pump-probe decay dynamics in hematite under nitrogen flow, (a) as-measured and (b) normalized transient absorption decays at 580 nm.

The excitation wavelength for all transient absorption measurements was in the range of 355–500 nm. The energy of an excitation photon corresponds to 2.5–3.5 eV when calculated with equation 2.2. This equals to 5×10^{-19} J per photon, leading to a photon flux of roughly 10^{15} photons per cm^2 per excitation pulse. Since the excitation frequency was 500 Hz, the average excitation flux used is approximately of the same order of magnitude as the whole portion of the AM1.5G reference spectrum (Figure 2.2) absorbed by hematite. This means that the excitation energy densities used roughly corresponds to exciting the sample with visible light illumination.

4.1.2 Fast recombination

The transient absorption spectra for pristine hematite under nitrogen flow are shown in Figure 4.4. They are drawn as 2D colormaps with the color indicating the absorption change. Spectra are shown for excitation at 365 nm in Figure 4.4a and at 425 nm in Figure 4.4b with an excitation density of 500 μJ/cm^2 for both wavelengths. The transient absorption spectra and dynamics remain unchanged with different excitation wavelengths (same sample was also measured using 500 nm excitation, not shown), supporting the

conclusion that the valence to conduction band transition in hematite is due to electron transfer from O 2p to Fe 3d states, leading to only a single type of hole (see section 2.2 for further discussion). The differences in the amount of absorption change between the excitation wavelengths are due to the increased absorption of the sample and reduced number of photons at 365 nm, compared to those at 425 nm.

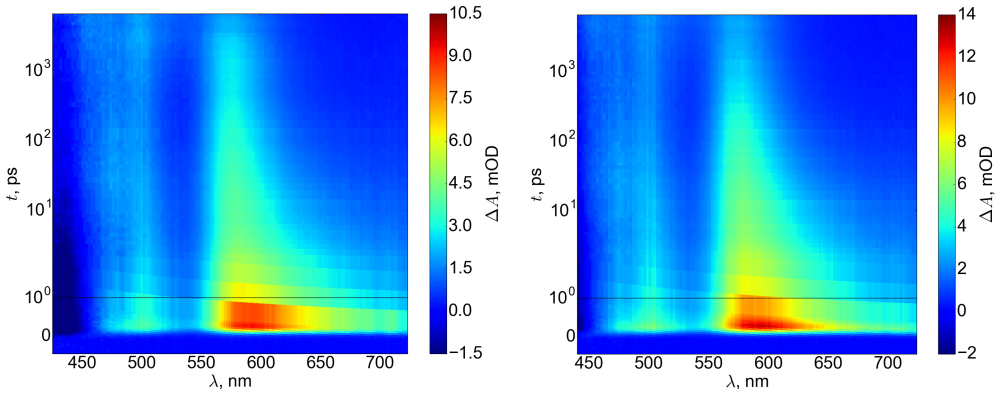

(a) Excitation at 365 nm. **(b)** Excitation at 425 nm.

Figure 4.4: Pump-probe transient absorption spectra of hematite under nitrogen flow, shown as 2D colormaps that have been corrected for group velocity dispersion (chirp) with 500 μJ/cm^2 excitation density at (a) 365 nm and (b) 425 nm.

The most prominent feature of the transient absorption spectra is the positive absorption change band localized around 580 nm, with a smaller positive band at 500 nm and ground state bleach below 450 nm. The 580 nm feature was previously proposed to be mainly due to the positive absorption of excited conduction band electrons.[80] The transient absorption band at 580 nm has a diffuse boundary at longer and a sharper boundary at shorter wavelengths. The sharp boundary was the main reason for this assignment in Ref. [80], since the valence band density of states is much more continuous than the density of states in the conduction band.

Assigning the transient absorption feature at 580 nm to the absorption of photoexcited valence band holes is supported by a larger amount of evidence. Huang et al. [77] first showed that holding a hematite photoanode under cathodic bias leads to a negative steady state absorption below 470 nm, while holding under anodic bias leads to a positive steady state absorption band at 580 nm, matching the features observed with transient absorption spectroscopy. Cathodic bias leads to an accumulation of conduction band electrons into hematite, bleaching the band to band (ground state) absorption along with inducing a smaller positive absorption at higher wavelengths due to the absorption of the conduction band electrons. On the other hand, anodic bias leads to an accumulation of valence band holes, with a localized positive absorption band. Barroso et al. [81] later showed that the positive steady state absorption increases linearly with increased bias voltage above the flat band potential, indicating that the positive absorption is associated with oxidized states within the depletion region that are possibly related to oxygen vacancies within the hematite lattice. Klahr et al. [82] later correlated this positive absorption with the accumulation of holes in surface states observed with electrochemical impedance spectroscopy and cyclic voltammetry.[83,84] Using operando infrared spectroscopy the same surface state was recently observed by Zandi and Hamann [85] to be a water splitting

intermediate (Fe^{IV}=O) that is formed after hole transfer to a surface hydroxyl group. However, the Fe^{IV}=O species was not observed to form at bias voltages as low as 0.8 V vs. RHE, where the positive absorption was already observable by Barroso et al.[81] Thus the 580 nm absorption feature is probably formed from the absorption of both water splitting intermediates and oxidized states within the depletion region.

Figure 4.5 shows the transient absorption spectra at select delay times, globally fitted four exponential decay component spectra, and transient absorption decays at select wavelengths. The spectra, fits, and decays in Figures 4.5a, 4.5b, and 4.5c, respectively, have been corrected for chirp. The sum of the four decay component spectra, denoted with "at 0 ps" in Figure 4.5b, matches well with the maximum transient absorption spectrum obtained at a delay of 0.3 ps. The fastest decay component with a lifetime of 0.79 ps also has the largest amplitude. This means that a majority of the charge carriers recombine within the first picosecond as a result of the localized nature of the photoexcited charge carriers in hematite. The longest decay component in Figure 4.5b does not have a definitive lifetime, since the lifetime for the fit is much longer (> 10 ns) than the pump-probe system's maximum allowed delay line length (6.5 ns). The long component spectrum matches that at the maximum delay time, shown as the transient absorption spectrum at 5 ns in Figure 4.5a. The transient absorption decays in Figure 4.5c illustrate the different processes occurring in bulk hematite. The ground state bleach can be observed clearly in the decay at 435 nm in the whole measurement time scale, however, a longer lived component of the bleach is visible at also 500 and 535 nm with a lifetime of 1.8 ns. The decays at 580 nm and 700 nm are composed primarily of recombination, with a half-life ($\tau_{1/2}$) of 2–3 ps. The fast decay of the 580 nm transient absorption band supports the conclusion that this feature is mainly composed of the absorption of an excited and localized hole in bulk hematite that recombines rapidly.

The picosecond to nanosecond transient absorption dynamics of hematite do not change much as a function of applied bias voltage or after changing the dopants coming from the substrate in high temperature annealing. The transient absorption decays at 580 nm of a pristine mesoporous hematite layer held under different bias voltages vs. RHE are shown in Figure 4.6a. The decays are indistinguishable from each other, with half-lives in the range of $\tau_{1/2} = 3 - 5$ ps. The half-lives are similar to those observed at 580 nm for a PECVD grown hematite layer held under a nitrogen atmosphere.

The transient absorption decays at 565 nm of PECVD grown hematite layers on different substrates at 1.23 V vs. RHE are shown in Figure 4.6b. In this case the modification of the FTO substrate with a sputtered ITO layer leads to a change in the types of dopants present in the hematite layer, with the high temperature annealing doping the hematite layer with indium instead of tin. However, the change in doping does not affect the picosecond to nanosecond charge carrier dynamics, with the recombination occurring with a half-life of $\tau_{1/2} = 2.2 - 2.5$ ps.

Incorporation of a PECVD grown TiO_2 overlayer accelerates the picosecond timescale recombination of a PECVD hematite layer selectively excited with 475 nm light through the TiO_2 layer, shown in Figure 4.6c. The increased recombination is due to the valence band of TiO_2 being at a lower energy than the valence band of hematite (see Figure 2.3), blocking hole transfer into the TiO_2 layer. On the other hand, intercalating a PECVD grown few-layer graphene layer between the two metal oxide layers reduces the ultrafast recombination in the hematite layer due to hole transfer into the graphene layer, reducing interfacial recombination. The graphene layer is also proposed to enable more efficient electron transfer from TiO_2 to hematite due to reduced interfacial recombination.

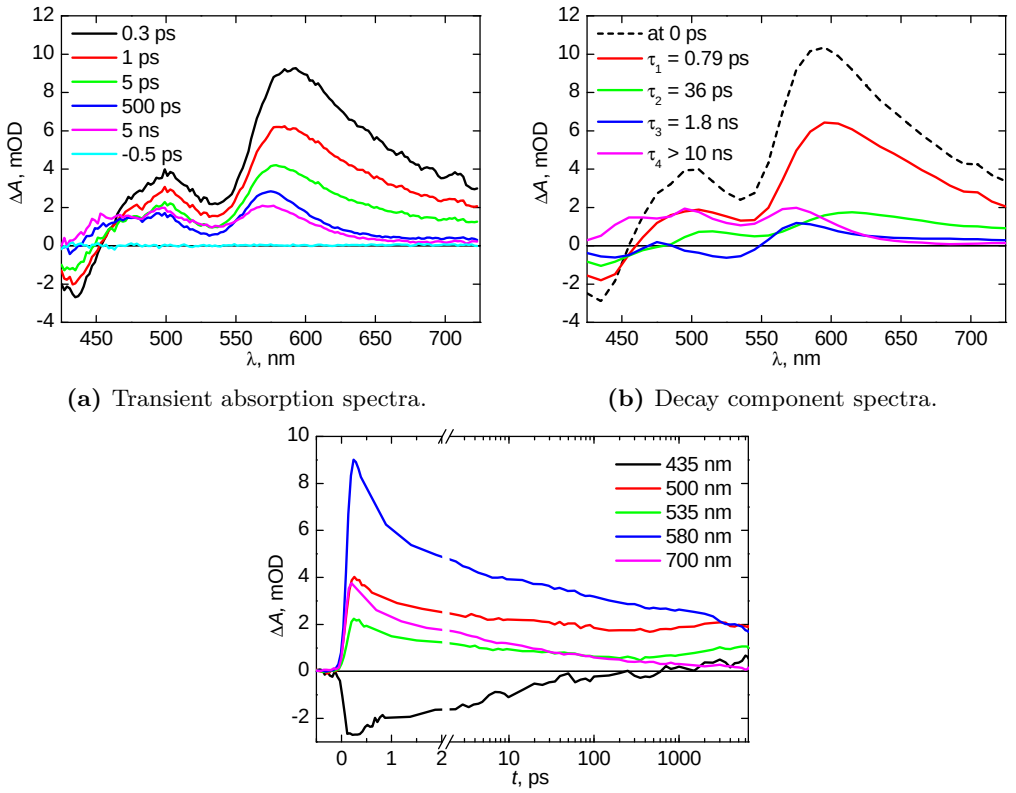

(a) Transient absorption spectra.

(b) Decay component spectra.

(c) Transient absorption decays.

Figure 4.5: Pump-probe (a) transient absorption spectra, (b) decay component spectra, and (c) transient absorption decays of a PECVD grown hematite layer with 500 μJ/cm^2 excitation density at 365 nm under nitrogen flow. The time scale is linear until 2 ps and logarithmic at longer delays in (c).

Ultrafast bulk recombination in hematite is one of the main reasons for the low photoelectrochemical performance shown in Figure 4.2. Since a majority of bulk charge carriers recombine within a few picoseconds, there is no way for them to take part in the water oxidation or reduction reactions. Retarding ultrafast recombination should be taken into account in photoanode design.

Passivation of interfacial states has been shown to retard recombination, for example with an interfacial graphene layer as shown in Figure 4.6c. Passivation reduces the amount of interfacial states that can act as efficient recombination centers. Another way to passivate hematite is by utilizing ultrathin metal oxide under- or overlayers, such as ALD grown interfacial TiO_2, Al_2O_3, or Ga_2O_3 layers.[40,41,43] Passivation of surface recombination states increases the onset potential of hematite photoanodes, whereas doping induced from underlayers can increase the photocurrent. Overlayers may also affect the water oxidation dynamics, discussed more in depth in Chapter 4.3. Passivation with TiO_2 overlayers was employed in **Paper II**, where both 30 nm and 85 nm thick ALD TiO_2 layers were observed to retard recombination in the tens of picoseconds timescale. Doping induced effects were studied in **Paper IV**, however the doping did not have an appreciable effect on the sub-picosecond to nanosecond decay dynamics, as shown in Figure 4.6b. The TiO_2

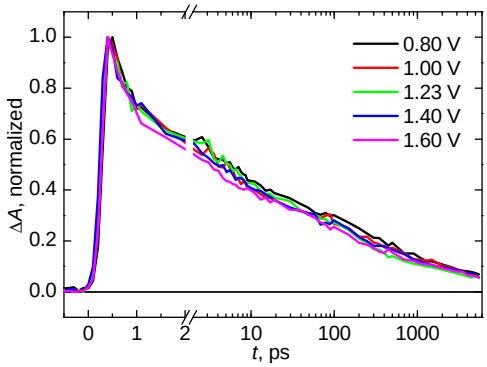

(a) 580 nm decay of mesoporous hematite biased vs. RHE with 120 μJ/cm^2 excitation density at 355 nm from **Paper I**.

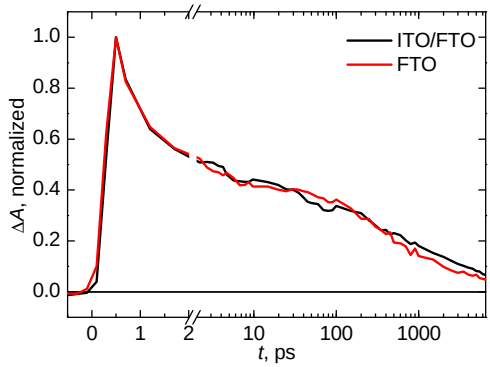

(b) 565 nm decay of PECVD grown hematite on different substrates at 1.23 V vs. RHE with 1000 μJ/cm^2 excitation density at 355 nm from **Paper IV**.

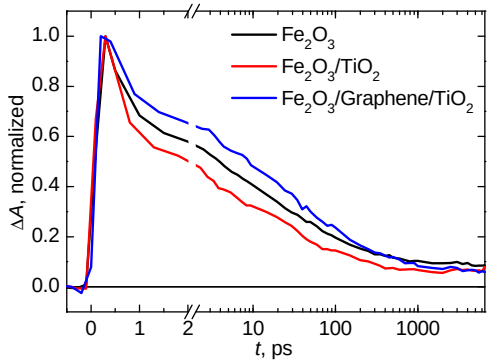

(c) 650 nm decay of PECVD grown hematite and TiO_2 with intercalated few-layer graphene at 1.23 V vs. RHE with 400 μJ/cm^2 excitation density at 475 nm from **Paper III**.

Figure 4.6: Normalized pump-probe transient absorption decays.

overlayers employed in **Paper III** were thicker than typical passivation layers, since they were designed to form heterojunctions with photoelectrochemical performance from both metal oxide layers. Passivation of interstitial recombination sites and improved charge transfer dynamics were achieved with the intercalated few-layer graphene layer.

Increasing charge carrier separation will also affect the photoelectrochemical performance. One way to optimize charge carrier separation is by nanostructuring of the material. In optimized nanostructures the distance that photogenerated holes need to diffuse from where they are generated to the semiconductor-electrolyte interface is minimized. Utilizing nanoscale structures at the interface typically leads to a depletion of charge carriers in the surface layer, meaning that the holes need to specifically diffuse to reach the SEI. Since the electron diffusion length is larger than the hole diffusion length in hematite, thin nanorod-like or mesoporous structures will enable electron extraction from the photoanode, while simultaneously minimizing the hole diffusion length. A mesoporous structure was employed in **Paper I** to minimize the distance from the hole generation sites to the SEI.

4.2 Electron trapping

The picosecond to nanosecond transient absorption dynamics of a mesoporous hematite–titania photoanode differ gradually from that of pristine hematite when a bias voltage is applied. A negative component that is formed instantaneously after excitation and lasts longer than the measurement range of 6 ns can be seen with increased bias voltages in the transient absorption decays, as presented in Figure 4.7a. This component turns into a visible bleach within a few hundred picoseconds that is centered around 580 nm, seen in the four exponential decay component spectra at 1.60 V vs. RHE, presented in Figure 4.7b.

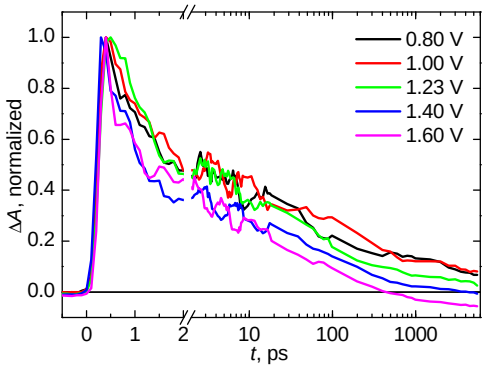

(a) Transient absorption decays biased vs. RHE.

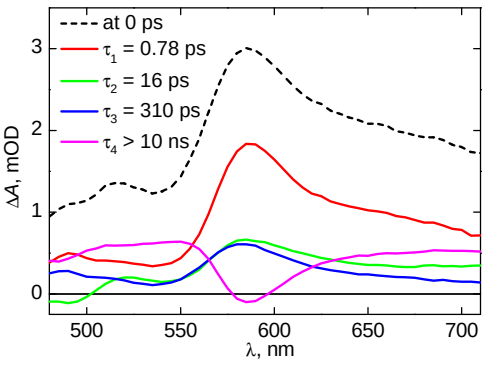

(b) Decay component spectra at 1.60 V vs. RHE.

Figure 4.7: Pump-probe (a) transient absorption decays at 580 nm as a function of bias voltage vs. RHE and (b) the decay component spectra at 1.60 V vs. RHE of a mesoporous hematite–titania mixture (15 % TiO_2) with 120 μJ/cm^2 excitation density at 355 nm from **Paper I**.

The formation of this long-lived bleach due to increasing anodic bias is clearly visible when only the longest lived ($\tau > 10$ ns) components are drawn as a function of bias voltage, presented in Figure 4.8a. The bleach at 580 nm is also associated with an increase in the absorption in the wavelength ranges 480–550 nm and 620–710 nm. The immediate formation of the bleach is illustrated in Figure 4.8b, where the difference immediately after excitation between the spectra measured without electrical connection to the photoanode and with a bias of 1.60 V vs. RHE is nearly identical with the $\tau > 10$ ns component spectrum at 1.60 V vs. RHE.

The flash-photolysis transient absorption decay at 575 nm for the same photoelectrode at 1.60 V vs. RHE is shown in Figure 4.9a along with the two exponential global fit with lifetimes $\tau_1 = 0.3$ ms and $\tau_2 = 360$ ms (τ_1 fit with a small energy distribution model, see Ref. [86] for details). The corresponding decay component spectra at 1.60 V vs. RHE are presented in Figure 4.9b.

The τ_1 component spectra as a function of bias voltage are presented in Figure 4.10a. The bleach component is visible still in the millisecond time scale, and the spectrum obtained with flash-photolysis matches the $\tau > 10$ ns component from the pump-probe measurements, as shown in Figure 4.10b. This means that the flash-photolysis measurement only sees the tail of the bleach component.

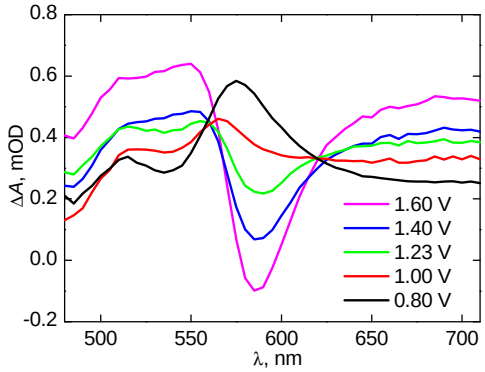

(a) $\tau > 10$ ns decay component spectra biased vs. RHE.

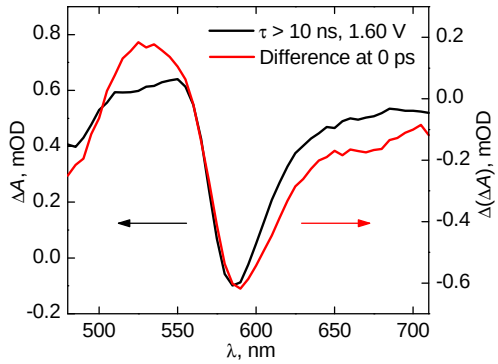

(b) $\tau > 10$ ns decay component spectrum at 1.60 V vs. RHE and the difference spectrum at 0 ps between no electrical connection and at 1.60 V vs. RHE.

Figure 4.8: (a) Long-lived decay components with $\tau > 10$ ns as a function of bias voltage vs. RHE and (b) the difference in spectra immediately after excitation (at 0 ps) without electrical connection and at 1.60 V vs. RHE of a mesoporous hematite–titania mixture (15 % TiO_2) with 120 μJ/cm^2 excitation density at 355 nm from **Paper I**.

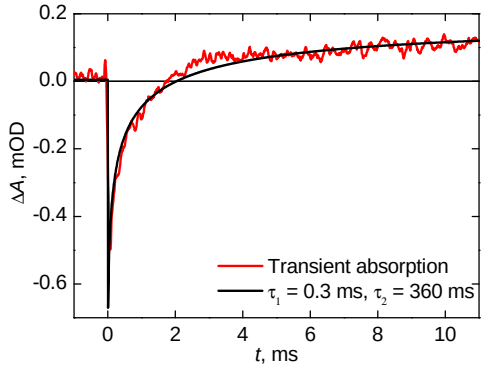

(a) Transient absorption decay at 1.60 V vs. RHE.

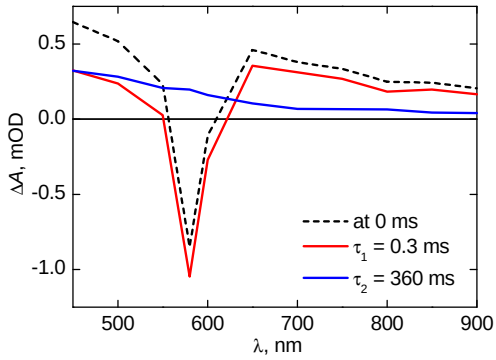

(b) Transient absorption decay component spectra at 1.60 V vs. RHE.

Figure 4.9: (a) Flash-photolysis transient absorption decay at 580 nm and (b) the decay component spectra of a mesoporous hematite–titania mixture (15 % TiO_2) biased at 1.60 V vs. RHE with 400 μJ/cm^2 excitation density at 355 nm from **Paper I**, measured with the mLFP-111 system with 30–80 averages.

The negative component is suggested to arise due to electron trapping into oxidized electron states in the space charge region in **Paper I**. The trapping being observed with the mixed hematite–titania photoanode, but not with the reference hematite photoanode, was proposed to be due to reduced recombination due to the formation of a pseudobrookite (Fe_2TiO_5) surface layer that enhances charge separation.[87] Similar trapping was also observed by Pendlebury et al. [79] in Si-doped hematite.

This explanation is compatible with electrons excited within the space charge region becoming rapidly trapped into vacant surface states, as illustrated in Figure 2.3. The

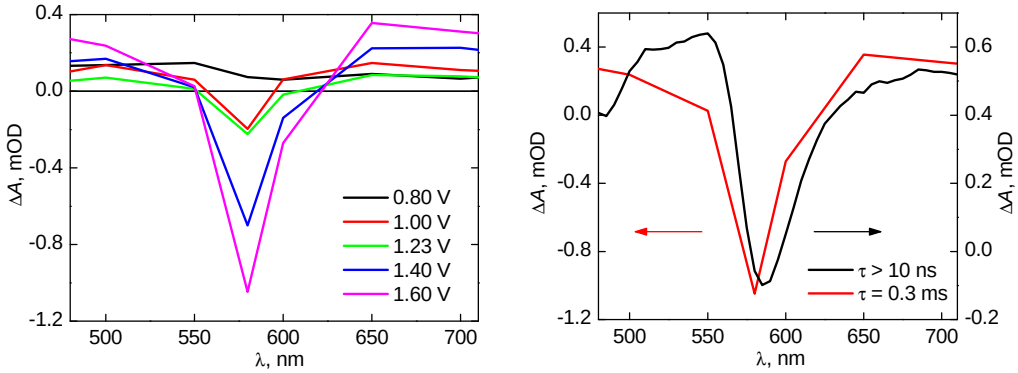

(a) $\tau = 0.3$ ms decay component spectra biased vs. RHE.

(b) $\tau > 10$ ns and $\tau = 0.3$ ms decay component spectra at 1.60 V vs. RHE.

Figure 4.10: (a) Flash-photolysis fast $\tau = 0.3$ ms decay component spectra biased vs. RHE and (b) longest lived pump-probe ($\tau > 10$ ns, see Figure 4.8a) and fast lived flash-photolysis ($\tau = 0.3$ ms) decay component spectra at 1.60 V vs. RHE of a mesoporous hematite–titania mixture (15 % TiO_2) with 400 $\mu J/cm^2$ excitation density at 355 nm from **Paper I**.

surface states may be water splitting intermediates, specifically the Fe^{IV}=O state observed by Zandi et al. [85]. Since the sample is excited with 355 nm light, it is probable that an electron is not directly excited into this state. Rather, the electron is excited into the conduction band, after which it rapidly thermalizes to the conduction band edge and is trapped by a surface state. Trapping of the electron on the surface explains the very long lifetime of the bleach component that is observed on timescales spanning 9 orders of magnitude. This interpretation is supported by the observation of a bleaching of steady state absorbance at 572 nm associated with electrons filling surface states in hematite.[82] The recovery from the bleach is proposed to be due to a hole transfer from the valence band into the surface state, reforming the Fe^{IV}=O state. Detrapping by electron extraction from the surface state into the external circuit is also possible, although this does not explain the faster decay process observed for holes at 650 nm with the same lifetime as the detrapping, illustrated later in Figure 4.11.

Electron trapping occurs on a faster time scale than the ultrafast recombination. It can retard the recombination discussed in Chapter 4.1.2 since it is a competitive pathway for conduction band electrons. Anodic bias voltage increased the transient absorption of the long-lived pump-probe component in mesoporous hematite in the whole probe range by approximately up to 50 % due to the formation of long-lived holes in the space charge layer, as shown in **Paper I**. However, the ultrafast electron trapping observed for the mesoporous hematite–titania photoanode increased absorption in the wavelength ranges 480–550 nm and 620–710 nm by more than 100 %, as shown in Figure 4.8a, attributed to valence band holes surviving from ultrafast recombination as a direct result of electron trapping. Electron trapping can thus be shown to increase the photoelectrochemical performance due to improved charge separation. If the electron trapping is mainly occurring into water splitting intermediates, as discussed earlier, it is probable that increased electron trapping is indicative of more active surface sites in the photoanode.

4.3 Water oxidation

Water splitting occurs on the milliseconds to seconds timescale due to slow reaction dynamics on the hematite surface. The flash-photolysis transient absorption decays of O_2-plasma treated PECVD grown hematite at 575 nm and 650 nm biased at 1.50 V vs. RHE are shown in Figure 4.11. The black lines show the global two-exponential fits with a fast stretched exponential component of $\tau_1 = 0.12$ ms, with exponential stretching factor $\beta = 0.74$, and a long-lived exponential component of $\tau_2 = 320$ ms. The recovery of the bleach component observed at 575 nm is due to the recombination or electron detrapping process discussed earlier. The transient absorption decay component observed at 650 nm with the same lifetime is due to valence band holes again filling the surface state, simultaneously decreasing the positive transient absorption due to photoexcited holes in the valence band. The long-lived decay with $\tau = 320$ ms is visible at both wavelengths, and is attributed to long-lived valence band holes taking part in the OER.

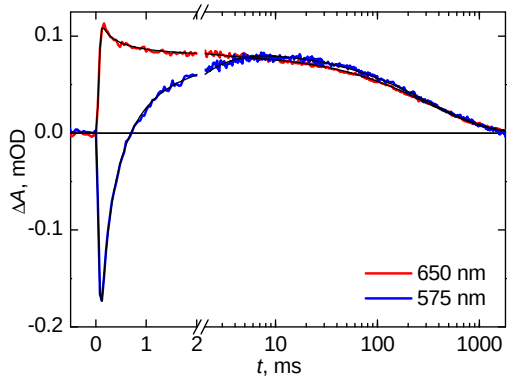

Figure 4.11: Flash-photolysis transient absorption decays of O_2-plasma treated PECVD grown hematite at 575 nm and 650 nm biased at 1.50 V vs. RHE with 540 μJ/cm^2 excitation density at 355 nm, measured with the in-lab system with 300 averages. The black lines show the global two-exponential fits with $\tau_1 = 0.12$ ms stretched exponential ($\beta = 0.74$) and $\tau_2 = 320$ ms.

The amplitude at 50 ms of the long-lived hole absorption at 650 nm correlates with the photocurrent of a mesoporous hematite–titania mixture (15 % TiO_2), presented in Figure 4.12. Also in **Paper IV** a doubling in the amplitude of long-lived holes coincided with a doubling of photocurrent.

The slow transfer dynamics of the long-lived holes has been described as the rate-limiting step of the OER.[88] Back-electron recombination is a competitive process to the OER at low bias voltages,[89] reducing the long-lived hole lifetime observed with transient absorption spectroscopy, as shown in Figure 4.13. The amplitude of the long-lived hole absorption increases with bias voltage due to a widening of the space charge region increasing the hole collection distance. No long-lived holes are observed with bias voltages below the photocurrent onset potential of 0.9 V vs. RHE, shown in Figure 4.12. The transient absorption rate constant of the long-lived hole decay ($k_{ta} = (\tau_{ta})^{-1}$) can be correlated with the OER rate constant (k_{oer}) and back-electron recombination rate constant (k_{ber}) with

$$k_{ta} = (\tau_{ta})^{-1} = k_{oer} + k_{ber}. \tag{4.1}$$

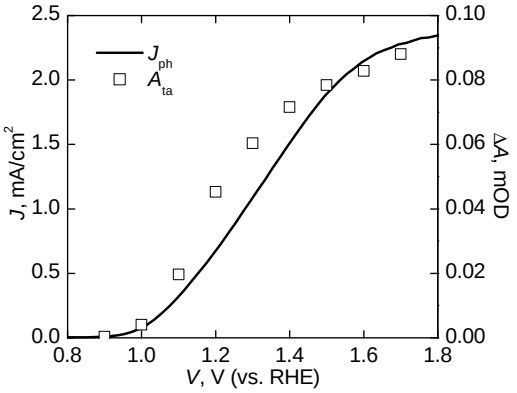

Figure 4.12: Photocurrent density–voltage curve and flash-photolysis amplitudes at 50 ms of the long-lived hole absorption at 650 nm of a mesoporous hematite–titania mixture (15 % TiO_2) biased vs. RHE with 400 μJ/cm^2 excitation density at 355 nm, measured with the mLFP-111 system with 30–80 averages.

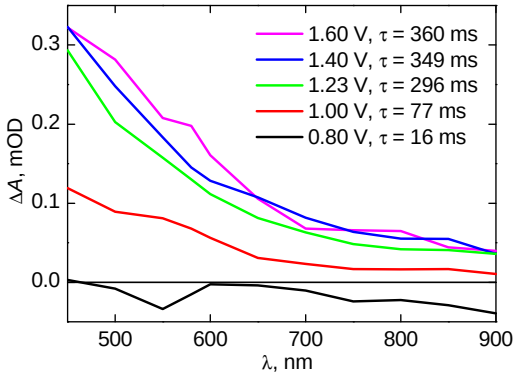

Figure 4.13: Flash-photolysis long decay component spectra and lifetimes of a mesoporous hematite–titania mixture (15 % TiO_2) biased vs. RHE with 400 μJ/cm^2 excitation density at 355 nm from **Paper I**, measured with the mLFP-111 system with 30–80 averages.

However, at applied bias voltages above 1.40 V vs. RHE the back electron recombination is retarded significantly. This means that the measured transient absorption rate for the long-lived hole component matches the water oxidation rate. The water oxidation rates at high applied bias voltage for several different hematite photoanodes are listed in Table 4.1. The transient absorption spectra were measured only at 1.23 V vs. RHE for the PECVD hematite samples in **Paper IV**, so the OER rate constant listed in Table 4.1 is overestimated due to back-electron recombination.

The water oxidation rate is much slower for bare hematite than it is for the samples that have been modified with TiO_2. The transient absorption rate constants for long-lived holes in hematite have been between 0.3–0.7 s^{-1} in previous publications,[88–90] and the rate constant of 1.1 s^{-1} obtained for PECVD grown hematite in **Paper II** is similar to the previously reported values.

The water oxidation rate constant increases noticeably when a TiO_2 overlayer is deposited on top of the hematite photoanode. This is due to the fact that photogenerated holes in

Table 4.1: Transient absorption amplitudes, lifetimes, and water oxidation rates constants of hematite samples under 355 nm laser excitation.

Sample	Publication	Voltage (V vs. RHE)	τ_{ta} (ms)	k_{oer} (s^{-1})
α-Fe_2O_3 with 15 % TiO_2	**Paper I**	1.60	360	2.78
α-Fe_2O_3	**Paper II**	1.60	900	1.11
35 nm TiO_2 on α-Fe_2O_3	**Paper II**	1.60	550	1.82
80 nm TiO_2 on α-Fe_2O_3	**Paper II**	1.60	330	3.0
α-Fe_2O_3 on FTO	**Paper IV**	1.23	310	3.22
α-Fe_2O_3 on ITO/FTO	**Paper IV**	1.23	360	2.78

TiO_2 exhibit faster reaction dynamics than in hematite.[88] This is seen with the increasing rate constant from 1.82 s^{-1} with 35 nm thick overlayers to 3.0 s^{-1} with 80 nm thick overlayers.

The water oxidation rate constant for a mesoporous hematite photoanode mixed with 15 % TiO_2 is 2.78 s^{-1}, almost the same as for the photoanode with a thick TiO_2 overlayer. This also matches the previously published methanol oxidation rate constant with hematite photoanodes.[88] The fast reaction dynamics with this photoanode is assigned to faster hole transfer from hematite due to the formation of a pseudobrookite (Fe_2TiO_5) mixed metal oxide surface layer. The incorporation of titanium in the pseudobrookite layer leads to similar reaction dynamics as those observed for bare and overlayer TiO_2.[88]

4.4 Charge carrier lifetimes

The charge transfer processes observed in the transient absorption measurements in this Thesis are illustrated in Figure 4.14, whereas the lifetimes of the processes are given in Table 4.2.

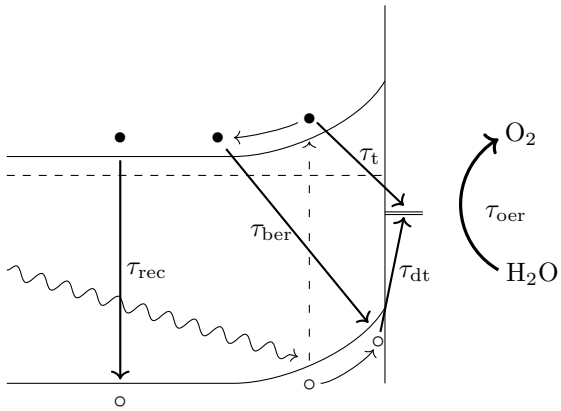

Figure 4.14: Charge carrier transfer and reaction rates in s^{-1} that were observed with transient absorption spectroscopy.

Electron trapping (τ_t) was observed instantaneously in the pump-probe measurements, indicating that it is due to either direct excitation from the valence band into the trap state or, more probably, rapid trapping of a thermalized electron in the conduction band. Bulk recombination (τ_{rec}) mostly occurred within one picosecond, although recombination continued into longer delay times. Even though electron detrapping (τ_{dt}) probably

Table 4.2: Rates constants for different processes in hematite photoanodes detected with transient absorption spectroscopy. Back-electron recombination lifetimes and rates approximated from **Paper I**.

Process	Symbol	Lifetime (s)
Electron trapping	τ_{t}	$< 10^{-13}$
Bulk recombination	τ_{rec}	0.78×10^{-12}
Electron detrapping	τ_{dt}	$\leq 0.12 \times 10^{-3}$
Back-electron recombination	τ_{ber}	$0.01 - 10$
Water oxidation	τ_{oer}	$0.33 - 0.90$

occurred already in the nanosecond to microsecond time scales due to heterogeneity of the surface traps, the flash photolysis system could still see the tail of the detrapping process. The lifetime obtained for the tail of detrapping gives an upper limit to the lifetime of the detrapping process. The detrapping was proposed to be due to hole recombination from the valence band into the surface trap state or water splitting intermediate, although electron detrapping by extraction into the external circuit is a possible alternative detrapping route especially at high bias voltages. Back-electron recombination (τ_{ber}) of conduction band electrons with long-lived valence band holes within the space charge region was also observed in **Paper I**, from which the lifetimes are taken from. The BER lifetime is dependent on the amount of bias voltage applied to the working electrode, with the lifetime assumed to be zero at 1.60 V vs. RHE bias. Finally, the long-lived hole lifetimes of hematite photoanodes at high applied bias voltages are given as the lifetime of the OER (τ_{oer}). It is impossible to accurately determine if the OER pathway for long-lived valence band holes occurs by direct transfer from the valence band or via water splitting intermediate surface states in the hematite.

5 Conclusions

In this Thesis transient absorption spectroscopy was used to study the charge carrier behavior in hematite photoanodes in the subpicosecond to seconds time scales. Transient absorption measurements under operating conditions revealed electron trapping into surface states instantaneously after excitation, ultrafast recombination with a lifetime under one picosecond, hole transfer to surface states in a timescale between nanoseconds and milliseconds, and water oxidation with long-lived surface holes in the hundreds of milliseconds timescale. The water oxidation reaction in hematite may advance through the oxidation of surface adsorbed hydroxyl species via trap states or through direct hole transfer from the valence band. Whichever route the OER advances through, the probing of long-lived holes in hematite offered direct monitoring of the water oxidation reaction rates.

Electron trapping was observed in **Paper I** to be a competitive pathway for excited conduction band electrons, reducing the amount of ultrafast charge carrier recombination. Since ultrafast recombination is deleterious with regard to water splitting performance, the electron trapping aided in the charge carrier separation and lead to greatly increased photocurrent values due to an increased amount of long-lived holes and improved oxygen evolution reaction dynamics.

The formation of heterojunctions with passivating ALD grown TiO_2 overlayers in **Paper II** was observed to increase charge carrier separation and retard fast recombination. Faster water oxidation dynamics were also observed for the passivated photoanodes since hole transfer to water splitting intermediates from TiO_2 occurs more rapidly than from hematite. On the other hand, growing thicker PECVD grown TiO_2 overlayers in **Paper III** resulted in increased recombination due to the formation of interfacial recombination sites. These recombination sites were passivated with an intercalated graphene layer that also increased electron transfer between the two metal oxide layers.

The amount of long-lived holes grew two-fold when the hematite layer was grown on ITO covered FTO substrates in **Paper IV**, coinciding with a doubling of the photocurrent. The dynamics of both ultrafast recombination and water oxidation reaction remained the same on both substrates. The improved hole collection and photoelectrochemical performance were thus assigned to improved conductivity in the In and Sn codoped hematite layer. The higher conductivity lead to more efficient charge carrier separation, possibly simultaneously retarding back-electron recombination due to the improved electron extraction from the photoanode.

The results of this Thesis indicate that the modification of hematite has a profound effect on the charge carrier behaviour. However, transient absorption spectroscopy cannot directly distinguish the water splitting intermediates on the hematite surface. The intermediates could possibly be identified by combining transient absorption spectroscopy

with time-resolved infrared spectroscopy. Future breakthroughs in advancing the photoelectrochemical performance of hematite can be expected after the rate limiting steps in water oxidation on hematite surfaces are identified. By optimizing the reactivity of these rate limiting steps, water splitting with hematite photoanodes can possibly overcome the currently limited efficiency.

Bibliography

[1] IEA, *Key World Energy Statistics 2016*. IEA, 2016. [Online]. Available: http://www.iea.org/publications/freepublications/publication/KeyWorld2016.pdf

[2] N. S. Lewis and G. Crabtree, *Basic research needs for solar energy utilization: report of the basic energy sciences workshop on solar energy utilization, April 18-21, 2005*. US Department of Energy, Office of Basic Energy Science, 2005. [Online]. Available: https://science.energy.gov/~/media/bes/pdf/reports/files/Basic_Research_Needs_for_Solar_Energy_Utilization_rpt.pdf

[3] N. S. Lewis and D. G. Nocera, "Powering the planet: Chemical challenges in solar energy utilization," *Proceedings of the National Academy of Sciences*, vol. 103, no. 43, pp. 15 729–15 735, 2006. [Online]. Available: http://dx.doi.org/10.1073/pnas.0603395103

[4] R. A. Betts, C. D. Jones, J. R. Knight, R. F. Keeling, and J. J. Kennedy, "El Nino and a record CO_2 rise," *Nature Climate Change*, pp. 806–810, 2016. [Online]. Available: http://dx.doi.org/10.1038/nclimate3063

[5] D. Hartmann, A. Klein Tank, M. Rusticucci, L. Alexander, S. Brönnimann, Y. Charabi, F. Dentener, E. Dlugokencky, D. Easterling, A. Kaplan, B. Soden, P. Thorne, M. Wild, and P. Zhai, "Observations: Atmosphere and surface," in *Climate Change 2013: The Physical Science Basis. Contribution of Working Group I to the Fifth Assessment Report of the Intergovernmental Panel on Climate Change*, T. Stocker, D. Qin, G.-K. Plattner, M. Tignor, S. Allen, J. Boschung, A. Nauels, Y. Xia, V. Bex, and P. Midgley, Eds. Cambridge, United Kingdom and New York, NY, USA: Cambridge University Press, 2013, book section 2, pp. 159–254. [Online]. Available: www.climatechange2013.org

[6] R. van de Krol and M. Grätzel, Eds., *Photoelectrochemical Hydrogen Production*. New York: Springer US, 2012. [Online]. Available: http://dx.doi.org/10.1007/978-1-4614-1380-6

[7] A. Fujishima and K. Honda, "Electrochemical evidence for the mechanism of the primary stage of photosynthesis," *Bulletin of the Chemical Society of Japan*, vol. 44, no. 4, pp. 1148–1150, 1971. [Online]. Available: http://dx.doi.org/10.1246/bcsj.44.1148

[8] A. Fujishima and K. Honda, "Electrochemical photolysis of water at a semiconductor electrode," *Nature*, vol. 238, pp. 37–38, 1972. [Online]. Available: http://dx.doi.org/10.1038/238037a0

[9] A. Murphy, P. Barnes, L. Randeniya, I. Plumb, I. Grey, M. Horne, and J. Glasscock, "Efficiency of solar water splitting using semiconductor electrodes," *International Journal of Hydrogen Energy*, vol. 31, no. 14, pp. 1999–2017, 2006. [Online]. Available: http://dx.doi.org/10.1016/j.ijhydene.2006.01.014

[10] K. Sivula, F. Le Formal, and M. Grätzel, "Solar water splitting: progress using hematite (α-Fe_2O_3) photoelectrodes," *ChemSusChem*, vol. 4, no. 4, pp. 432–449, 2011. [Online]. Available: http://dx.doi.org/10.1002/cssc.201000416

[11] K. Sivula, "Metal oxide photoelectrodes for solar fuel production, surface traps, and catalysis," *The Journal of Physical Chemistry Letters*, vol. 4, no. 10, pp. 1624–1633, 2013. [Online]. Available: http://dx.doi.org/10.1021/jz4002983

[12] M. P. Dare-Edwards, J. B. Goodenough, A. Hamnett, and P. R. Trevellick, "Electrochemistry and photoelectrochemistry of iron (III) oxide," *Journal of the Chemical Society, Faraday Transactions 1: Physical Chemistry in Condensed Phases*, vol. 79, no. 9, pp. 2027–2041, 1983. [Online]. Available: http://dx.doi.org/10.1039/F19837902027

[13] R. K. Quinn, R. Nasby, and R. Baughman, "Photoassisted electrolysis of water using single crystal α-Fe_2O_3 anodes," *Materials Research Bulletin*, vol. 11, no. 8, pp. 1011–1017, 1976. [Online]. Available: http://dx.doi.org/10.1016/0025-5408(76)90178-1

[14] K. Itoh and J. O. Bockris, "Stacked thin-film photoelectrode using iron oxide," *Journal of Applied Physics*, vol. 56, no. 3, pp. 874–876, 1984. [Online]. Available: http://dx.doi.org/10.1063/1.334028

[15] J. H. Kennedy and K. W. Frese, "Photooxidation of water at α-Fe_2O_3 electrodes," *Journal of the Electrochemical Society*, vol. 125, no. 5, pp. 709–714, 1978. [Online]. Available: http://dx.doi.org/10.1149/1.2131532

[16] X. Wen, S. Wang, Y. Ding, Z. L. Wang, and S. Yang, "Controlled growth of large-area, uniform, vertically aligned arrays of α-Fe_2O_3 nanobelts and nanowires," *The Journal of Physical Chemistry B*, vol. 109, no. 1, pp. 215–220, 2005. [Online]. Available: http://dx.doi.org/10.1021/jp0461448

[17] A. Kay, I. Cesar, and M. Grätzel, "New benchmark for water photooxidation by nanostructured α-Fe_2O_3 films," *Journal of the American Chemical Society*, vol. 128, no. 49, pp. 15 714–15 721, 2006. [Online]. Available: http://dx.doi.org/10.1021/ja0643801

[18] K. Sivula, R. Zboril, F. Le Formal, R. Robert, A. Weidenkaff, J. Tucek, J. Frydrych, and M. Grätzel, "Photoelectrochemical water splitting with mesoporous hematite prepared by a solution-based colloidal approach," *Journal of the American Chemical Society*, vol. 132, no. 21, pp. 7436–7444, 2010. [Online]. Available: http://dx.doi.org/10.1021/ja101564f

[19] Y. Lin, S. Zhou, S. W. Sheehan, and D. Wang, "Nanonet-based hematite heteronanostructures for efficient solar water splitting," *Journal of the American Chemical Society*, vol. 133, no. 8, pp. 2398–2401, 2011. [Online]. Available: http://dx.doi.org/10.1021/ja110741z

[20] K. Sivula, F. L. Formal, and M. Grätzel, "$WO_3-Fe_2O_3$ photoanodes for water splitting: A host scaffold, guest absorber approach," *Chemistry of Materials*, vol. 21, no. 13, pp. 2862–2867, 2009. [Online]. Available: http://dx.doi.org/10.1021/cm900565a

[21] M. Stefik, M. Cornuz, N. Mathews, T. Hisatomi, S. Mhaisalkar, and M. Grätzel, "Transparent, conducting Nb:SnO_2 for host–guest photoelectrochemistry," *Nano Letters*, vol. 12, no. 10, pp. 5431–5435, 2012. [Online]. Available: http://dx.doi.org/10.1021/nl303101n

[22] S. C. Riha, M. J. DeVries Vermeer, M. J. Pellin, J. T. Hupp, and A. B. Martinson, "Hematite-based photo-oxidation of water using transparent distributed current collectors," *ACS Applied Materials & Interfaces*, vol. 5, no. 2, pp. 360–367, 2013. [Online]. Available: http://dx.doi.org/10.1021/am302356k

[23] R. van de Krol, Y. Liang, and J. Schoonman, "Solar hydrogen production with nanostructured metal oxides," *Journal of Materials Chemistry*, vol. 18, no. 20, pp. 2311–2320, 2008. [Online]. Available: http://dx.doi.org/10.1039/B718969A

[24] D. K. Zhong and D. R. Gamelin, "Photoelectrochemical water oxidation by cobalt catalyst ("Co-Pi")/α-Fe_2O_3 composite photoanodes: oxygen evolution and resolution of a kinetic bottleneck," *Journal of the American Chemical Society*, vol. 132, no. 12, pp. 4202–4207, 2010. [Online]. Available: http://dx.doi.org/10.1021/ja908730h

[25] M. Barroso, A. J. Cowan, S. R. Pendlebury, M. Grätzel, D. R. Klug, and J. R. Durrant, "The role of cobalt phosphate in enhancing the photocatalytic activity of α-Fe_2O_3 toward water oxidation," *Journal of the American Chemical Society*, vol. 133, no. 38, pp. 14 868–14 871, 2011. [Online]. Available: http://dx.doi.org/10.1021/ja205325v

[26] J. Y. Kim, G. Magesh, D. H. Youn, J.-W. Jang, J. Kubota, K. Domen, and J. S. Lee, "Single-crystalline, wormlike hematite photoanodes for efficient solar water splitting," *Scientific Reports*, vol. 3, p. 2681, 2013. [Online]. Available: http://dx.doi.org/10.1038/srep02681

[27] S. C. Riha, B. M. Klahr, E. C. Tyo, S. Seifert, S. Vajda, M. J. Pellin, T. W. Hamann, and A. B. Martinson, "Atomic layer deposition of a submonolayer catalyst for the enhanced photoelectrochemical performance of water oxidation with hematite," *ACS Nano*, vol. 7, no. 3, pp. 2396–2405, 2013. [Online]. Available: http://dx.doi.org/10.1021/nn305639z

[28] C. Du, X. Yang, M. T. Mayer, H. Hoyt, J. Xie, G. McMahon, G. Bischoping, and D. Wang, "Hematite-based water splitting with low turn-on voltages," *Angewandte Chemie International Edition*, vol. 52, no. 48, pp. 12 692–12 695, 2013. [Online]. Available: http://dx.doi.org/10.1002/anie.201306263

[29] K. M. Young and T. W. Hamann, "Enhanced photocatalytic water oxidation efficiency with $Ni(OH)_2$ catalysts deposited on α-Fe_2O_3 via ald," *Chemical Communications*, vol. 50, no. 63, pp. 8727–8730, 2014. [Online]. Available: http://dx.doi.org/10.1039/C4CC02598A

[30] F. Lin and S. W. Boettcher, "Adaptive semiconductor/electrocatalyst junctions in water-splitting photoanodes," *Nature Materials*, vol. 13, no. 1, pp. 81–86, 2014. [Online]. Available: http://dx.doi.org/10.1038/nmat3811

[31] J. A. Glasscock, P. R. Barnes, I. C. Plumb, and N. Savvides, "Enhancement of photoelectrochemical hydrogen production from hematite thin films by the introduction of Ti and Si," *The Journal of Physical Chemistry C*, vol. 111, no. 44, pp. 16 477–16 488, 2007. [Online]. Available: http://dx.doi.org/10.1021/jp074556l

[32] T. Arai, Y. Konishi, Y. Iwasaki, H. Sugihara, and K. Sayama, "High-throughput screening using porous photoelectrode for the development of visible-light-responsive semiconductors," *Journal of Combinatorial Chemistry*, vol. 9, no. 4, pp. 574–581, 2007. [Online]. Available: http://dx.doi.org/10.1021/cc0700142

[33] R. Shinar and J. H. Kennedy, "Photoactivity of doped α-Fe_2O_3 electrodes," *Solar Energy Materials*, vol. 6, no. 3, pp. 323–335, 1982. [Online]. Available: http://dx.doi.org/10.1016/0165-1633(82)90038-7

[34] J. Turner, M. Hendewerk, J. Parmeter, D. Neiman, and G. Somorjai, "The characterization of doped iron oxide electrodes for the photodissociation of water stability, optical, and electronic properties," *Journal of the Electrochemical Society*, vol. 131, no. 8, pp. 1777–1783, 1984. [Online]. Available: http://dx.doi.org/10.1149/1.2115959

[35] V. Aroutiounian, V. Arakelyan, G. Shahnazaryan, G. Stepanyan, E. Khachaturyan, H. Wang, and J. A. Turner, "Photoelectrochemistry of semiconductor electrodes made of solid solutions in the system Fe_2O_3–Nb_2O_5," *Solar Energy*, vol. 80, no. 9, pp. 1098–1111, 2006. [Online]. Available: http://dx.doi.org/10.1016/j.solener.2005.10.005

[36] B. Zhao, T. Kaspar, T. Droubay, J. McCloy, M. Bowden, V. Shutthanandan, S. Heald, and S. Chambers, "Electrical transport properties of Ti-doped Fe_2O_3 (0001) epitaxial films," *Physical Review B*, vol. 84, no. 24, p. 245325, 2011. [Online]. Available: http://dx.doi.org/10.1103/PhysRevB.84.245325

[37] M. N. Huda, A. Walsh, Y. Yan, S.-H. Wei, and M. M. Al-Jassim, "Electronic, structural, and magnetic effects of 3d transition metals in hematite," *Journal of Applied Physics*, vol. 107, no. 12, p. 123712, 2010. [Online]. Available: http://dx.doi.org/10.1063/1.3432736

[38] O. Zandi, B. M. Klahr, and T. W. Hamann, "Highly photoactive Ti-doped α-Fe_2O_3 thin film electrodes: resurrection of the dead layer," *Energy & Environmental Science*, vol. 6, no. 2, pp. 634–642, 2013. [Online]. Available: http://dx.doi.org/10.1039/C2EE23620F

[39] O. Zandi and T. W. Hamann, "Enhanced water splitting efficiency through selective surface state removal," *The Journal of Physical Chemistry Letters*, vol. 5, no. 9, pp. 1522–1526, 2014. [Online]. Available: http://dx.doi.org/10.1021/jz500535a

[40] O. Zandi, J. A. Beardslee, and T. Hamann, "Substrate dependent water splitting with ultrathin α-Fe_2O_3 electrodes," *The Journal of Physical Chemistry C*, vol. 118, no. 30, pp. 16 494–16 503, 2014. [Online]. Available: http://dx.doi.org/10.1021/jp4116657

[41] F. Le Formal, N. Tétreault, M. Cornuz, T. Moehl, M. Grätzel, and K. Sivula, "Passivating surface states on water splitting hematite photoanodes with alumina overlayers," *Chemical Science*, vol. 2, no. 4, pp. 737–743, 2011. [Online]. Available: http://dx.doi.org/10.1039/C0SC00578A

[42] T. Hisatomi, F. Le Formal, M. Cornuz, J. Brillet, N. Tétreault, K. Sivula, and M. Grätzel, "Cathodic shift in onset potential of solar oxygen evolution on hematite by 13-group oxide overlayers," *Energy & Environmental Science*, vol. 4, no. 7, pp. 2512–2515, 2011. [Online]. Available: http://dx.doi.org/10.1039/C1EE01194D

[43] L. Steier, I. Herraiz-Cardona, S. Gimenez, F. Fabregat-Santiago, J. Bisquert, S. D. Tilley, and M. Grätzel, "Understanding the role of underlayers and overlayers in thin film hematite photoanodes," *Advanced Functional Materials*, vol. 24, no. 48, pp. 7681–7688, 2014. [Online]. Available: http://dx.doi.org/10.1002/adfm.201402742

[44] L. Xi, P. S. Bassi, S. Y. Chiam, W. F. Mak, P. D. Tran, J. Barber, J. S. C. Loo, and L. H. Wong, "Surface treatment of hematite photoanodes with zinc acetate for water oxidation," *Nanoscale*, vol. 4, no. 15, pp. 4430–4433, 2012. [Online]. Available: http://dx.doi.org/10.1039/C2NR30862B

[45] M. Barroso, C. A. Mesa, S. R. Pendlebury, A. J. Cowan, T. Hisatomi, K. Sivula, M. Grätzel, D. R. Klug, and J. R. Durrant, "Dynamics of photogenerated holes in surface modified α-Fe_2O_3 photoanodes for solar water splitting," *Proceedings of the National Academy of Sciences*, vol. 109, no. 39, pp. 15 640–15 645, 2012. [Online]. Available: http://dx.doi.org/10.1073/pnas.1118326109

[46] S. J. Moniz, S. A. Shevlin, X. An, Z.-X. Guo, and J. Tang, "Fe_2O_3–TiO_2 nanocomposites for enhanced charge separation and photocatalytic activity," *Chemistry – A European Journal*, vol. 20, no. 47, pp. 15 571–15 579, 2014. [Online]. Available: http://dx.doi.org/10.1002/chem.201403489

[47] S. J. Moniz, S. A. Shevlin, D. J. Martin, Z.-X. Guo, and J. Tang, "Visible-light driven heterojunction photocatalysts for water splitting–a critical review," *Energy & Environmental Science*, vol. 8, no. 3, pp. 731–759, 2015. [Online]. Available: http://dx.doi.org/10.1039/C4EE03271C

[48] P. Luan, M. Xie, X. Fu, Y. Qu, X. Sun, and L. Jing, "Improved photoactivity of TiO_2–Fe_2O_3 nanocomposites for visible-light water splitting after phosphate bridging and its mechanism," *Physical Chemistry Chemical Physics*, vol. 17, no. 7, pp. 5043–5050, 2015. [Online]. Available: http://dx.doi.org/10.1039/C4CP04631E

[49] M. T. Mayer, Y. Lin, G. Yuan, and D. Wang, "Forming heterojunctions at the nanoscale for improved photoelectrochemical water splitting by semiconductor materials: case studies on hematite," *Accounts of Chemical Research*, vol. 46, no. 7, pp. 1558–1566, 2013. [Online]. Available: http://dx.doi.org/10.1021/ar300302z

[50] P. Sharma, P. Kumar, A. Solanki, R. Shrivastav, S. Dass, and V. R. Satsangi, "Photoelectrochemical performance of bilayered Fe–TiO_2/Zn–Fe_2O_3 thin films for solar generation of hydrogen," *Journal of Solid State Electrochemistry*, vol. 16, no. 4, pp. 1305–1312, 2012. [Online]. Available: http://dx.doi.org/10.1007/s10008-011-1552-z

[51] W. M. Latimer, *The oxidation states of the elements and their potentials in aqueous solutions, 2nd edition.* New York: Prentice-Hall, INC., 1953.

[52] ASTM G173-03(2012), *Standard Tables for Reference Solar Spectral Irradiances: Direct Normal and Hemispherical on 37° Tilted Surface.* West Conshohocken, PA: ASTM International, 2012. [Online]. Available: http://dx.doi.org/10.1520/G0173-03R12

[53] B. G. Streetman and S. Banerjee, *Solid state electronic devices, 6th edition.* New Jersey: Pearson Prentice Hall, 2006.

[54] A. Hagfeldt and M. Graetzel, "Light-induced redox reactions in nanocrystalline systems," *Chemical Reviews*, vol. 95, no. 1, pp. 49–68, 1995. [Online]. Available: http://dx.doi.org/10.1021/cr00033a003

[55] M. Catti, G. Valerio, and R. Dovesi, "Theoretical study of electronic, magnetic, and structural properties of α-Fe_2O_3 (hematite)," *Physical Review B*, vol. 51, no. 12, p. 7441, 1995. [Online]. Available: http://dx.doi.org/10.1103/PhysRevB.51.7441

[56] W. Butler, A. Bandyopadhyay, and R. Srinivasan, "Electronic and magnetic structure of a 1000 k magnetic semiconductor: α-hematite (Ti)," *Journal of Applied Physics*, vol. 93, no. 10, pp. 7882–7884, 2003. [Online]. Available: http://dx.doi.org/10.1063/1.1556127

[57] J. Velev, A. Bandyopadhyay, W. H. Butler, and S. Sarker, "Electronic and magnetic structure of transition-metal-doped α-hematite," *Physical Review B*, vol. 71, p. 205208, May 2005. [Online]. Available: http://link.aps.org/doi/10.1103/PhysRevB.71.205208

[58] Y. Ma, P. D. Johnson, N. Wassdahl, J. Guo, P. Skytt, J. Nordgren, S. D. Kevan, J.-E. Rubensson, T. Böske, and W. Eberhardt, "Electronic structures of α-Fe_2O_3 and Fe_3O_4 from O K-edge absorption and emission spectroscopy," *Physical Review B*, vol. 48, pp. 2109–2111, 1993. [Online]. Available: http://link.aps.org/doi/10.1103/PhysRevB.48.2109

[59] A. J. E. Rettie, W. D. Chemelewski, D. Emin, and C. B. Mullins, "Unravelling small-polaron transport in metal oxide photoelectrodes," *The Journal of Physical Chemistry Letters*, vol. 7, no. 3, pp. 471–479, 2016. [Online]. Available: http://dx.doi.org/10.1021/acs.jpclett.5b02143

[60] L. M. Peter, "Dynamic aspects of semiconductor photoelectrochemistry," *Chemical Reviews*, vol. 90, no. 5, pp. 753–769, 1990. [Online]. Available: http://dx.doi.org/10.1021/cr00103a005

[61] O. Zandi and T. W. Hamann, "The potential versus current state of water splitting with hematite," *Physical Chemistry Chemical Physics*, vol. 17, no. 35, pp. 22 485–22 503, 2015. [Online]. Available: http://dx.doi.org/10.1039/C5CP04267D

[62] B. Iandolo, B. Wickman, I. Zorić, and A. Hellman, "The rise of hematite: origin and strategies to reduce the high onset potential for the oxygen evolution reaction," *Journal of Materials Chemistry A*, vol. 3, no. 33, pp. 16 896–16 912, 2015. [Online]. Available: http://dx.doi.org/10.1039/C5TA03362D

[63] R. Marcus, "Chemical and electrochemical electron-transfer theory," *Annual Review of Physical Chemistry*, vol. 15, no. 1, pp. 155–196, 1964. [Online]. Available: https://doi.org/10.1146/annurev.pc.15.100164.001103

[64] H. Gerischer, "Charge transfer processes at semiconductor-electrolyte interfaces in connection with problems of catalysis," *Surface Science*, vol. 18, no. 1, pp. 97–122, 1969. [Online]. Available: http://dx.doi.org/10.1016/0039-6028(69)90269-6

[65] C. A. Koval and J. N. Howard, "Electron transfer at semiconductor electrode-liquid electrolyte interfaces," *Chemical Reviews*, vol. 92, no. 3, pp. 411–433, 1992. [Online]. Available: http://dx.doi.org/10.1021/cr00011a004

[66] H. Gerischer, "Electrochemical behavior of semiconductors under illumination," *Journal of the Electrochemical Society*, vol. 113, no. 11, pp. 1174–1182, 1966. [Online]. Available: http://dx.doi.org/10.1149/1.2423779

[67] Y. Xu and M. A. Schoonen, "The absolute energy positions of conduction and valence bands of selected semiconducting minerals," *American Mineralogist*, vol. 85, no. 3-4, pp. 543–556, 2000. [Online]. Available: https://doi.org/10.2138/am-2000-0416

[68] R. G. W. Norrish and G. Porter, "Chemical reactions produced by very high light intensities," *Nature*, vol. 164, p. 658, 1949. [Online]. Available: http://dx.doi.org/10.1038/164658a0

[69] G. Porter, "Flash photolysis and spectroscopy. a new method for the study of free radical reactions," vol. 200, no. 1061, pp. 284–300, 1950. [Online]. Available: http://dx.doi.org/10.1098/rspa.1950.0018

[70] Nobel Media AB 2014, "The nobel prize in chemistry 1967." [Online]. Available: http://www.nobelprize.org/nobel_prizes/chemistry/laureates/1967/

[71] N. V. Tkachenko, *Optical spectroscopy: methods and instrumentations*. Elsevier, 2014.

[72] M. Dantus, M. J. Rosker, and A. H. Zewail, "Real-time femtosecond probing of "transition states" in chemical reactions," *The Journal of Chemical Physics*, vol. 87, no. 4, pp. 2395–2397, 1987. [Online]. Available: http://dx.doi.org/10.1063/1.453122

[73] M. J. Rosker, M. Dantus, and A. H. Zewail, "Femtosecond clocking of the chemical bond," *Science*, vol. 241, no. 4870, pp. 1200–1202, 1988. [Online]. Available: http://dx.doi.org/10.1126/science.241.4870.1200

[74] Nobel Media AB 2014, "The nobel prize in chemistry 1999." [Online]. Available: http://www.nobelprize.org/nobel_prizes/chemistry/laureates/1999/

[75] M. Forster, R. J. Potter, Y. Ling, Y. Yang, D. R. Klug, Y. Li, and A. J. Cowan, "Oxygen deficient α-Fe_2O_3 photoelectrodes: a balance between enhanced electrical properties and trap-mediated losses," *Chemical Science*, vol. 6, no. 7, pp. 4009–4016, 2015. [Online]. Available: http://dx.doi.org/10.1039/C5SC00423C

[76] N. J. Cherepy, D. B. Liston, J. A. Lovejoy, H. Deng, and J. Z. Zhang, "Ultrafast studies of photoexcited electron dynamics in γ- and α-Fe_2O_3 semiconductor nanoparticles," *The Journal of Physical Chemistry B*, vol. 102, no. 5, pp. 770–776, 1998. [Online]. Available: http://dx.doi.org/10.1021/jp973149e

[77] Z. Huang, Y. Lin, X. Xiang, W. Rodríguez-Córdoba, K. J. McDonald, K. S. Hagen, K.-S. Choi, B. S. Brunschwig, D. G. Musaev, C. L. Hill *et al.*, "In situ probe of photocarrier dynamics in water-splitting hematite (α-Fe_2O_3) electrodes," *Energy & Environmental Science*, vol. 5, no. 10, pp. 8923–8926, 2012. [Online]. Available: http://dx.doi.org/10.1039/C2EE22681B

[78] S. Shen, P. Guo, D. A. Wheeler, J. Jiang, S. A. Lindley, C. X. Kronawitter, J. Z. Zhang, L. Guo, and S. S. Mao, "Physical and photoelectrochemical properties of Zr-doped hematite nanorod arrays," *Nanoscale*, vol. 5, no. 20, pp. 9867–9874, 2013. [Online]. Available: http://dx.doi.org/10.1039/C3NR03245K

[79] S. R. Pendlebury, X. Wang, F. Le Formal, M. Cornuz, A. Kafizas, S. D. Tilley, M. Grätzel, and J. R. Durrant, "Ultrafast charge carrier recombination and trapping in hematite photoanodes under applied bias," *Journal of the American Chemical Society*, vol. 136, no. 28, pp. 9854–9857, 2014. [Online]. Available: http://dx.doi.org/10.1021/ja504473e

[80] S. Sorenson, E. Driscoll, S. Haghighat, and J. M. Dawlaty, "Ultrafast carrier dynamics in hematite films: The role of photoexcited electrons in the transient optical response," *The Journal of Physical Chemistry C*, vol. 118, no. 41, pp. 23 621–23 626, 2014. [Online]. Available: http://dx.doi.org/10.1021/jp508273f

[81] M. Barroso, S. R. Pendlebury, A. J. Cowan, and J. R. Durrant, "Charge carrier trapping, recombination and transfer in hematite (α-Fe_2O_3) water splitting photoanodes," *Chemical Science*, vol. 4, no. 7, pp. 2724–2734, 2013. [Online]. Available: http://dx.doi.org/10.1039/C3SC50496D

[82] B. Klahr and T. Hamann, "Water oxidation on hematite photoelectrodes: insight into the nature of surface states through in situ spectroelectrochemistry," *The Journal of Physical Chemistry C*, vol. 118, no. 19, pp. 10 393–10 399, 2014. [Online]. Available: http://dx.doi.org/10.1021/jp500543z

[83] B. Klahr, S. Gimenez, F. Fabregat-Santiago, T. Hamann, and J. Bisquert, "Water oxidation at hematite photoelectrodes: the role of surface states," *Journal of the American Chemical Society*, vol. 134, no. 9, pp. 4294–4302, 2012. [Online]. Available: http://dx.doi.org/10.1021/ja210755h

[84] B. Klahr, S. Gimenez, F. Fabregat-Santiago, J. Bisquert, and T. W. Hamann, "Electrochemical and photoelectrochemical investigation of water oxidation with hematite electrodes," *Energy & Environmental Science*, vol. 5, no. 6, pp. 7626–7636, 2012. [Online]. Available: http://dx.doi.org/10.1039/C2EE21414H

[85] O. Zandi and T. W. Hamann, "Determination of photoelectrochemical water oxidation intermediates on haematite electrode surfaces using operando infrared spectroscopy," *Nature Chemistry*, vol. 8, pp. 778–783, 2016. [Online]. Available: http://dx.doi.org/10.1038/nchem.2557

[86] H. Lehtivuori, A. Efimov, H. Lemmetyinen, and N. V. Tkachenko, "Distributed decay kinetics of charge separated state in solid film," *Chemical Physics Letters*, vol. 437, no. 4, pp. 238–242, 2007. [Online]. Available: http://dx.doi.org/10.1016/j.cplett.2007.02.029

[87] D. Monllor-Satoca, M. Bärtsch, C. Fàbrega, A. Genç, S. Reinhard, T. Andreu, J. Arbiol, M. Niederberger, and J. R. Morante, "What do you do, titanium? insight into the role of titanium oxide as a water oxidation promoter in hematite-based photoanodes," *Energy & Environmental Science*, vol. 8, no. 11, pp. 3242–3254, 2015. [Online]. Available: http://dx.doi.org/10.1039/C5EE01679G

[88] A. J. Cowan, C. J. Barnett, S. R. Pendlebury, M. Barroso, K. Sivula, M. Grätzel, J. R. Durrant, and D. R. Klug, "Activation energies for the rate-limiting step in water photooxidation by nanostructured α-Fe_2O_3 and TiO_2," *Journal of the American Chemical Society*, vol. 133, no. 26, pp. 10 134–10 140, 2011. [Online]. Available: http://dx.doi.org/10.1021/ja200800t

[89] F. Le Formal, S. R. Pendlebury, M. Cornuz, S. D. Tilley, M. Grätzel, and J. R. Durrant, "Back electron–hole recombination in hematite photoanodes for water splitting," *Journal of the American Chemical Society*, vol. 136, no. 6, pp. 2564–2574, 2014. [Online]. Available: http://dx.doi.org/10.1021/ja412058x

[90] S. R. Pendlebury, M. Barroso, A. J. Cowan, K. Sivula, J. Tang, M. Grätzel, D. Klug, and J. R. Durrant, "Dynamics of photogenerated holes in nanocrystalline α-Fe_2O_3 electrodes for water oxidation probed by transient absorption spectroscopy," *Chemical Communications*, vol. 47, no. 2, pp. 716–718, 2011. [Online]. Available: http://dx.doi.org/10.1039/C0CC03627G

Publications

Publication I

Tero-Petri Ruoko, Kimmo Kaunisto, Mario Bärtsch, Juuso Pohjola, Arto Hiltunen, Markus Niederberger, Nikolai V. Tkachenko, and Helge Lemmetyinen

"Subpicosecond to second time-scale charge carrier kinetics in hematite–titania nanocomposite photoanodes"

Journal of Physical Chemistry Letters, vol. 6, no. 15, pp. 2859–2864, 2015

Reproduced with permission from the American Chemical Society

THE JOURNAL OF PHYSICAL CHEMISTRY Letters

Letter

pubs.acs.org/JPCL

Subpicosecond to Second Time-Scale Charge Carrier Kinetics in Hematite−Titania Nanocomposite Photoanodes

Tero-Petri Ruoko,[†] Kimmo Kaunisto,*[,†] Mario Bärtsch,[‡] Juuso Pohjola,[†] Arto Hiltunen,[†] Markus Niederberger,[‡] Nikolai V. Tkachenko,[†] and Helge Lemmetyinen[†]

[†]Department of Chemistry and Bioengineering, Tampere University of Technology, P.O. Box 541, 33101 Tampere, Finland

[‡]Laboratory for Multifunctional Materials, Department of Materials, ETH Zürich, Vladimir-Prelog-Weg 5, 8093 Zürich, Switzerland

Supporting Information

ABSTRACT: Water splitting with hematite is negatively affected by poor intrinsic charge transport properties. However, they can be modified by forming heterojunctions to improve charge separation. For this purpose, charge dynamics of TiO_2:α-Fe_2O_3 nanocomposite photoanodes are studied using transient absorption spectroscopy to monitor the evolution of photogenerated charge carriers as a function of applied bias voltage. The bias affects the charge carrier dynamics, leading to trapped electrons in the submillisecond time scale and an accumulation of holes with a lifetime of 0.4 ± 0.1 s. By contrast, slower electron trapping and only few long-lived holes are observed in a bare hematite photoanode. The decay of the long-lived holes is 1 order of magnitude faster for the composite photoanodes than previously published for doped hematite, indicative of higher catalytic efficiency. These results illustrate the advantages of using composite materials to overcome poor charge carrier dynamics, leading to a 30-fold enhancement in photocurrent.

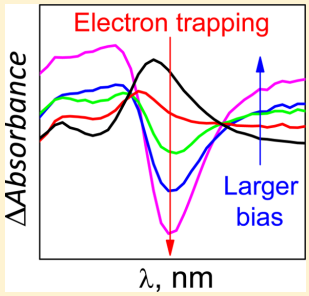

The Sun is the largest source of energy available; however, no efficient methods of storing solar power exist. Artificial photosynthesis has the potential to convert sunlight into chemical fuels that can be stored and transported over long distances, eliminating the problem of intermittent local energy production with photovoltaics. Photoelectrochemical (PEC) water reduction can be used to produce hydrogen as a renewable fuel. Ever since the discovery of PEC water splitting,[1,2] metal oxide semiconductors, such as α-Fe_2O_3 (hematite), TiO_2 (titania), and WO_3, have been preferred photoanode materials due to their abundance, nontoxicity, and thermodynamic stability.[3−8] Hematite has been especially regarded as one of the most promising photoanode materials ever since it was first used for water oxidation by Hardee and Bard.[9] Hematite has numerous desirable properties as a photoanode material: a near optimal band gap of ∼2.2 eV leading to a theoretical solar-to-hydrogen efficiency of 12.9%,[10] high chemical stability, natural abundance, and low production costs.[4,5]

However, the highest achieved solar-to-hydrogen efficiency of hematite is currently only 34% of the theoretical limit[11] due to several factors: (i) a flat band potential too low for water reduction, (ii) a high overpotential required to oxidize water, (iii) poor electron mobility, and (iv) a small hole diffusion length of 2−20 nm.[12−15] Fast charge carrier recombination due to the poor electron mobility and the small hole diffusion length can be solved by using very thin hematite films. However, the relatively low absorption coefficient of hematite leads to a long light penetration depth. Thus, thick films are needed for complete light absorption, with many electron−hole pairs formed far from the semiconductor−electrolyte interface with no opportunity to take part in the water oxidation reaction.

To overcome these intrinsic shortcomings of hematite, two separate approaches were used to increase the photocurrent efficiency. Hematite samples were prepared from amorphous iron oxide nanoparticles on fluorine-doped tin oxide (FTO) substrates to yield mesoporous films. This effectively minimizes the distance that an electron−hole pair must diffuse to reach the semiconductor−electrolyte interface to take part in the oxidation reaction. A drawback of this approach is that the mesoporous structure increases the distance that photoexcited electrons must travel to reach the conducting substrate, while the poor electron mobility remains unchanged. However, the incorporation of titanium into hematite has been shown to increase both electron mobility and concentration, while reducing the charge carrier recombination rate.[16−20] The optimal Ti concentration has been observed to range from 1 to 10 molar percent.[20] Thus, mixed hematite−titania (0−20 molar % Ti at 5% intervals) films were prepared from a nanoparticle codispersion[21] to simultaneously minimize the distance that holes must diffuse to the electrolyte interface and increase the electron mobility. According to TEM analysis (not shown) the sizes of the amorphous iron oxide and anatase nanoparticles were approximately 2−4 nm before deposition, yielding 250 ± 50 nm thick mesoporous nanocomposite

Received: May 29, 2015
Accepted: July 3, 2015
Published: July 3, 2015

DOI: 10.1021/acs.jpclett.5b01128
J. Phys. Chem. Lett. 2015, 6, 2859−2864

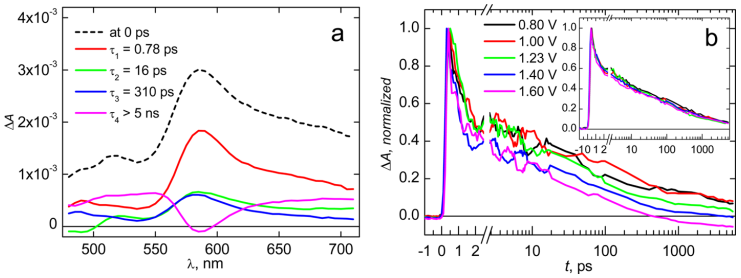

Figure 1. (a) Four-exponential decay component spectra for the hematite-titania photoanode at 1.6 V_{RHE}. (b) Normalized TAS decays at 580 nm for the bare hematite (inset) and hematite−titania (15%) photoanodes at different bias voltages vs RHE in a picoseconds−nanoseconds time scale.

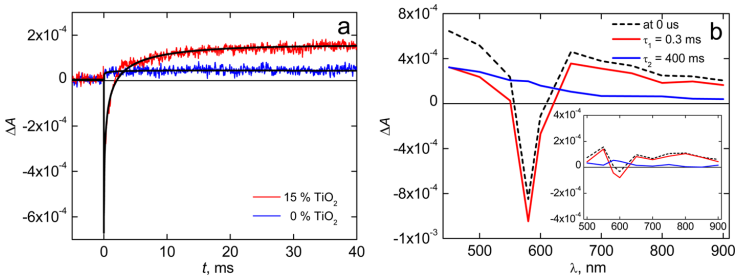

Figure 2. (a) Flash-photolysis TAS decays at 580 nm for the bare hematite and the hematite−titania (15%) samples at 1.6 V_{RHE} in a microseconds−milliseconds time scale (smoothed with a 20 point Savitzky−Golay filter). Black lines show biexponential fits to the raw data. (b) Corresponding decay component spectra for the bare hematite (inset) and hematite−titania (15%) samples at 1.6 V_{RHE}.

electrodes after annealing with an average particle diameter of approximately 40 nm regardless of the amount of incorporated titania. A scanning electron microscope (SEM) image of the mesoporous hematite structure is presented in Supporting Information Figure S1. The titania forms mainly a shell-like mixed-phase pseudobrookite−iron titanate (Fe_2TiO_5) layer on top of the larger hematite nanoparticles, as observed by a possible U-shaped titanium shell layer with X-ray photoelectron spectroscopy (XPS) and the existence of titanium mainly in the surface of hematite particles with high-resolution transmission electron microscopy (HR-TEM) combined with electron energy loss spectroscopy (EELS).[21] The solubility level of titania in hematite was determined to be between 15 and 20%, due to the formation of segregated distributions of hematite and titania with 20% incorporation of TiO_2.[21] The 15 molar % TiO_2 hematite-titania photoanode was selected as the representative nanocomposite film since it provided the highest photocurrent efficiency with respect to sample absorption (Figures S2−S4), showing a 30-fold increase in the photocurrent at 1.23 V versus the reversible hydrogen electrode (RHE).

Transient absorption spectroscopy (TAS) in a picoseconds−seconds time scale enables the investigation of the evolution of photogenerated charge carriers from initial recombination to participation in the water oxidation reaction. Studies using TAS for hematite photoanodes with applied bias voltage have been published predominantly within the past few years.[22−30] Both bare hematite and hematite−titania photoanodes feature broad time-resolved spectra at 0 ps with a maximum at 580 nm, attributed to the absorption of photogenerated electrons and holes.[22,25,30] The transient absorption peak at 580 nm is assigned to optical transitions into localized states below the conduction band level of hematite, with a positive signal indicating the oxidation of these states.[28] The four exponential decay component spectra for the hematite−titania photoanode at 1.6 V vs RHE are shown in Figure 1a. The ultrafast TAS decays at 580 nm are multiexponential with half-lives of 2.5−3.3 ps and 4.0−6.5 ps, respectively, as determined from the raw decay data shown in Figure 1b.

The application of anodic bias has little effect on the TAS dynamics of the bare hematite photoanode, with the signal decaying almost completely within 6 ns except for a small residual positive absorption at 580 nm, as visible in the inset of Figure 1b and Figure S5. This decay is assigned to a primary bimolecular electron−hole recombination with no significant electron trapping on this time scale.[30] On the other hand, the anodic bias changes the ultrafast decay dynamics of the hematite−titania photoanode significantly. The positive absorption observed at 580 nm rapidly inverts into a negative bleach signal in Figures 1 and S6, assigned to electron trapping into oxidized energy states a few hundred millivolts below the conduction band edge.[25,28,30] Furthermore, the TAS decays are significantly prolonged at wavelengths longer and shorter than the 580 nm absorption feature with applied bias, as shown in Figures S7 and S8. This is assigned to a greatly increased amount of photogenerated holes near the valence band edge due to reduced recombination.

In the microseconds−seconds time scale, the TAS decays at 580 nm for bare hematite and hematite−titania photoanodes have two distinct components: an intense negative bleach signal that inverts into a positive absorption that is observable for up to 2 s, as visible in Figures 2, S9, and S10. The decays up to 40

DOI: 10.1021/acs.jpclett.5b01128
J. Phys. Chem. Lett. 2015, 6, 2859−2864

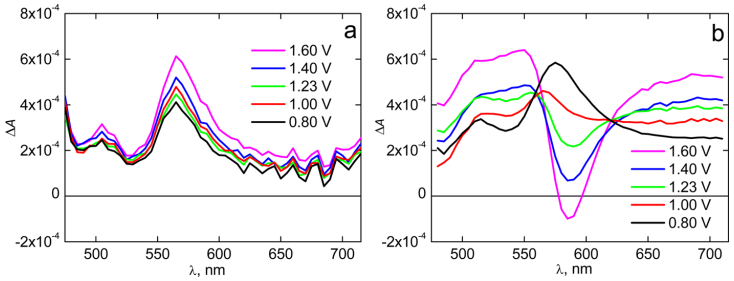

Figure 3. Longest decay component spectra (τ > 5 ns) from picoseconds to nanoseconds TAS for the (a) bare hematite and (b) hematite−titania (15% TiO_2) photoanodes at different bias voltages vs RHE.

ms at 1.6 V_{RHE} are shown in Figure 2a, and the corresponding biexponential decay component spectra are shown in Figure 2b. The faster decay component was fitted with a small energy distribution model,[31] since band bending results in a distributed exponential lifetime for the trapped electrons. In this time scale, the TAS signal amplitudes of the bare hematite film are near the instrument response limit of ~10^{-5}, as shown in Figure S11, leading to high uncertainties in the determined lifetimes and spectral features. Thus, the following discussion is limited to the hematite−titania photoanode.

The amplitude of the negative bleach signal increases with higher applied bias voltages and possesses the same spectral features observed for the longest-lived component in the nanoseconds time scale, shown in Figure 1a. This indicates a prolonged electron trapping from the nanoseconds to the milliseconds time range. The bleach signal recovers completely within 20 ms due to electron extraction from the filled energy states.[30] This is followed by a positive absorption observed throughout the probe range with lifetimes of approximately 300−400 ms at biases above the onset voltage (≥1 V), assigned to long-lived surface holes that can participate in the water oxidation reaction.[22,23,25]

The decay of the long-lived hole signal has been described as the rate-limiting step in the water oxidation reaction.[23] The water oxidation reaction rate for the long-lived holes was calculated using the kinetic model presented in ref 29, where the rate constant of the long-lived hole signal decay is equal to the sum of the rate constants for water oxidation and slow back electron recombination as described by eq 1:

$$k_{TA} = k_{WO} + k_{BER} = (\tau_{TA})^{-1} \quad (1)$$

where k_{TA} is the decay rate of the long-lived exponential transient absorption signal, k_{WO} is the water oxidation rate, k_{BER} is the rate constant for back electron recombination, and τ_{TA} is the exponential long-lived hole lifetime obtained from the two exponential global fits of raw transient absorption decays in the microseconds−seconds time scale. The water oxidation rate is presumed to be constant with respect to applied bias voltage and equal to the long-lived hole decay at the highest measured bias (1.6 V vs RHE) due to band bending preventing electron back flow.[29] Since the exponential lifetime of the long-lived hole signal is 360 ms with negligible back electron recombination at this bias voltage, the water oxidation reaction rate for the nanocomposite electrode is calculated as $k_{wo} = (\tau_{TA})^{-1} = 2.78\ s^{-1}$. The calculated rate constants and water oxidation yields for the long-lived holes at all measured bias voltages are presented in Table S1. A visual comparison of the rate constants at different bias voltages is presented in Figure S13a, whereas the water oxidation yield of long-lived holes is compared with the photocurrent density under simulated solar illumination in Figure S13b.

For the hematite−titania photoanode, the water oxidation reaction rate is 1 order of magnitude higher than the previously published results for silicon-doped hematite photoanodes ($k_{WO} \approx 2.8\ s^{-1}$ vs 0.3−0.7 s^{-1})[22,23,29] and matches the rate observed for water oxidation with titania photoanodes.[32−34] In addition, the water oxidation rate is very close to that observed for silicon-doped hematite photoanodes in the presence of methanol ($k \approx 2.7\ s^{-1}$),[22] a known hole scavenger. The high reaction rate obtained for the composite photoanode is indicative of increased catalytic activity due to a greatly decreased activation energy barrier.[23]

It is important to note that some of the observed signal for long-lived holes could originate from a direct excitation of possibly remaining anatase particles. However, due to the relatively low concentration of anatase and the unfavorable band alignment for hole transport from hematite to anatase,[21] most of the long-lived signal is suggested to originate from holes in hematite. In addition, no photocurrent specific to anatase below the onset potential of hematite is observed (Figure S4), indicating that it does not directly take part in the water oxidation reaction. The observation that the incorporation of the anatase particles mainly results in the formation of a pseudobrookite−iron titanate shell over the hematite particles in these photoanodes supports the conclusion that direct excitation of anatase can only play a very minor role in the water oxidation reaction rate.[21]

Fast electron trapping to localized oxidized states near the conduction band edge of hematite has been suggested to compete with electron−hole-pair recombination, thus increasing the hole transport efficiency.[30] The longest time scale (>5 ns) temporally resolved transient absorption spectra at different bias voltages obtained with picoseconds−nanoseconds TAS for the bare hematite and the hematite−titania photoanodes are compared in Figure 3. In this time scale, the absorption feature at 580 nm remains unchanged for the bare hematite photoanode with increased anodic bias, although a small rise in the absorbance throughout the probe region is observed. This rise is assigned to an increased surface hole concentration due to promoted band bending at the semiconductor−electrolyte interface. On the other hand, for the hematite−titania sample, the electron trapping to oxidized electron states is clearly visible at 580 nm with biases above the onset voltage. The trapping results in a greatly increased hole concentration

DOI: 10.1021/acs.jpclett.5b01128
J. Phys. Chem. Lett. 2015, 6, 2859−2864

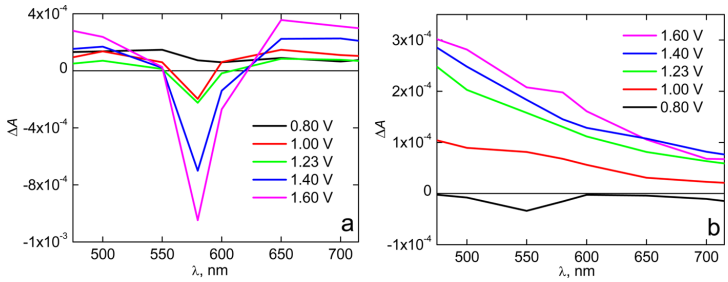

Figure 4. (a) Short- and (b) long-lived decay component spectra from microseconds to seconds TAS of the hematite−titania (15% TiO_2) sample at different bias voltages vs RHE.

observed at shorter and longer wavelengths than the bleach at 580 nm, and is attributed to increased charge separation due to the formation of the pseudobrookite−hematite heterojunction. It is possible that the incorporation of titania also leads to an increased density of energy states near the conduction band of hematite. This would result in a competitive trapping pathway for electrons, decreasing the electron−hole recombination rate, and thus increasing the charge carrier lifetime.[30]

The trapped electrons in the hematite-titania photoanodes have a lifetime in the nanoseconds to microseconds range, with the same spectral feature observed still in the millisecond time scale, as shown in Figure 4a. This is consistent with the fact that electrons trapped in oxygen vacancies in hematite cannot immediately recombine,[35] thus leading to considerably enhanced charge separation and photocurrent performance.[30] The concentration of the long-lived holes increases drastically with increased anodic voltage, as visible in Figure 4b.

After the onset potential is reached, the hole lifetime remains stable at ∼300−360 ms, as shown in Table S1 and Figure S13. This indicates a high rate for the water oxidation reaction and slow rate for the back electron recombination, with only the number of holes taking part in the reaction increasing. Only few long-lived holes are observed for the hematite−titania photoanodes at voltages below the onset potential, suggesting that the reason for high overpotentials being a prerequisite for water oxidation with hematite lies in the poor separation of holes at the semiconductor−electrolyte interface and greatly increased back electron recombination at low bias voltages. The pseudobrookite−hematite heterojunction resulting from the incorporation of titania in hematite evidently has a large effect on the charge separation process, increasing the amount of long-lived surface holes.[21] Scheme 1 illustrates the proposed mechanism with which the enhanced charge separation takes place. Since both the valence and the conduction band levels in pseudobrookite are higher than in hematite,[36] a pn-junction is created when the pseudobrookite layer forms on top of the hematite particles. This increases the charge carrier separation in the region near the junction, explaining the observed increase in the amount of long-lived holes with the nanocomposite electrode. The heterojunction also acts as a block for photogenerated electrons, retarding back electron recombination and increasing the efficiency of the photoanodes. This illustrates the importance of forming heterojunctions with nanocomposite materials, resulting in higher performances than with low level incorporation of titanium into hematite.

The results presented in this study indicate that the 30-fold increase in photocurrent performance achieved with hematite−titania composite photoanodes over bare hematite is due to two factors. First, it is shown that nanosecond time scale electron trapping into oxygen vacancies is enhanced, retarding the primary electron−hole recombination processes and hence prolonging the photogenerated hole lifetime. Second, the catalytic efficiency of the photoanodes is increased, as evidenced by room temperature kinetics for long-lived holes that are 1 order of magnitude faster than those previously published for hematite based photoanodes. The reaction kinetics observed match those published for methanol photooxidation with hematite, indicating very high catalytic performance of the photoanodes.

Scheme 1. Charge Generation, Recombination, and Transfer in the Nanocomposite Photoelectrodes[a]

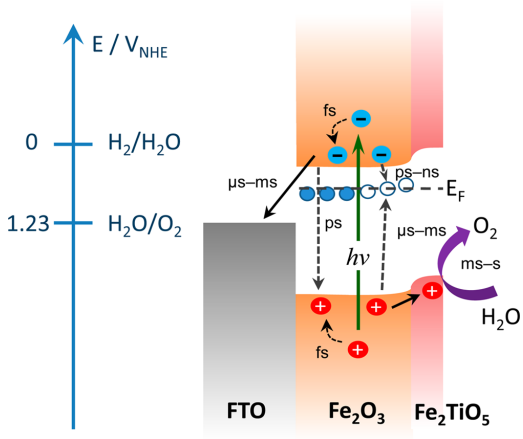

[a]Band bending and the excitation of the pseudobrookite layer are not shown in the scheme for simplicity. Valence and conduction band energies are taken from ref 36.

■ ASSOCIATED CONTENT

Ⓢ Supporting Information

Detailed experimental conditions, absorption spectra and *J*−*V* curves of samples, and decay component spectra at all measured time scales and applied bias voltages are presented in the Supporting Information. The Supporting Information is available free of charge on the ACS Publications website at DOI: 10.1021/acs.jpclett.5b01128.

DOI: 10.1021/acs.jpclett.5b01128
J. Phys. Chem. Lett. 2015, 6, 2859−2864

AUTHOR INFORMATION

Corresponding Author

*E-mail: kimmo.kaunisto@tut.fi.

Notes

The authors declare no competing financial interest.

ACKNOWLEDGMENTS

The authors kindly acknowledge the financial support under the FP7 project SOLAROGENIX, "Visible-Light Active Metal Oxide Nano-catalysts for Sustainable Solar Hydrogen Production" (NMP4-SL-2012-310333). We would also like to thank Darinka Primc, Ph.D., for performing the TEM analysis of the nanoparticles.

REFERENCES

(1) Boddy, P. J. Oxygen Evolution on Semiconducting TiO_2. *J. Electrochem. Soc.* **1968**, *115*, 199−203.

(2) Fujishima, A.; Honda, K. Electrochemical Photolysis of Water at a Semiconductor Electrode. *Nature* **1972**, *238*, 37−38.

(3) Jorand Sartoretti, C.; Alexander, B. D.; Solarska, R.; Rutkowska, W. A.; Augustynski, J.; Cerny, R. Photoelectrochemical Oxidation of Water at Transparent Ferric Oxide Film Electrodes. *J. Phys. Chem. B* **2005**, *109*, 13685−13692.

(4) Sivula, K.; Le Formal, F.; Grätzel, M. Solar Water Splitting: Progress Using Hematite (α-Fe_2O_3) Photoelectrodes. *ChemSusChem* **2011**, *4*, 432−449.

(5) Sivula, K. Metal Oxide Photoelectrodes for Solar Fuel Production, Surface Traps, and Catalysis. *J. Phys. Chem. Lett.* **2013**, *4*, 1624−1633.

(6) Nowotny, J.; Bak, T.; Nowotny, M. K.; Sheppard, L. R. Titanium Dioxide for Solar-hydrogen I. Functional Properties. *Int. J. Hydrogen Energy* **2007**, *32*, 2609−2629.

(7) Santato, C.; Odziemkowski, M.; Ulmann, M.; Augustynski, J. Crystallographically Oriented Mesoporous WO_3 Films: Synthesis, Characterization, and Applications. *J. Am. Chem. Soc.* **2001**, *123*, 10639−10649.

(8) Sayama, K.; Nomura, A.; Zou, Z.; Abe, R.; Abe, Y.; Arakawa, H. Photoelectrochemical Decomposition of Water on Nanocrystalline $BiVO_4$ Film Electrodes under Visible Light. *Chem. Commun.* **2003**, 2908−2909.

(9) Hardee, K. L.; Bard, A. J. Semiconductor Electrodes V. The Application of Chemically Vapor Deposited Iron Oxide Films to Photosensitized Electrolysis. *J. Electrochem. Soc.* **1976**, *123*, 1024−1026.

(10) Murphy, A. B. Efficiency of Solar Water Splitting using Semiconductor Electrodes. *Int. J. Hydrogen Energy* **2006**, *31*, 1999−2017.

(11) Kim, J. Y.; Magesh, G.; Youn, D. H.; Jang, J.-W.; Kubota, J.; Domen, K.; Lee, J. S. Single-Crystalline, Wormlike Hematite Photoanodes for Efficient Solar Water Splitting. *Sci. Rep.* **2013**, *3* (2681), 1−8.

(12) Dare-Edwards, M. P.; Goodenough, J. B.; Hamnett, A.; Trevellick, P. R. Electrochemistry and Photoelectrochemistry of Iron(III) Oxide. *J. Chem. Soc., Faraday Trans. 1* **1983**, *79*, 2027−2041.

(13) Quinn, R. K.; Nasby, R. D.; Baughman, R. J. Photoassisted Electrolysis of Water using Single Crystals of α-Fe_2O_3 Anode. *Mater. Res. Bull.* **1976**, *11*, 1011−1017.

(14) Itoh, K.; Bockris, J. O. Stacked Thin-Film Photoelectrode using Iron-Oxide. *J. Appl. Phys.* **1984**, *56*, 874−876.

(15) Kennedy, J. H.; Frese, K. W. Photooxidation of Water at α-Fe_2O_3 Electrodes. *J. Electrochem. Soc.* **1978**, *125*, 709−714.

(16) Wang, G.; Ling, Y.; Wheeler, D. A.; George, K. E. N.; Horsley, K.; Heske, C.; Zhang, J. Z.; Li, Y. Facile Synthesis of Highly Photoactive α-Fe_2O_3-Based Films for Water Oxidation. *Nano Lett.* **2011**, *11*, 3503−3509.

(17) Lian, X.; Yang, X.; Liu, S.; Xu, Y.; Jiang, C.; Chen, J.; Wang, R. Enhanced Photoelectrochemical Performance of Ti-doped Hematite Thin Films Prepared by the Sol−Gel Method. *Appl. Surf. Sci.* **2012**, *258*, 2307−2311.

(18) Zandi, O.; Klahr, B. M.; Hamann, T. W. Highly Photoactive Ti-doped α-Fe_2O_3 Thin Film Electrodes: Resurrection of the Dead Layer. *Energy Environ. Sci.* **2013**, *6*, 634−642.

(19) Kim, D. W.; Riha, S. C.; Demarco, E. J.; Martinson, A. B. F.; Farha, O. K.; Hupp, J. T. Greenlighting Photoelectrochemical Oxidation of Water by Iron Oxide. *ACS Nano* **2014**, *8*, 12199−12207.

(20) Kronawitter, C. X.; Zegkinoglou, I.; Shen, S.-H.; Liao, P.; Cho, I. S.; Zandi, O.; Liu, Y.-S.; Lashgari, K.; Westin, G.; Guo, J.-H.; et al. Titanium Incorporation into Hematite Photoelectrodes: Theoretical Considerations and Experimental Observations. *Energy Environ. Sci.* **2014**, *7*, 3100−3121.

(21) Monllor-Satoca, D.; Bärtsch, M.; Fàbrega, C.; Genç, A.; Hilaire, S.; Andreu, T.; Arbiol, J.; Niederberger, M.; Morante, J. R. What Do you Do, Titanium? Insight into the Role of Titanium Oxide as Water Oxidation Promoter in Hematite-Based Photoanodes. Unpublished results.

(22) Pendlebury, S. R.; Barroso, M.; Cowan, A. J.; Sivula, K.; Tang, J.; Grätzel, M.; Klug, D. R.; Durrant, J. R. Dynamics of Photogenerated Holes in Nanocrystalline α-Fe_2O_3 Electrodes for Water Oxidation Probed by Transient Absorption Spectroscopy. *Chem. Commun.* **2011**, *47*, 716−718.

(23) Cowan, A. J.; Barnett, C. J.; Pendlebury, S. R.; Barroso, M.; Sivula, K.; Grätzel, M.; Durrant, J. R.; Klug, D. R. Activation Energies for the Rate-Limiting Step in Water Photooxidation by Nanostructured α-Fe_2O_3 and TiO_2. *J. Am. Chem. Soc.* **2011**, *133*, 10134−10140.

(24) Barroso, M.; Cowan, A. J.; Pendlebury, S. R.; Grätzel, M.; Klug, D. R.; Durrant, J. R. The Role of Cobalt Phosphate in Enhancing the Photocatalytic Activity of α-Fe_2O_3 toward Water Oxidation. *J. Am. Chem. Soc.* **2011**, *133*, 14868−14871.

(25) Barroso, M.; Mesa, C. A.; Pendlebury, S. R.; Cowan, A. J.; Hisatomi, T.; Sivula, K.; Grätzel, M.; Klug, D. R.; Durrant, J. R. Dynamics of Photogenerated Holes in Surface Modified α-Fe_2O_3 Photoanodes for Solar Water Splitting. *Proc. Natl. Acad. Sci. U. S. A.* **2012**, *109*, 15640−15645.

(26) Pendlebury, S. R.; Cowan, A. J.; Barroso, M.; Sivula, K.; Ye, J.; Grätzel, M.; Klug, D. R.; Tang, J.; Durrant, J. R. Correlating Long-lived Photogenerated Hole Populations with Photocurrent Densities in Hematite Water Oxidation Photoanodes. *Energy Environ. Sci.* **2012**, *5*, 6304−6312.

(27) Cowan, A. J.; Durrant, J. R. Long-lived Charge Separated States in Nanostructured Semiconductor Photoelectrodes for the Production of Solar Fuels. *Chem. Soc. Rev.* **2013**, *42*, 2281−2293.

(28) Barroso, M.; Pendlebury, S. R.; Cowan, A. J.; Durrant, J. R. Charge Carrier Trapping, Recombination and Transfer in Hematite (α-Fe_2O_3) Water Splitting Photoanodes. *Chem. Sci.* **2013**, *4*, 2724−2734.

(29) Le Formal, F.; Pendlebury, S. R.; Cornuz, M.; Tilley, S. D.; Grätzel, M.; Durrant, J. R. Back Electron-Hole Recombination in Hematite Photoanodes for Water Splitting. *J. Am. Chem. Soc.* **2014**, *136*, 2564−2574.

(30) Pendlebury, S. R.; Wang, X.; Le Formal, F.; Cornuz, M.; Kafizas, A.; Tilley, S. D.; Grätzel, M.; Durrant, J. R. Ultrafast Charge Carrier Recombination and Trapping in Hematite Photoanodes under Applied Bias. *J. Am. Chem. Soc.* **2014**, *136*, 9854−9857.

(31) Lehtivuori, H.; Efimov, A.; Lemmetyinen, H.; Tkachenko, N. V. Distributed Decay Kinetics of Charge Separated State in Solid Film. *Chem. Phys. Lett.* **2007**, *437*, 238−242.

(32) Tang, J.; Durrant, J. R.; Klug, D. R. Mechanism of Photocatalytic Water Splitting in TiO2. Reaction of Water with Photoholes, Importance of Charge Carrier Dynamics, and Evidence for Four-Hole Chemistry. *J. Am. Chem. Soc.* **2008**, *130*, 13885−13891.

(33) Cowan, A. J.; Tang, J.; Leng, W.; Durrant, J. R.; Klug, D. R. Water Splitting by Nanocrystalline TiO_2 in a Complete Photoelectrochemical Cell Exhibits Efficiencies Limited by Charge Recombination. *J. Phys. Chem. C* **2010**, *114*, 4208−4214.

DOI: 10.1021/acs.jpclett.5b01128
J. Phys. Chem. Lett. 2015, 6, 2859−2864

(34) Tang, J.; Cowan, A. J.; Durrant, J. R.; Klug, D. R. Mechanism of O_2 Production from Water Splitting: Nature of Charge Carriers in Nitrogen Doped Nanocrystalline TiO_2 Films and Factors Limiting O_2 Production. *J. Phys. Chem. C* **2011**, *115*, 3143−3150.
(35) Rivera, R.; González, S.; Stashans, A. Microstructure and Optical Properties of α-Fe_2O_3 Containing F-centres. *Superlattices Microstruct.* **2010**, *47*, 225−231.
(36) Courtin, E.; Baldinozzi, G.; Sougrati, M. T.; Stievano, L.; Sanchez, C.; Laberty-Robert, C. New Fe_2TiO_5-Based Nanoheterostructured Mesoporous Photoanodes with Improved Visible Light Photoresponses. *J. Mater. Chem. A* **2014**, *2*, 6567−6577.

DOI: 10.1021/acs.jpclett.5b01128
J. Phys. Chem. Lett. 2015, 6, 2859−2864

Publication II

Davide Barreca, Giorgio Carraro, Alberto Gasparotto, Chiara Maccato, Michael E. A. Warwick, Kimmo Kaunisto, Cinzia Sada, Stuart Turner, Yakup Gönüllü, Tero-Petri Ruoko, Laura Borgese, Elza Bontempi, Gustaaf Van Tendeloo, Helge Lemmetyinen, and Sanjay Mathur

"Fe_2O_3 – TiO_2 nano-heterostructure photoanodes for highly efficient solar water oxidation"

Advanced Materials Interfaces, vol. 2, no. 17, p. 1500313, 2015

Fe_2O_3–TiO_2 Nano-heterostructure Photoanodes for Highly Efficient Solar Water Oxidation

Davide Barreca, Giorgio Carraro, Alberto Gasparotto, Chiara Maccato, Michael E. A. Warwick, Kimmo Kaunisto,* Cinzia Sada, Stuart Turner, Yakup Gönüllü, Tero-Petri Ruoko, Laura Borgese, Elza Bontempi, Gustaaf Van Tendeloo, Helge Lemmetyinen, and Sanjay Mathur*

Harnessing solar energy for the production of clean hydrogen by photoelectrochemical water splitting represents a very attractive, but challenging approach for sustainable energy generation. In this regard, the fabrication of Fe_2O_3–TiO_2 photoanodes is reported, showing attractive performances [≈2.0 mA cm^{-2} at 1.23 V vs. the reversible hydrogen electrode in 1 M NaOH] under simulated one-sun illumination. This goal, corresponding to a tenfold photoactivity enhancement with respect to bare Fe_2O_3, is achieved by atomic layer deposition of TiO_2 over hematite (α-Fe_2O_3) nanostructures fabricated by plasma enhanced-chemical vapor deposition and final annealing at 650 °C. The adopted approach enables an intimate Fe_2O_3–TiO_2 coupling, resulting in an electronic interplay at the Fe_2O_3/TiO_2 interface. The reasons for the photocurrent enhancement determined by TiO_2 overlayers with increasing thickness are unraveled by a detailed chemico-physical investigation, as well as by the study of photogenerated charge carrier dynamics. Transient absorption spectroscopy shows that the increased photoelectrochemical response of heterostructured photoanodes compared to bare hematite is due to an enhanced separation of photogenerated charge carriers and more favorable hole dynamics for water oxidation. The stable responses obtained even in simulated seawater provides a feasible route in view of the eventual large-scale generation of renewable energy.

1. Introduction

The development of sustainable energy production systems has become an ever-growing demand under the rising stress of the global population, living standards, and increased industrialization.[1–7] In this context, photoactivated methods such as photoelectrochemical (PEC) H_2O splitting, starting from two abundant natural resources such as solar photons and water, are environmentally benign approaches for the production of hydrogen as a clean and renewable energy vector.[8–24] A key issue for PEC water splitting is the identification of suitable photoanode materials satisfying the challenging requirements for solar hydrogen generation.[13,14,25,26] Among the most promising candidates, hematite (α-Fe_2O_3) has long been a preferred choice[18,20,27–32] thanks to its good photochemical stability, earth abundance, nontoxicity, low cost and proper band gap ($E_G \approx 2.1$ eV) to absorb a large fraction of the solar spectrum.[3,4,16,21,33–36] In spite of these advantages, the solar-to-hydrogen

Dr. D. Barreca
CNR-IENI and INSTM
Department of Chemistry
Padova University
35131 Padova, Italy
E-mail: davide.barreca@unipd.it
Dr. G. Carraro, Dr. A. Gasparotto, Prof. C. Maccato,
Dr. M. E. A. Warwick
Department of Chemistry
Padova University and INSTM
35131 Padova, Italy
Dr. K. Kaunisto, T.-P. Ruoko, Prof. H. Lemmetyinen
Department of Chemistry and Bioengineering
Tampere University of Technology
33101 Tampere, Finland
E-mail: kimmo.kaunisto@tut.fi

DOI: 10.1002/admi.201500313

Prof. C. Sada
Department of Physics and Astronomy
Padova University
35131 Padova, Italy
Dr. S. Turner, Prof. G. Van Tendeloo
EMAT
University of Antwerp
2020 Antwerpen, Belgium
Dr. Y. Gönüllü, Prof. S. Mathur
Department of Chemistry
Chair of Inorganic and Materials Chemistry
Cologne University
50939 Cologne, Germany
Dr. L. Borgese, Prof. E. Bontempi
Chemistry for Technologies Laboratory
University of Brescia
25123 Brescia, Italy

efficiency of hematite falls well short of the theoretical maximum value (≈13%)[6,7,10,11,34,37] due to a number of factors,[2,12,17,25,30,38] including poor charge transport properties, improper band positions for unassisted water splitting, low electron–hole pair lifetime (<10 ps), and small exciton diffusion length (≈2–4 nm).[11,28,35,39,40] To overcome these drawbacks and enhance hematite conductivity and photoresponses, the most commonly used strategies are nanoarchitecture engineering[7,11,18,22,26,39] and elemental doping.[17,25,29,41,42] Other improvements have been afforded by the introduction of oxygen evolution catalysts (OECs), such as Co-, Ni-, Ir-, and Ru-based ones.[1,10,19,24–26,43] Despite the advantageous reduction in the onset potential, most of these systems are toxic and/or expensive, being unsuitable for large-scale energy production. In addition, water oxidation efficiencies are often limited by surface recombination, a severe issue to be tackled.[19,26,44] An alternative strategy to address the primary requirements for an efficient solar-to-hydrogen conversion consists in the formation of nano-heterostructures involving Fe_2O_3 coupling with suitable underlayers or overlayers[1,4,33,40,45,46] to suppress electron back recombination at the hematite/substrate interface,[20,28,29] enhance light absorption, and improve charge carrier transport properties.[5,16,19,27,47] So far, several works have been focused on the surface functionalization of Fe_2O_3 nanosystems with various oxides, such as Al_2O_3, Ga_2O_3, $Fe_xSn_{1-x}O_4$, and TiO_2.[3,10,19,20,39] The obtained results highlight the possibility of improving PEC performances by passivation of surface states, protection against corrosion, use of buried semiconductor junctions,[2,19] and a proper tailoring of charge transfer processes between the constituent phases.[20,47] Nevertheless, the practical use of modified hematite photoanodes in efficient, durable, and low-cost solar hydrogen production is still hindered by various factors,[37] including the system stability[29] and the difficulties in identifying precise structure–functions relationships.[6,17] In addition, driving PEC water splitting more efficiently than the state-of-the-art hematite photoanodes[48] remains a main hurdle impeding further technological developments.[34]

In the present study, we report on a method for the enhancement of hematite photoanode charge transfer, resulting in a remarkable improvement of the recorded PEC performances in solar water splitting. In particular, we have devoted our attention to the coating of plasma enhanced-chemical vapor deposition (PE-CVD) hematite nanostructures by an atomic layer deposition (ALD) TiO_2 overlayer, followed by thermal treatment in air at 650 °C. It is worth highlighting that, despite several efforts aimed at investigating Ti incorporation into hematite photoelectrodes,[7,29,35,38,40,42] Fe_2O_3–TiO_2 multilayered and composite systems have so far been much less investigated.[3,6,16,27,45] For these materials, the current density for water photooxidation has been reported to drop off with an increased number of TiO_2 ALD cycles, the reasons underlying this behavior being unclear.[2] In this work, taking advantage of ALD repeatability, conformity, and precise thickness control,[24,46,49] we focus our attention on the PEC behavior of Fe_2O_3–TiO_2 nano-heterostructures characterized by different TiO_2 overlayer thicknesses. A relevant attention is devoted to the interrelations between system properties and functional performances, with particular regard to the structural and electronic interplay occurring at Fe_2O_3/TiO_2 heterointerfaces. Under optimized conditions, a tenfold photocurrent increase compared to bare α-Fe_2O_3 photoanodes was observed, corresponding to the highest performances ever reported for similar systems, especially at high applied potentials. This feature, along with the high stability even in simulated seawater, for which solar splitting has only been seldom investigated,[50] represents an important goal toward the sustainable and efficient conversion of solar light into chemical energy.

2. Results and Discussion

2.1. Preparation and Characterization of Fe_2O_3–TiO_2 Photoanodes

Fe_2O_3–TiO_2 photoanodes were fabricated by a three-step protocol, involving: (i) PE-CVD of Fe_2O_3 on fluorine-doped tin oxide (FTO) substrates; (ii) ALD of TiO_2 with a different cycle number, in order to tailor the corresponding overlayer thickness; and (iii) annealing in air for 1 h at 650 °C (**Table 1**). Bare Fe_2O_3 (hereafter labeled as Fe_2O_3), composed of pure α-Fe_2O_3 (hematite) free from other iron oxide polymorphs, was characterized by an inherently porous nanoorganization [Figure S1, Supporting Information]. The subsequent ALD of TiO_2 resulted in morphological variations, as revealed by field emission-scanning electron microscopy (FE-SEM; see **Figure 1**). In particular, specimens 400_L and 400_H, obtained with a lower and a higher number of ALD cycles, presented more rounded surface features than the pristine Fe_2O_3 (Figure S1a,b, Supporting Information). In the case of 400_L, functionalization with TiO_2 produced only a modest alteration of Fe_2O_3 aggregate features, indicating the formation of a conformal thin film. For specimen 400_H, more marked modifications of the surface morphology took place (Figure 1a,b). The system double-layered structure was clearly evidenced by cross-sectional FE-SEM images (Figure 1c,d). As can be observed, upon going from specimen 400_L to the homologous 400_H, the TiO_2 overlayer thickness underwent a parallel increase. These observations, along with the intimate and uniform Fe_2O_3–TiO_2 contact, highlight the intrinsic ALD conformal coverage capability,[18,19,49] enabling a fine control of the resulting Fe_2O_3–TiO_2 heterojunction features. Cross sectional FE-SEM images enabled the estimation of the total nanodeposit (and titania overlayer) thickness values, yielding 400 ± 15 (35 ± 10) and 480 ± 30 (80 ± 10) nm for 400_L and 400_H, respectively. In order to attain further insight into the system topography, the material surfaces were probed by atomic force microscopy (AFM; Figure 1g,h). The recorded micrographs showed the formation of multigrain structures, in line with FE-SEM observations. Irrespective of the synthesis conditions, very similar root-mean-square (RMS) roughness values (≈20 nm) were obtained for the analyzed systems.

Table 1. Main growth and processing conditions for FTO-supported photoanodes investigated in the present study.

Sample ID	Fe_2O_3 by PE-CVD	TiO_2 by ALD	Thermal annealing
Fe_2O_3	400 °C, 1 h	//	650 °C, 1 h, air
400_L	400 °C, 1 h	150 °C, 1150 cycles	650 °C, 1 h, air
400_H	400 °C, 1 h	150 °C, 5750 cycles	650 °C, 1 h, air

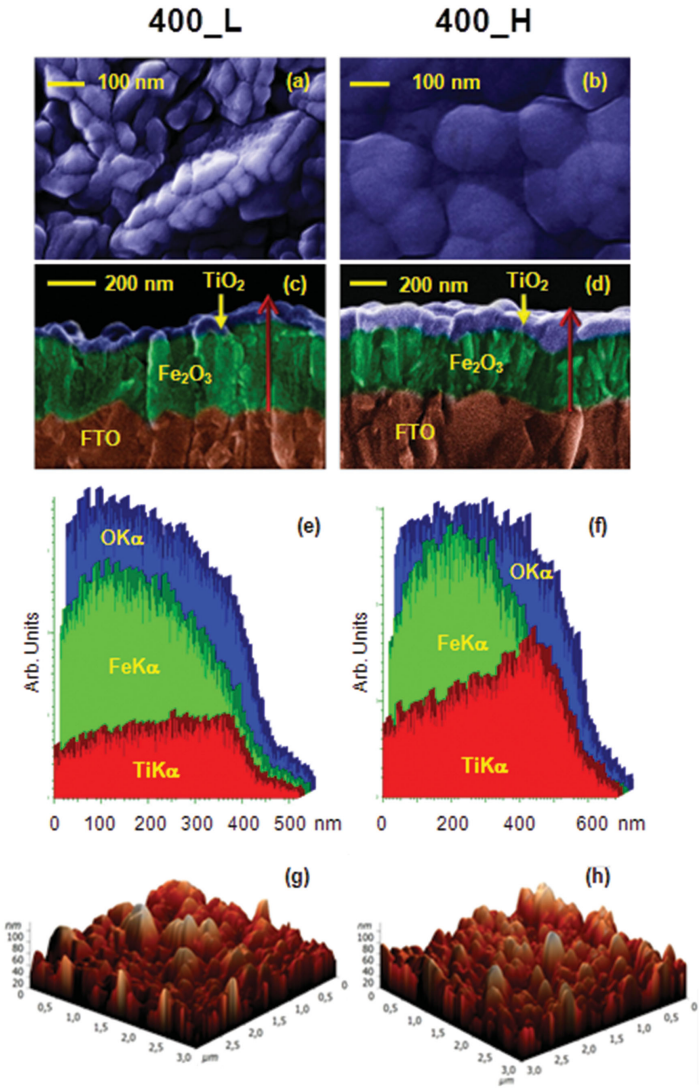

Figure 1. a,b) Plane-view FE-SEM images, c,d) cross-sectional FE-SEM images, e,f) EDXS line-scan profiles recorded along the lines marked in cross-sectional views, and g,h) AFM micrographs for Fe_2O_3–TiO_2 specimens. In (e) and (f), arrows mark the direction of abscissa increase.

The local in-depth composition was analyzed by energy dispersive X-ray spectroscopy (EDXS) line-scans (Figure 1e,f). The obtained data showed that TiO_2 was mainly concentrated in the outermost material region, a phenomenon more evident for the 400_H sample, confirming that a higher number of ALD cycles resulted in a thicker TiO_2 overlayer, as already appreciated by FE-SEM images. Conversely, the FeKα line intensity underwent a progressive increase in the inner system region at the expense of the TiKα one, confirming the predominance of Fe_2O_3 in the deposit regions closer to the FTO substrate.

Since the mutual spatial distribution of Fe_2O_3 and TiO_2 is a key issue for an optimal heterostructure engineering, the in-depth chemical composition along the thickness was further investigated by secondary ion mass spectrometry (SIMS) analyses (**Figure 2** a,b). The obtained data allowed the estimation of a mean C concentration (averaged over the whole thickness) as low as 150 ppm, highlighting thus the purity of the obtained materials. Irrespective of the processing conditions, the O ionic yield remained almost constant throughout the investigated depth. As can be observed in Figure 2, the outermost sample region was Ti-rich, a phenomenon particularly evident for specimen 400_H, characterized by a higher thickness of the TiO_2 overlayer. Upon increasing the sputtering time, a concomitant increase in the Fe ionic yield and a progressive decrease in the Ti one took place, in agreement with EDXS data (see Figure 1). This evidence suggested that the TiO_2 layer was covering hematite nanostructures even in the inner regions, a phenomenon due to the synergy between the Fe_2O_3 porosity and the good conformality achievable by the use of ALD. Finally, both titanium and iron signals underwent a net intensity decrease at the interface with the FTO substrate. The Sn tailing extending into the nanodeposits at the interfacial region suggested the occurrence of tin diffusion from the FTO substrate induced by thermal annealing, at least to some extent. This phenomenon, already observed in previous works, might beneficially contribute to PEC performances, due to an improved system electrical conductivity.[37,43,51]

Overall, the data discussed so far point to the obtainment of Fe_2O_3–TiO_2 heterostructures, with titanium oxide being mainly confined in the outermost system regions. To perform a detailed characterization of the Fe and Ti chemical environments, X-ray photoelectron spectroscopy (XPS) analyses were carried out. Wide-scan XPS spectra (Figure S2a, Supporting Information) were dominated by titanium and oxygen photopeaks. In the case of sample 400_L, the presence of iron could also be detected (see Figure 2d), suggesting in this case the occurrence of a thinner and porous TiO_2 overlayer (compare TEM analysis; see below). Irrespective of the used ALD conditions, the $Ti2p_{3/2}$ binding energy (BE) of 458.5 eV, as well as the separation between the spin-orbit components [Δ(BE) = 5.7 eV] (Figure 2c), was in line with the presence of Ti(IV) in TiO_2.[35,52] The Fe2p peak shape and position [Figure 2d; BE($Fe2p_{3/2}$) = 711.1 eV], along with the pertaining spin-orbit splitting [Δ(BE) = 13.7 eV], were consistent with the formation of iron(III) oxide free from other Fe oxidation states.[7,11,33,35,42,52] The O1s

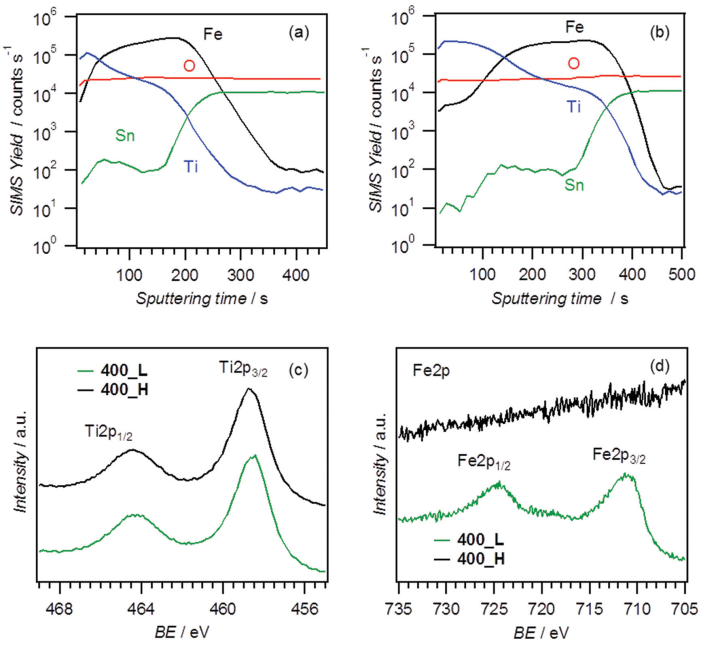

Figure 2. SIMS depth profiles for Fe_2O_3–TiO_2 deposits on FTO: a) 400_L and b) 400_H. c) Ti2p and d) Fe2p XPS surface spectra for the same specimens.

signal (Figure S2b, Supporting Information) could be fitted by two contributing bands located at (I) BE = 530.0 eV and (II) 532.0 eV, attributed to lattice O and surface –OH groups/adsorbed oxygen.[4,7,35,42]

The structure of the deposited Fe_2O_3–TiO_2 photoanodes was investigated by X-ray diffraction (XRD). The recorded patterns (Figure S3, Supporting Information) were dominated by a series of signals corresponding to hematite reflections for both specimens 400_L and 400_H.[53] Interestingly, the latter also showed the appearance of additional peaks at 2θ = 25.3° and 47.9°, related to (101) and (200) crystallographic planes of anatase TiO_2,[54] whereas no signals related to titania could be unambiguously observed for sample 400_L, due to the lower amount of deposited TiO_2 (compare the thickness values obtained by cross-sectional FE-SEM analyses, see above). In accordance with XPS results, no reflections related to Fe–Ti–O ternary phases were present, and the absence of appreciable angular shifts also enabled to rule out the occurrence of Ti doping into Fe_2O_3.

To investigate the nanoscale structure of Fe_2O_3–TiO_2 materials, high resolution transmission electron microscopy (HR-TEM), high angle annular dark field scanning transmission electron microscopy (HAADF-STEM), and EDXS analyses were carried out. **Figure 3**a–d displays HAADF-STEM (*Z* contrast) overview images of both samples in cross-section, together with EDXS elemental maps for Ti, Fe, Sn, and Si, evidencing the glass/FTO/α-Fe_2O_3/TiO_2 multilayer stacks. The Fe_2O_3/TiO_2 interface is imaged in more detail in Figure 3e,f, from which TiO_2 overlayer thickness values were extracted and were in excellent agreement with those provided by FE-SEM analyses (see above and Figure 1). Irrespective of the used ALD conditions, the Fe_2O_3 nanodeposit consisted of well-developed upward growing hematite needles, whose assembly resulted in an open, porous structure. This peculiar texture enabled the ALD TiO_2 coating to be deposited even in the inner system regions, confirming the formation of Fe_2O_3–TiO_2 nano-heterostructures. The overlayers, composed by TiO_2 with the anatase crystal phase, are further imaged by the HR micrographs reported in Figure 3g,h. The presence of small voids (mean size of few nanometers), imaged as a dark contrast in the mass-thickness sensitive HAADF-STEM view in Figure 3h, highlights the porosity of the titania top layer. Electron diffraction (ED) maps of both specimens showed reflections that could be attributed to hematite and anatase phases (see Figure S4, Supporting Information), despite the 400_L sample displaying very weak anatase signals due to the low TiO_2 amount (see also XRD data).

The target Fe_2O_3/TiO_2 nano-heterostructures were also analyzed by optical absorption spectroscopy (Figure S5, Supporting Information). The recorded spectra were characterized by a sub-bandgap scattering tail in the 600–750 nm region and a sharp absorbance increase occurring from 550–600 nm toward lower wavelengths, consistent with the bandgap of hematite.[25,40,43] As a whole, the optical properties of the present Fe_2O_3–TiO_2 heterostructures are appealing for PEC water splitting triggered by solar irradiation, since these photoanodes can efficiently absorb a significant fraction of the Vis spectrum. From Tauc plots, it was possible to extrapolate a mean band gap (E_G) value of 2.1 eV, revealing that the TiO_2 overlayers did not appreciably affect the optical features in the Vis range.[16,17,38,44]

2.2. PEC Investigation of Fe_2O_3–TiO_2 Photoanodes

The functional properties of Fe_2O_3–TiO_2 heterostructures in PEC water splitting were evaluated in NaOH aqueous solutions (**Figure 4**a) and compared with those of a bare Fe_2O_3 photoelectrode. In the absence of illumination, the samples showed very small currents, and even when the water electrolysis reaction was reached at ≈1.8 V,[5] dark currents were lower than 1 mA cm^{-2}. Upon simulated solar illumination, a net *j* increase at potentials lower than E° (1.23 V vs reversible hydrogen electrode (RHE)) took place, since part of the energy required for the oxidation process is captured from the incident light.[5] Considering the onset potentieal (E_{onset}) as the value at which a current density of 0.02 mA cm^{-2} is first reached,[6] for the pure Fe_2O_3 photoanode E_{onset} was estimated to be 1.1 V_{RHE}. Subsequently, a progressive *j* increase with *E* occurred, reaching a value of 0.24 mA cm^{-2} at 1.23 V_{RHE}. As can be observed, the functionalization of hematite with TiO_2 resulted in a decrease of the onset potential and in a significant increase of the recorded

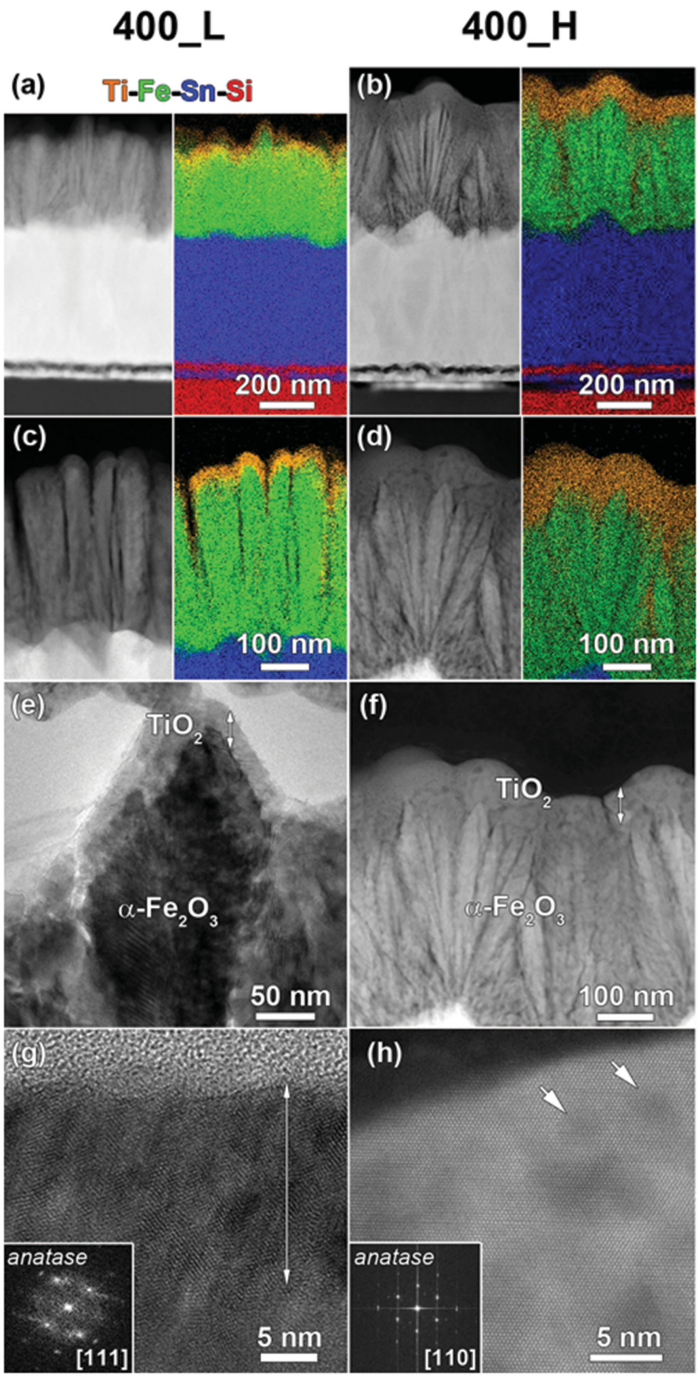

Figure 3. TEM characterization of Fe_2O_3–TiO_2 photoanodes. a–d) Cross sectional HAADF-STEM images and corresponding EDXS chemical maps of samples a,c) 400_L and b,d) 400_H. e) TEM overview image of sample 400_L. f) HAADF-STEM overview of sample 400_H. In both cases, the TiO_2 overlayer thickness is marked by a double-ended arrow. g) HR-TEM image of sample 400_L, evidencing the low crystallinity of the anatase top layer. The anatase layer is imaged along the [111] zone axis, as evidenced by the inset Fourier transform (FT) pattern. h) High resolution HAADF-STEM image of sample 400_H, with arrows indicating the presence of small dark-contrast voids in the highly crystalline anatase overlayer. The anatase layer is imaged along the [110] zone axis, as evidenced by the inset FT pattern.

photocurrent values. Interestingly, a dependence of PEC performances on TiO_2 thickness could be clearly appreciated, since sample 400_H displayed a systematic enhancement of photocurrent values with respect to the 400_L one. In particular, 400_H showed an E_{onset} value as low as 0.8 V_{RHE} and j = 2.0 mA cm^{-2} at 1.23 V_{RHE}, a value nearly ten times higher than that pertaining to pure Fe_2O_3. It is generally accepted that the required overpotential is related to the poor oxygen evolution reaction (OER) kinetics and to the unfavorable conduction band energy position for bare Fe_2O_3.[5,6,19,46] As a consequence, the shift of E_{onset} to more cathodic potentials highlights the beneficial effect exerted by TiO_2 functionalization on the system photoresponse. Along with the onset potential, one of the most important parameters to evaluate photoanode performances is represented by the photocurrent value plateau. In this regard, bare Fe_2O_3 reached a plateau at ≈1.4 V (j ≈ 0.6 mA cm^{-2}), whereas Fe_2O_3–TiO_2 systems did not display any appreciable saturation up to 1.8 V vs. RHE (j ≈ 9.6 mA cm^{-2} for specimen 400_H).

Based on the above observations, the higher photocurrents for samples 400_L and 400_H, as well as the absence of saturation effects at potentials higher than 1.23 V vs. RHE, can be traced back to the formation of Fe_2O_3–TiO_2 heterojunctions, responsible for a more efficient charge carrier separation with respect to bare Fe_2O_3.[5] In particular, at 1.23 V_{RHE}, a j value close to 2.0 mA cm^{-2} was recorded for the 400_H specimen. This photocurrent threshold compares very favorably with the best values reported in the literature for Fe_2O_3–TiO_2 photoelectrodes.[4,6,14,15,19,32,50] Such a result, obtained without the use of any expensive/toxic cocatalyst, is very attractive in view of solar water splitting promoted by Fe_2O_3–TiO_2 materials.

In order to elucidate the role of the TiO_2 overlayer, solar-to-hydrogen (STH) efficiency values were calculated from j–E data. It is worth noting that only a few works in the

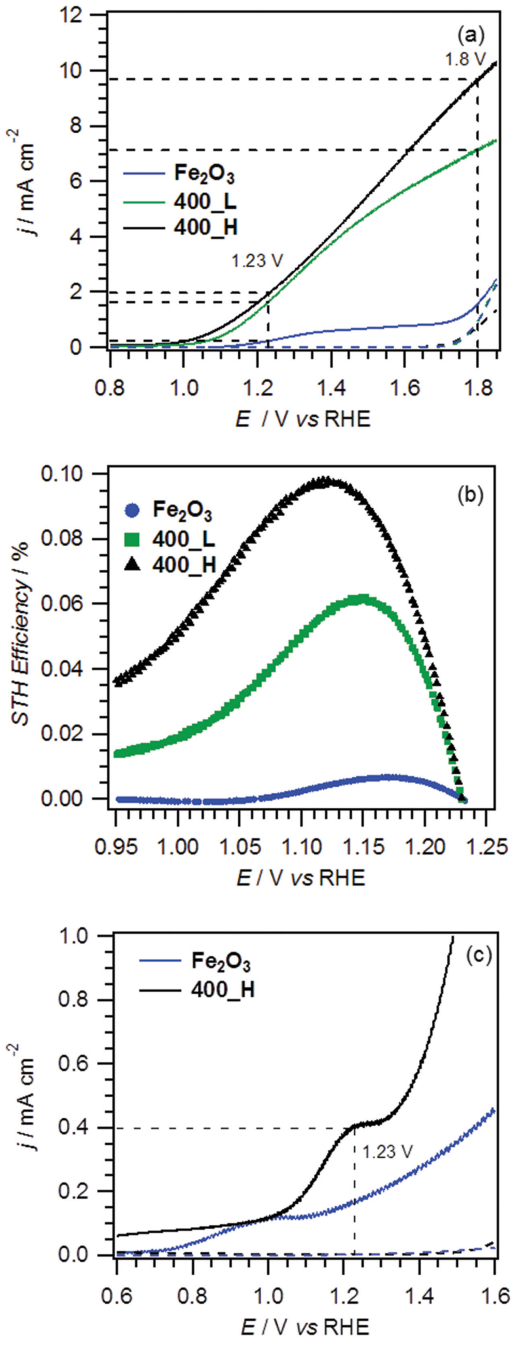

Figure 4. a) Photocurrent density vs. applied potential curves for Fe_2O_3 and Fe_2O_3–TiO_2 photoelectrodes recorded in 1 M NaOH solution under simulated solar irradiation (continuous lines) and in the dark (dashed lines). b) Calculated solar-to-hydrogen (STH) efficiencies. c) *j–E* curves for bare Fe_2O_3 and for specimen 400_H in a simulated seawater solution, recorded under solar illumination. Dark current curves are reported as dashed lines.

available literature report STH values for similar systems.[34] As can be appreciated from Figure 4b, the STH efficiency maximum increased in the order: Fe_2O_3 (0.007%) < 400_L (0.060%) < 400_H (0.098%). Notably, the highest photoefficiency values were obtained for TiO_2-containing specimens at *E* values lower than for bare Fe_2O_3. This finding highlights the importance of the Fe_2O_3-TiO_2 heterojunction on charge separation, as well as the positive effect exerted by titania functionalization in enhancing hole dynamics for water oxidation (see also below). To further demonstrate the beneficial role of the Fe_2O_3-TiO_2 heterojunction, it is worth noticing that the PEC response upon solar irradiation (SI, Figure S6) of bare TiO_2, fabricated by ALD and annealed at 650 °C, is almost negligible.

It is well known that the main drawbacks related to the use of Fe_2O_3 photoanodes include the high density of surface states, low hole mobility, short charge-carrier lifetime, and slow OER kinetics.[2,50] On the other hand, even TiO_2 photoanodes suffer from various disadvantages, in particular from poor solar light harvesting.[3,45] So far, some studies have demonstrated that functionalization of Fe_2O_3 with TiO_2 results in worse PEC performances with respect to bare iron(III) oxide.[2,19,50] In a different way, the very high photocurrents shown by the present Fe_2O_3/TiO_2 photoanodes, along with the decreased onset voltages and the absence of significant saturation at high applied potentials, highlight the benefit offered by Fe_2O_3/TiO_2 heterojunctions in affording favorable photoactivity improvements.[3,16,27,47] Due to the mutual positions of Fe_2O_3 and TiO_2 conduction band edges, electrons photogenerated in TiO_2 can be easily transferred to Fe_2O_3 and injected into the FTO substrate, and can subsequently migrate through the external electric circuit to reduce water at the cathode,[45] suppressing thus detrimental recombination effects (see also below and **Scheme 1**). An additional favorable contribution to the actual performances is related to the fact that TiO_2 overlayers can prevent hematite photocorrosion in a wide pH range.[5]

To attain an insight into the stability of the present materials, PEC measurements were carried out under the same conditions at the first and third day of utilization for the best performing system, i.e. specimen 400_H. The obtained experimental results (Figure S7, Supporting Information) revealed that the measured photocurrent values did not undergo any appreciable variation, evidencing a good stability of the target photoanodes, a key prerequisite for their technological applications.

Based on these very favorable results, the most efficient and promising photoelectrode (400_H) was tested in PEC water splitting using simulated seawater solutions. The use of seawater represents a key technological target for a real-world sustainable hydrogen generation, since 97.5% of the overall H_2O available on earth is salt water.[55,56] Figure 4c compares *j–E* curves obtained using simulated seawater upon solar illumination for specimen 400_H and for bare Fe_2O_3. As can be observed, for the latter, an increase in photocurrent densities with the applied potential was observed (≈0.2 mA cm^{-2} at 1.23 V_{RHE}). Interestingly, sample 400_H yielded a higher photocurrent density that, despite being lower than that recorded in NaOH solutions (compare Figure 4a), reached *j* values of ≈0.4 mA cm^{-2} at 1.23 V_{RHE}. This result, along with the previously discussed PEC data, shows that the obtained Fe_2O_3–TiO_2 materials represent a key step forward for the fabrication of photoanodes to be used in real-world devices.

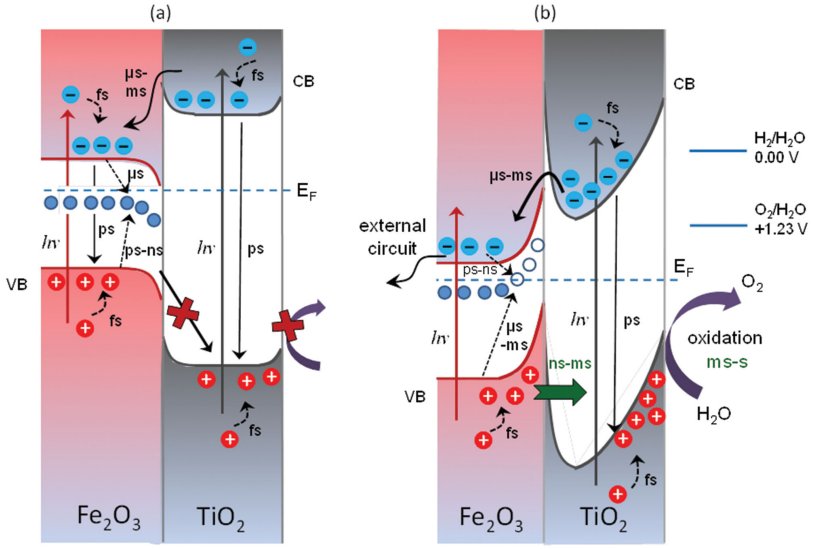

Scheme 1. Schematic energy level diagrams illustrating the photoactivated charge transfer processes and related timescales: a) without and b) with the application of a positive external bias to Fe_2O_3–TiO_2 photoanodes. The intraband electron-trap states, located a few 100 mV below the conduction band edge of hematite, are also shown (CB: conduction band, VB: valence band, E_F: Fermi level, fs: femtosecond, ps: picosecond, ns: nanosecond, μs: microsecond, ms: millisecond).

2.3. TAS Analysis on Fe_2O_3–TiO_2 Photoanodes

To further elucidate the role of Fe_2O_3/TiO_2 heterojunctions in promoting the PEC water splitting and investigate charge-carrier dynamics in the target photoelectrodes, transient absorption spectroscopy (TAS) analyses were carried out. TAS measurements allow the monitoring of photogenerated electron and hole dynamics from a picosecond to a second timescale,[57–59] and are a powerful tool for the study of the interplay between nanostructure and PEC response in Fe_2O_3 and TiO_2 based photoanodes.[25,42,57,60,61] In this work, the evolution of charge carriers was examined by using band-gap excitation of both Fe_2O_3 and TiO_2 at λ = 355 nm, simulating the solar illumination conditions in which light is absorbed by both components.

To investigate the electron mobility of TiO_2 functionalized specimens, microsecond-to-millisecond TAS decays were measured at λ = 580 nm. The selected probe wavelength corresponds to electrons trapped in hematite intra-band states and long-lived holes in both hematite and anatase.[57,58,62] Transient absorption traces and corresponding exponential fits for the specimens are displayed in **Figure 5**a. The initial photobleaching, i.e., the negative absorption change, following the excitation laser pulse could be assigned to the intra-band trapped electrons in hematite.[57] The fits resulted in lifetimes of 1.7 and 900 ms for bare Fe_2O_3, 0.5 and 550 ms for sample 400_L, and 0.3 and 330 ms for sample 400_H, respectively. The short-lived components correspond to the bleaching recovery, attributed to the extraction of trapped electrons, and are therefore indicative of electron mobility in the metal oxide structure. The increased bleaching recovery rate ($1/\tau$) of 400_L and 400_H with respect to bare Fe_2O_3 suggests enhanced electron mobility for the Fe_2O_3–TiO_2 heterostructure. TAS amplitude for 400_L and 400_H is higher with respect to bare Fe_2O_3 (Figure 5a), indicating therefore a higher amount of holes surviving the initial electron–hole recombination in the TiO_2 functionalized photoanodes. The long-lived components with the positive absorption were assigned to holes participating to water oxidation, and were resolved more accurately in a millisecond-to-second timescale (see below) in which water splitting has been reported to occur.[57,63]

The TAS decays of the specimens in a second time range and at a probe wavelength of λ = 650 nm, corresponding to the hole absorption in both Fe_2O_3 and TiO_2,[58,62] were fitted with an exponential model, shown in Figure 5b (see also Figure S8, Supporting Information). Functionalization of Fe_2O_3 with TiO_2 decreased the lifetime of long-lived photoholes, as indicated by the mean lifetimes of 3.0 and 1.8 s obtained for the bare Fe_2O_3 and 400_L photoanodes, respectively. This phenomenon is in good agreement with the higher PEC response of the TiO_2 containing specimens, as it demonstrates an enhanced water oxidation reaction rate. Previously published hole lifetimes for water oxidation over TiO_2 photoelectrodes were close to 0.3 s.[61,63] Hence, despite the presence of the TiO_2 overlayer, hole dynamics of specimen 400_L are directly influenced by the presence of the underlying hematite. Moreover, a photohole lifetime of 0.5 s was obtained for specimen 400_H (Figure 5b), close to the above literature value for bare TiO_2. The decreased photohole lifetime for 400_H with respect to bare Fe_2O_3 and 400_L is noticeable already on a millisecond timescale in Figure 5. The uniform and thicker coverage of Fe_2O_3 by TiO_2 in specimen 400_H can likely be considered responsible for the similar hole lifetimes as published perviously for pure TiO_2. The faster surface reaction kinetics with the thicker TiO_2

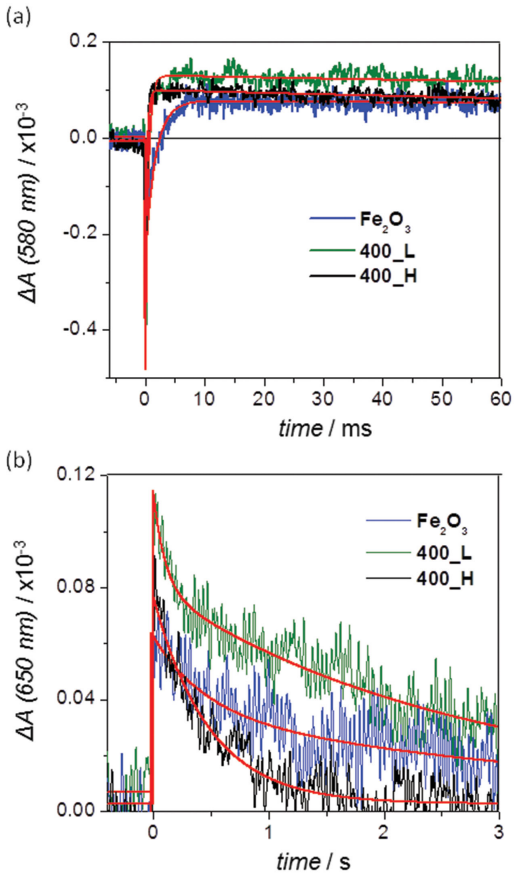

Figure 5. TAS decays for bare Fe_2O_3 and Fe_2O_3–TiO_2 samples on a) a millisecond and b) a second timescale. Red lines represent exponential fits of raw data.

overlayer directly explains the higher PEC response of this photoanode in comparison to the 400_L one, overcoming the slow OER kinetics typical for Fe_2O_3.

Picosecond TAS decays for the bare Fe_2O_3, 400_L, and 400_H photoanodes were compared at 580 nm to investigate the effect of TiO_2 functionalization on initial electron–hole recombination in Fe_2O_3. The retarded electron–hole recombination on the <10 ps time range for the Fe_2O_3–TiO_2 specimens (Figure S9, Supporting Information) was assigned to the passivation of Fe_2O_3 surface defects by TiO_2 deposition,[6] favoring, in turn, a decrease in detrimental charge recombination events.

To rationalize the obtained data, it is necessary to consider that the lower valence band energy of TiO_2 with respect to Fe_2O_3 potentially prohibits hole transfer from Fe_2O_3 to TiO_2,[64] and this phenomenon should lead to a decreased PEC response. However, as demonstrated by Figure 4 and the related discussion, the photocurrent response of TiO_2 functionalized specimens (400_L and 400_H) significantly outperforms that of the bare hematite (Fe_2O_3). Such a remarkable PEC enhancement suggests an efficient charge carrier separation upon coupling the two components in the resulting Fe_2O_3–TiO_2 photoelectrodes. In particular, the role of the junction can be illustrated by analyzing the energy band diagram presented in Scheme 1a,b without and with applied external bias.[24,57,58,65] The system Fermi level energy is lowered with increasing positive bias, which further promotes band bending at the interfaces, an effect that becomes more pronounced upon raising the applied potential. We propose that high photocurrents are achieved only after the valence band energy of hematite shifts to lower values with respect to the TiO_2 valence band edge at the electrolyte interface, promoting thus hole transfer from Fe_2O_3 to TiO_2. This conclusion is supported by the fact that no photocurrent plateau was observed for the TiO_2 functionalized specimens (Figure 4), attributed to enhanced driving force for hole transfer through TiO_2 with respect to increasing anodic potential that further promotes band bending (Scheme 1). In addition, hole conduction from Fe_2O_3 to titania via TiO_2 electronic defect states can be considered as a possible alternative hole transport mechanism.[24]

On the basis of these results, the high PEC response for the TiO_2 functionalized specimens are due to: i) formation of the Fe_2O_3-TiO_2 heterojunction promoting charge separation, and ii) enhanced hole dynamics for water oxidation due to titania overlayer functionalization. In addition, band bending, becoming more important upon raising the applied external bias, further enhances spatial charge separation by hole transport through the TiO_2 overlayer (Scheme 1b).

3. Conclusions

In conclusion, we have successfully prepared Fe_2O_3–TiO_2 nanoheterostructure photoanodes on FTO by the initial PE-CVD growth of Fe_2O_3 nanosystems followed by ALD of TiO_2 layers with variable thickness and final annealing in air. The inherent benefits of the adopted joint process have enabled the fabrication of high-purity systems, characterized by an intimate contact between Fe_2O_3 and TiO_2. These features synergistically contributed to the extremely high performances in photoelectrochemical water oxidation activated by solar illumination, which corresponded to ≈2.0 mA cm^{-2} photocurrent density at 1.23 V vs. RHE under simulated one-sun irradiation. The significant amplification in the PEC performance with respect to the case of bare Fe_2O_3 was mainly attributed to the beneficial role of Fe_2O_3–TiO_2 heterojunctions, resulting in an enhanced charge separation and retarded electron–hole recombination. In addition, TiO_2 protective action against corrosion has enabled the obtainment of attractive preliminary results even for PEC tests in seawater, whose use in solar water splitting is reported for the first time for Fe_2O_3–TiO_2 systems. These results, along with the high and stable photoanode activity, pave the way to sustainable energy generation starting from abundant and renewable natural resources through cost-effective nano-heterostructure devices. The proposed strategy and, in particular, the surface functionalization using ALD-deposited layers, may open doors to the use of combined synthesis approaches in the fabrication of a variety of nanostructures for photoassisted applications displaying improved functionalities.

Based on the present data, optimization of the material performances will require a fine tailoring of Fe_2O_3 morphology to obtain nanosystems endowed with higher porosity, and the investigation of higher TiO_2 loadings on such materials and on the ultimate functional behavior. Furthermore, detailed studies on the properties of the developed systems by incident photon-to-current efficiency, external quantum efficiency, and impedance spectroscopy analyses will also be performed, in order to attain a detailed insight on the heterojunction properties.

4. Experimental Section

4.1. Synthesis

Fe_2O_3 nanodeposits were fabricated using a custom-built two-electrode PE-CVD apparatus [radio frequency (RF) = 13.56 MHz; electrode diameter = 9 cm; interelectrode distance = 6 cm].[41] Depositions were performed on previously cleaned[41,66] FTO-coated glass substrates (Aldrich, 735167-1EA, ≈7 Ω sq^{-1}; lateral dimensions = 2.0 × 1.0 cm; FTO thickness ≈600 nm). Iron(III) oxide systems were prepared starting from $Fe(hfa)_2TMEDA$ (hfa = 1,1,1,5,5,5–hexafluoro–2,4–pentanedionate; TMEDA = *N,N,N′,N′*–tetramethylethylenediamine).[67] In a typical growth experiment, 0.30 ± 0.01 g of precursor powders were placed in an external glass reservoir, heated by an oil bath at 65 °C, and transported into the reaction chamber by electronic grade Ar [flow rate = 60 standard cubic centimeters per minute (sccm)]. In order to prevent undesired precursor condensation phenomena, connecting gas lines were maintained at 140 °C by means of external heating tapes. Two additional gas inlets were used for the independent introduction of electronic grade Ar and O_2 (flow rates = 15 and 20 sccm, respectively) directly into the reaction chamber. After preliminary optimization experiments, each deposition was carried out for 1 h under the following conditions: growth temperature = 400 °C; total reactor pressure = 1.0 mbar; RF-power of 10 W.

The as-prepared Fe_2O_3 nanodeposits were subsequently coated with TiO_2 layers of different thicknesses by means of ALD. ALD experiments were performed at a deposition temperature of 150 °C by a Ultratech/Cambridge Nanotech Inc. Savanna 100 machine operating between 13–15 mbar in continuous flow mode at 20 sccm. Titanium oxide was deposited starting from titanium(IV) tetraisopropoxide $[Ti(O^iPr)_4]$ and milliQ water (H_2O) as Ti and O sources, respectively. $Ti(O^iPr)_4$ was purchased from STREM Chemicals, Inc. (France) and used without any further purification. MilliQ water was produced by means of a Millipore DirectQ-5 purification system starting from tap water. The precursors were injected in the reactor directly from stainless steel reservoirs maintained at 80 °C $[Ti(O^iPr)_4]$ and 25 °C (H_2O). Electronic grade N_2 was used as carrier to feed the precursor vapors alternatively into the reaction chamber. To avoid precursor condensation, both valves and delivery lines were maintained at 115 °C. After an initial prescreening of the operating conditions, the use of thicker titania overlayers has been intentionally discarded in order to prevent the obtainment of too compact systems with reduced active area, a feature that could detrimentally affect the ultimate functional performances. After this optimization process, the cycle numbers were selected (Table 1) in order to obtain TiO_2 overlayers with the desired thickness.

After deposition, thermal treatments were carried out in air for 1 h at atmospheric pressure using a Carbolite HST 12/200 tubular furnace (heating rate = 20 °C min^{-1}) at 650 °C. The use of higher temperatures was discarded, to prevent detrimental thermal degradations of FTO substrates.[43]

4.2. Characterization

FE-SEM analyses were carried out using a Zeiss SUPRA 40 VP FE-SEM instrument equipped with an Oxford INCA X-sight X-ray detector for EDXS investigation, operating at primary beam acceleration voltages comprised between 10.0 and 20.0 kV.

AFM analyses were run using an NT-MDT SPM solver P47H-PRO instrument operating in semicontact/tapping mode and in air. After plane fitting, RMS roughness values were obtained from 3 × 3 μm^2 images.

SIMS investigation was performed by means of an IMS 4f mass spectrometer (Cameca) using a Cs^+ primary beam (voltage = 14.5 keV; current = 25 nA; stability = 0.2%) and negative secondary ion detection, adopting an electron gun for charge compensation. Beam blanking mode and high mass resolution configuration were adopted. Signals were recorded rastering over a 150 × 150 μm^2 area and detecting secondary ions from a subregion close to 10 × 10 μm^2 in order to avoid crater effects.

XRD measurements were conducted operating in reflection mode by means of a Dymax-RAPID microdiffractometer equipped with a cylindrical imaging plate detector, allowing data collection from 0° to 160° (2θ) horizontally and from −45° to +45° (2θ) vertically upon using Cu$K\alpha$ radiation (λ = 1.54056 Å). Each pattern was collected with an exposure time of 40 min, using a collimator diameter of 300 μm. Conventional XRD patterns were obtained by integration of 2D images.

TEM, HAADF-STEM, and EDXS mapping experiments were carried out on a FEI Tecnai Osiris microscope, operated at 200 kV and equipped with a Super-X high solid angle energy-dispersive X-ray detector, as well as a FEI Titan "cubed" microscope (acceleration voltage = 200 kV), equipped with an aberration corrector for the probe-forming lens and a Super-X high solid angle EDXS detector.

XPS analyses were run on a Perkin–Elmer Φ 5600ci apparatus with a standard Al$K\alpha$ radiation ($h\nu$ = 1486.6 eV), at operating pressures <10^{-8} mbar. Charge correction was performed by assigning to the adventitious C1s signal a Binding Energy (BE) of 284.8 eV.[68] After a Shirley-type background subtraction, atomic percentages (at%) were calculated by signal integration using standard PHI V5.4A sensitivity factors.

Optical absorption spectra were recorded in transmission mode at normal incidence by means of a Cary 50 spectrophotometer, using bare FTO glass as a reference. In all cases, the substrate contribution was subtracted. Tauc plots were determined based on the Tauc equation, assuming the occurrence of direct allowed transitions.[41,43]

PEC measurements were performed in unbuffered 1 M NaOH solutions and, for selected systems, in simulated sea water (35 g L^{-1} sea salt from Tropic Marin), using a saturated calomel electrode (SCE) as reference, a Pt wire as counter-electrode and the Fe_2O_3–TiO_2 nanodeposits as working electrodes. A copper wire was soldered on an uncovered portion of the FTO substrate to establish electrical connection, and an epoxy resin was used to seal all exposed FTO portions, except for the electrode working areas.[69] Prior to measurements, the electrolyte was purged with N_2 to prevent any possible reaction with dissolved O_2. Linear sweep voltammetry (10 mV s^{-1}) was carried out between −1.0 and 1.0 V vs. SCE using a potentiostat (PAR, Versa state IV), both in the dark and under front side illumination, using a Xe lamp (150 W, Oriel) with an AM 1.5 filter. Potentials with respect to the RHE scale (E_{RHE}) were calculated using the Nernst equation.[35]

$$E_{RHE} = E_{SCE} + E^0_{SCE} + 0.059\text{pH} \quad (1)$$

where E_{SCE} and E^0_{SCE} are the actual and standard potentials against SCE.

STH efficiency values are calculated based on the following equation[5,34]

$$\text{STH efficiency}(\%) = j \times (1.23 - E_{RHE}) / I_{light} \quad (2)$$

where E_{RHE} is the applied bias vs. RHE and I_{light} denotes the irradiance intensity (equal to 100 mW cm^{-2} for AM 1.5G illumination).

TAS experiments were performed on photoanodes having a geometric area of 3 × 3 cm^2 in a three-electrode PEC cell (Zahner-elektrik PECC-2) with a Pt counter-electrode, an Ag/AgCl (3 M KCl) reference electrode, and 0.1 M NaOH electrolyte (degassed with N_2 prior to measurements). A potential value of 1.6 V vs. RHE was controlled by a

standard potentiostat (CompactStat, Ivium Technologies) to probe the charge dynamics under water splitting conditions. TAS measurements in a microsecond-to-second timescale were carried out by a modified flash-photolysis apparatus (Luzchem LFP-111) with a New Focus (model 2051) photodetector and a halogen lamp (9 W, Thorlabs SLS201/M) probe. The excitation was fixed at $\lambda = 355$ nm, with an energy density of 0.4 mJ cm^{-2}. The transient absorption traces were averaged 50–80 times. The microsecond-to-second decays are smoothed by using the Savitzky–Golay method with 25 smoothing point.

The picosecond-to-nanosecond TAS experiments were performed by a pump-probe system consisting of Libra F-1K (Coherent Inc.) generator producing 100 fs pulses at $\lambda = 800$ nm (1 mJ) with a repetition rate of 1 kHz.[70] An optical parametric amplifier (Topas-C, Light Conversion Ltd.) was used to provide pump pulses at $\lambda = 355$ nm. The measuring component was ExciPro (CDP Inc.) equipped with two array photodetectors coupled with a spectrometer (CDP2022i) set for probe detection in the 500–700 nm interval, with averaging over 10 000 excitation shots. The maximum time range available for probing was ≈6 ns. TAS decays were fitted by using exponential functions in order to elucidate the charge transfer processes and corresponding timescales in the studied photoanode systems.

Supporting Information

Supporting Information is available from the Wiley Online Library or from the author.

Acknowledgements

The authors kindly acknowledge the financial support under the FP7 project "SOLAROGENIX" (NMP4-SL-2012-310333), as well as Padova University ex-60% 2012–2014 projects, Grant No. CPDR132937/13 (SOLLEONE), and Regione Lombardia-INSTM ATLANTE projects. S.T. acknowledges the FWO Flanders for a postdoctoral scholarship.

Received: June 12, 2015
Revised: July 24, 2015
Published online: September 5, 2015

[1] S. J. A. Moniz, S. A. Shevlin, D. J. Martin, Z.-X. Guo, J. Tang, *Energy Environ. Sci.* **2015**, *8*, 731.
[2] R. Liu, Z. Zheng, J. Spurgeon, X. Yang, *Energy Environ. Sci.* **2014**, *7*, 2504.
[3] W. H. Hung, T. M. Chien, A. Y. Lo, C. M. Tseng, D. D. Li, *RSC Adv.* **2014**, *4*, 45710.
[4] P. Luan, M. Xie, X. Fu, Y. Qu, X. Sun, L. Jing, *Phys. Chem. Chem. Phys.* **2015**, *17*, 5043.
[5] S. Hernández, V. Cauda, D. Hidalgo, V. Farías Rivera, D. Manfredi, A. Chiodoni, F. C. Pirri, *J. Alloys Compd.* **2014**, *615*, S530.
[6] X. Yang, R. Liu, C. Du, P. Dai, Z. Zheng, D. Wang, *ACS Appl. Mater. Interfaces* **2014**, *6*, 12005.
[7] M. Rioult, H. Magnan, D. Stanescu, A. Barbier, *J. Phys. Chem. C* **2014**, *118*, 3007.
[8] D. Barreca, G. Carraro, V. Gombac, A. Gasparotto, C. Maccato, P. Fornasiero, E. Tondello, *Adv. Funct. Mater.* **2011**, *21*, 2611.
[9] G. Carraro, C. Maccato, A. Gasparotto, T. Montini, S. Turner, O. I. Lebedev, V. Gombac, G. Adami, G. Van Tendeloo, D. Barreca, P. Fornasiero, *Adv. Funct. Mater.* **2014**, *24*, 372.
[10] D. P. Cao, W. J. Luo, J. Y. Feng, X. Zhao, Z. S. Li, Z. G. Zou, *Energy Environ. Sci.* **2014**, *7*, 752.
[11] G. K. Mor, H. E. Prakasam, O. K. Varghese, K. Shankar, C. A. Grimes, *Nano Lett.* **2007**, *7*, 2356.
[12] L. Wang, C. Y. Lee, P. Schmuki, *Electrochem. Commun.* **2013**, *30*, 21.
[13] X. J. Lian, X. Yang, S. J. Liu, Y. Xu, C. P. Jiang, J. W. Chen, R. L. Wang, *Appl. Surf. Sci.* **2012**, *258*, 2307.
[14] C. X. Kronawitter, Z. Ma, D. Liu, S. S. Mao, B. R. Antoun, *Adv. Energy Mater.* **2012**, *2*, 52.
[15] J. H. Kim, J. H. Kim, J.-W. Jang, J. Y. Kim, S. H. Choi, G. Magesh, J. Lee, J. S. Lee, *Adv. Energy Mater.* **2015**, *5*, 1401933.
[16] P. Luan, M. Xie, D. Liu, X. Fu, L. Jing, *Sci. Rep.* **2014**, *4*, 6180.
[17] O. Zandi, B. M. Klahr, T. W. Hamann, *Energy Environ. Sci.* **2013**, *6*, 634.
[18] B. Klahr, S. Gimenez, F. Fabregat-Santiago, T. Hamann, J. Bisquert, *J. Am. Chem. Soc.* **2012**, *134*, 4294.
[19] F. Le Formal, N. Tetreault, M. Cornuz, T. Moehl, M. Grätzel, K. Sivula, *Chem. Sci.* **2011**, *2*, 737.
[20] L. Steier, I. Herraiz-Cardona, S. Gimenez, F. Fabregat-Santiago, J. Bisquert, S. D. Tilley, M. Grätzel, *Adv. Funct. Mater.* **2014**, *24*, 7681.
[21] H. Magnan, D. Stanescu, M. Rioult, E. Fonda, A. Barbier, *Appl. Phys. Lett.* **2012**, *101*, 133908.
[22] S. Li, P. Zhang, X. Song, L. Gao, *Int. J. Hydrogen Energy* **2014**, *39*, 14596.
[23] F. Le Formal, M. Grätzel, K. Sivula, *Adv. Funct. Mater.* **2010**, *20*, 1099.
[24] S. Hu, M. R. Shaner, J. A. Beardslee, M. Lichterman, B. S. Brunschwig, N. S. Lewis, *Science* **2014**, *344*, 1005.
[25] D. A. Wheeler, G. Wang, Y. Ling, Y. Li, J. Z. Zhang, *Energy Environ. Sci.* **2012**, *5*, 6682.
[26] G. M. Carroll, D. K. Zhong, D. R. Gamelin, *Energy Environ. Sci.* **2015**, *8*, 577.
[27] W.-H. Hung, T.-M. Chien, C.-M. Tseng, *J. Phys. Chem. C* **2014**, *118*, 12676.
[28] D. Wang, X.-T. Zhang, P.-P. Sun, S. Lu, L.-L. Wang, Y.-A. Wei, Y.-C. Liu, *Int. J. Hydrogen Energy* **2014**, *39*, 16212.
[29] C. Zhang, Q. Wu, X. Ke, J. Wang, X. Jin, S. Xue, *Int. J. Hydrogen Energy* **2014**, *39*, 14604.
[30] Q. Yu, X. Meng, T. Wang, P. Li, J. Ye, *Adv. Funct. Mater.* **2015**, *25*, 2686.
[31] M. Marelli, A. Naldoni, A. Minguzzi, M. Allieta, T. Virgili, G. Scavia, S. Recchia, R. Psaro, V. Dal Santo, *ACS Appl. Mater. Interfaces* **2014**, *6*, 11997.
[32] S. C. Warren, K. Voïtchovsky, H. Dotan, C. M. Leroy, M. Cornuz, F. Stellacci, C. Hébert, A. Rothschild, M. Grätzel, *Nat. Mater.* **2013**, *12*, 842.
[33] Y. Lin, S. Zhou, S. W. Sheehan, D. Wang, *J. Am. Chem. Soc.* **2011**, *133*, 2398.
[34] P. Sharma, P. Kumar, D. Deva, R. Shrivastav, S. Dass, V. R. Satsangi, *Int. J. Hydrogen Energy* **2010**, *35*, 10883.
[35] G. Wang, Y. Ling, D. A. Wheeler, K. E. N. George, K. Horsley, C. Heske, J. Z. Zhang, Y. Li, *Nano Lett.* **2011**, *11*, 3503.
[36] N. T. Hahn, C. B. Mullins, *Chem. Mater.* **2010**, *22*, 6474.
[37] N. Mirbagheri, D. Wang, C. Peng, J. Wang, Q. Huang, C. Fan, E. E. Ferapontova, *ACS Catal.* **2014**, *4*, 2006.
[38] Z. Fu, T. Jiang, Z. Liu, D. Wang, L. Wang, T. Xie, *Electrochim. Acta* **2014**, *129*, 358.
[39] L. Xi, S. Y. Chiam, W. F. Mak, P. D. Tran, J. Barber, S. C. J. Loo, L. H. Wong, *Chem. Sci.* **2013**, *4*, 164.
[40] M. H. Lee, J. H. Park, H. S. Han, H. J. Song, I. S. Cho, J. H. Noh, K. S. Hong, *Int. J. Hydrogen Energy* **2014**, *39*, 17501.
[41] D. Barreca, G. Carraro, A. Gasparotto, C. Maccato, C. Sada, A. P. Singh, S. Mathur, A. Mettenbörger, E. Bontempi, L. E. Depero, *Int. J. Hydrogen Energy* **2013**, *38*, 14189.
[42] S. Shen, C. X. Kronawitter, D. A. Wheeler, P. Guo, S. A. Lindley, J. Jiang, J. Z. Zhang, L. Guo, S. S. Mao, *J. Mater. Chem. A* **2013**, *1*, 14498.

[43] M. E. A. Warwick, K. Kaunisto, D. Barreca, G. Carraro, A. Gasparotto, C. Maccato, E. Bontempi, C. Sada, T.-P. Ruoko, S. Turner, G. Van Tendeloo, *ACS Appl. Mater. Interfaces* **2015**, *7*, 8667.
[44] C. H. Miao, T. F. Shi, G. P. Xu, S. L. Ji, C. H. Ye, *ACS Appl. Mater. Interfaces* **2013**, *5*, 1310.
[45] S. J. A. Moniz, S. A. Shevlin, X. An, Z.-X. Guo, J. Tang, *Chem. Eur. J.* **2014**, *20*, 15571.
[46] M. T. Mayer, Y. Lin, G. Yuan, D. Wang, *Acc. Chem. Res.* **2013**, *46*, 1558.
[47] C. X. Kronawitter, L. Vayssieres, S. Shen, L. Guo, D. A. Wheeler, J. Z. Zhang, B. R. Antoun, S. S. Mao, *Energy Environ. Sci.* **2011**, *4*, 3889.
[48] J. Y. Kim, G. Magesh, D. H. Youn, J.-W. Jang, J. Kubota, K. Domen, J. S. Lee, *Sci. Rep.* **2013**, *3*, 2681.
[49] D. Barreca, G. Carraro, A. Gasparotto, C. Maccato, F. Rossi, G. Salviati, M. Tallarida, C. Das, F. Fresno, D. Korte, U. L. Stangar, M. Franko, D. Schmeisser, *ACS Appl. Mater. Interfaces* **2013**, *5*, 7130.
[50] Z. Li, W. Luo, M. Zhang, J. Feng, Z. Zou, *Energy Environ. Sci.* **2013**, *6*, 347.
[51] Y. Ling, G. Wang, D. A. Wheeler, J. Z. Zhang, Y. Li, *Nano Lett.* **2011**, *11*, 2119.
[52] J. Luo, X. Xia, Y. Luo, C. Guan, J. Liu, X. Qi, C. F. Ng, T. Yu, H. Zhang, H. J. Fan, *Adv. Energy Mater.* **2013**, *3*, 737.
[53] Pattern N° 33–0664, JCPDS (2000).
[54] Pattern N° 00–021–1272, JCPDS (2000).
[55] S. M. Ji, H. Jun, J. S. Jang, H. C. Son, P. H. Borse, J. S. Lee, *J. Photochem. Photobiol., A* **2007**, *189*, 141.
[56] H. Joo, S. Bae, C. Kim, S. Kim, J. Yoon, *Sol. Energy Mater. Sol. Cells* **2009**, *93*, 1555.
[57] M. Barroso, S. R. Pendlebury, A. J. Cowan, J. R. Durrant, *Chem. Sci.* **2013**, *4*, 2724.
[58] S. R. Pendlebury, X. Wang, F. Le Formal, M. Cornuz, A. Kafizas, S. D. Tilley, M. Grätzel, J. R. Durrant, *J. Am. Chem. Soc.* **2014**, *136*, 9854.
[59] B. C. Fitzmorris, J. M. Patete, J. Smith, X. Mascorro, S. Adams, S. S. Wong, J. Z. Zhang, *ChemSusChem* **2013**, *6*, 1907.
[60] A. J. Cowan, W. Leng, P. R. F. Barnes, D. R. Klug, J. R. Durrant, *Phys. Chem. Chem. Phys.* **2013**, *15*, 8772.
[61] J. Tang, J. R. Durrant, D. R. Klug, *J. Am. Chem. Soc.* **2008**, *130*, 13885.
[62] A. J. Cowan, C. J. Barnett, S. R. Pendlebury, M. Barroso, K. Sivula, M. Grätzel, J. R. Durrant, D. R. Klug, *J. Am. Chem. Soc.* **2011**, *133*, 10134.
[63] J. Tang, A. J. Cowan, J. R. Durrant, D. R. Klug, *J. Phys. Chem. C* **2011**, *115*, 3143.
[64] J. B. Baxter, C. Richter, C. A. Schmuttenmaer, *Annu. Rev. Phys. Chem.* **2014**, *65*, 423.
[65] L. Peng, T. Xie, Y. Lu, H. Fan, D. Wang, *Phys. Chem. Chem. Phys.* **2010**, *12*, 8033.
[66] G. Carraro, A. Gasparotto, C. Maccato, E. Bontempi, F. Bilo, D. Peeters, C. Sada, D. Barreca, *Cryst. Eng. Commun.* **2014**, *16*, 8710.
[67] D. Barreca, G. Carraro, A. Devi, E. Fois, A. Gasparotto, R. Seraglia, C. Maccato, C. Sada, G. Tabacchi, E. Tondello, A. Venzo, M. Winter, *Dalton Trans.* **2012**, *41*, 149.
[68] D. Briggs, M. P. Seah, *Practical Surface Analysis: Auger and X-ray Photoelectron Spectroscopy*, 2nd ed., John Wiley and Sons, New York **1990**.
[69] S. Kumari, A. P. Singh, Sonal, D. Deva, R. Shrivastav, S. Dass, V. R. Satsangi, *Int. J. Hydrogen Energy* **2010**, *35*, 3985.
[70] D. Sirbu, C. Turta, A. C. Benniston, F. Abou-Chahine, H. Lemmetyinen, N. V. Tkachenko, C. Wood, E. Gibson, *RSC Adv.* **2014**, *4*, 22733.

Publication III

Ali Kaouk, Tero-Petri Ruoko, Yakup Gönüllü, Kimmo Kaunisto, Andreas Mettenbörger, Evgeny Gurevich, Helge Lemmetyinen, Andreas Ostendorf, and Sanjay Mathur,

"Graphene-intercalated Fe_2O_3/TiO_2 heterojunctions for efficient photoelectrolysis of water"

RSC Advances, vol. 5, iss. 123, pp. 101401 – 101407, 2015

Reproduced with permission from The Royal Society of Chemistry

RSC Advances

PAPER

View Article Online
View Journal | View Issue

Cite this: *RSC Adv.*, 2015, **5**, 101401

Graphene-intercalated Fe_2O_3/TiO_2 heterojunctions for efficient photoelectrolysis of water†

A. Kaouk,[a] T.-P. Ruoko,[ab] Y. Gönüllü,[a] K. Kaunisto,[b] A. Mettenbörger,[a] E. Gurevich,[c] H. Lemmetyinen,[b] A. Ostendorf[c] and S. Mathur*[a]

Received 8th September 2015
Accepted 5th November 2015

DOI: 10.1039/c5ra18330h

www.rsc.org/advances

Interfacial modification of α-Fe_2O_3/TiO_2 multilayer photoanodes by intercalating few-layer graphene (FLG) was found to improve water splitting efficiency due to superior transport properties, when compared to individual iron and titanium oxides and heterojunctions thereof. Both metal oxides and graphene sheets were grown by plasma-enhanced chemical vapor deposition. Compared to the onset potential achieved for α-Fe_2O_3 films (1 V *vs.* RHE), the α-Fe_2O_3/TiO_2 bilayer structure yielded a better onset potential (0.3 V *vs.* RHE). Heterojunctioned bilayers exhibited a higher photocurrent density (0.32 mA cm^{-2} at 1.23 V *vs.* RHE) than the single α-Fe_2O_3 layer (0.22 mA cm^{-2} at 1.23 V *vs.* RHE), indicating more efficient light harvesting and higher concentration of photogenerated charge carriers. For more efficient charge transport at the interface, a few layer graphene sheet was intercalated into the α-Fe_2O_3/TiO_2 interface, which substantially increased the photocurrent density to 0.85 mA cm^{-2} (1.23 V *vs.* RHE) and shifted the onset potential (0.25 V *vs.* RHE). Ultrafast transient absorption spectroscopy studies indicated that the incorporation of FLG between the α-Fe_2O_3 and TiO_2 layers resulted in reduced recombination in the α-Fe_2O_3 layer. The results showed that graphene intercalation improved the charge separation and the photocurrent density of the FTO/α-Fe_2O_3/FLG/TiO_2 system.

Introduction

In the on-going quest for clean and sustainable energy sources, the production of hydrogen through photochemical water splitting offer a promising solution to suppress the carbon footprint and emission of greenhouse gases.[1,2]

Transition metal oxides such as α-Fe_2O_3 and TiO_2 are favourable candidates that provide intrinsic advantages in terms of high photo-stability and sufficient mobility of charge carriers besides their earth-abundance.[3] Despite these advantages, no commercially viable material exists that would enable to maintain the proposed minimum 10% requirement for solar-to-hydrogen fuel efficiency (STH).[4] The wide band gap of TiO_2 (anatase 3.2 eV and rutile 3.0 eV) limits it's usage in solar hydrogen production under visible light illumination. As TiO_2 is photoactive largely in the UV spectral region, only a small portion (4%) of the solar spectrum can be utilized for photocatalytic processes.[5] In the case of hematite (α-Fe_2O_3), its suitable band gap (~2.0–2.2 eV) allows harvesting a significant portion of the solar spectrum. Moreover, hematite has a valence band edge which is favourable for water oxidation reaction.[4] Although hematite yields theoretically a 20% STH conversion efficiency for water splitting,[5] high STH values have not been reached due to a combination of a relatively long light penetration depth (*ca.* 100 nm at $\lambda = 500$ nm) and a short hole diffusion length (2–20 nm).[6,7] As a result, photo-generated holes that are originated deep in the material cannot reach the surface and are mostly lost in the recombination processes.

In the search for strategies enabling an enhancement of the photo-electrochemical properties of TiO_2, doping with different 3d transition elements (such as Fe, V,[8] Cr,[9] Mn,[10] Cu[11]) is a promising approach to increase the visible light activity.[12–15] In the case of hematite, it has been reported that the dendritic α-Fe_2O_3 films prepared by atmospheric pressure chemical vapour deposition (AP-CVD) yielded enhanced plateau photocurrents for water oxidation due to the generation of photoholes at short distances from the semiconductor liquid interface.[16] We have previously reported that hydrogen plasma treatment of hematite films is a simple and effective strategy for modifying the existing material to improve significantly the band edge positions and photo-electrochemical (PEC) performance.[17] Sharma *et al.* have shown that producing multilayered TiO_2/α-Fe_2O_3 electrodes through a sol–gel process yielded approximately a 10-fold improvement in photocurrent density over a single layer electrode.[18] However, depositing a multilayered structure with a liquid phase process creates more interfaces between the layers, resulting in recombination centers and traps for the

[a]*Institute of Inorganic Chemistry, University of Cologne, Cologne 50939, Germany. E-mail: sanjay.mathur@uni-koeln.de*

[b]*Department of Chemistry and Bioengineering, Tampere University of Technology, Tampere 33710, Finland*

[c]*Lehrstuhl für Laseranwendungstechnik, Ruhr-Universität Bochum, Bochum 44801, Germany*

† Electronic supplementary information (ESI) available. See DOI: 10.1039/c5ra18330h

charge carriers, which is detrimental for electron transport. Gas phase processes are used to limit the effect of interfacial interactions. Plasma enhanced chemical vapour deposition (PE-CVD) of dense layers decreases the interfacial surface area, thus improving electron mobility in multilayer systems.[19,20] Despite the enhancement in metal oxide interfacial interactions, gas phase depositions are still limited by surface trap states and interfacial charge carrier recombination. To overcome these setbacks, charge carrier recombination in the metal oxide interface should be limited. In this context, it has been reported that a graphene sheet between two layers could improve the electron transfer.[21]

In this study, we report on α-Fe_2O_3/TiO_2 multilayered structures for water splitting applications. The interface of α-Fe_2O_3/TiO_2 was modified by intercalating a sheet of "few layer graphene". Few layer graphene, α-Fe_2O_3 and TiO_2 films were deposited by PE-CVD in order to obtain sharp interfaces and dense layers with superior interfacial properties. The α-Fe_2O_3/TiO_2 bilayer electrode exhibited a better onset potential (0.3 V *vs.* RHE), defined as the potential were photocurrent density crosses 0 mA cm^{-2}, than an electrode having a single α-Fe_2O_3 layer (1 V *vs.* RHE), whereas the highest photocurrent density (approximately 1 mA cm^{-2} at 1.23 V *vs.* RHE) was generated by the α-Fe_2O_3/FLG/TiO_2 electrode. Ultrafast transient absorption spectroscopy (TAS) studies were performed under water splitting conditions to gain insight into the effects that the layering resulted in. It was observed that the graphene layer reduced ps–ns timescale recombination in the hematite layer, indicative of graphene mediated hole transfer from α-Fe_2O_3 to TiO_2. On the other hand, the α-Fe_2O_3/TiO_2 bilayer electrode exhibited faster recombination than the single α-Fe_2O_3 layer due to unfavourable band alignment of the materials. Thus, the improved onset potential and photocurrent of the bilayer system is presumably due to the simultaneous excitation of both materials.

Experimental section

Metal oxide deposition

Hematite films were deposited by radio frequency plasma enhanced chemical vapour deposition (PE-CVD) onto FTO substrates using iron pentacarbonyl ($Fe(CO)_5$) as the Fe source and pure oxygen gas as the O source, as reported elsewhere.[13,22] TiO_2 films were deposited *via* PECVD onto FTO substrates (as reference) and onto the graphene or hematite coated substrate by using titanium isopropoxide as a precursor. The as-grown films were amorphous and were annealed for 2 h in air at 750 °C to obtain crystalline hematite films (Fe_2O_3) and 500 °C for TiO_2.

Graphene deposition and transfer

The copper foil substrates (Alfa Aesar, 25 μm, 99.8%) were first dipped in an acetic acid bath to eliminate native oxides formed by the industrial process and storage,[23] after which the substrates were washed in water and isopropanol sonic bathes consecutively. The substrates were then annealed at 700 °C under vacuum to increase the grain size of the polycrystalline copper.

Treated copper substrates were used for hydrogen free PE-CVD deposition of graphene (Plasma Electronic). The substrates were placed in the PE-CVD chamber under a pressure of 2 Pa at 700 °C. The graphene deposition processes were done under a 10 : 1 argon to methane atmosphere with a RF power of 70 W.

A 10% PMMA (polymethyl methacrylate) in toluene solution was drop coated over the as-grown graphene layers and dried at 100 °C for 1 h.[24] The polymer covered substrate was then annealed at 180 °C for 2 h. After cooling to room temperature the copper substrate was etched in an aqueous solution of iron(III)nitrate ($Fe(NO_3)_3$) (25 w%). The graphene-polymer sheet was washed thoroughly with deionized water and picked up from water with the preferred substrate (Si, SiO_2, glass, FTO glass). After transfer the substrate was first dried in air and subsequently at 100 °C overnight. The polymer was finally dissolved in acetone and the graphene was rinsed in an isopropanol ultrasonic bath and blow dried.

Characterization

The powder X-ray diffraction patterns were measured (STOE-STADI MP) in reflection mode using Cu Kα (λ = 0.15406 nm) radiation. Film morphology was analysed by SEM (scanning electron microscopy, Nova Nano SEM 430 (FEI)) and absorption spectra were measured using an UV-visible spectrophotometer (Perkin-Elmer Lambda 950). PEC measurements were carried out in a three electrode electrochemical cell with a 1.0 M NaOH electrolyte using a potentiostat (PAR, Model: Versa state IV, USA) and a 150 W xenon lamp (Oriel), which was equipped with a AM1.5 filter to simulate the solar spectrum. As-grown and transferred graphene sheets were characterized using optical microscopy (Nikon Eclipse LV150) to check for the existence of layers. Layer uniformity was measured by STM (Park Systems XE-100). The number of layers and microscopic quality of the grown graphene was analysed by Raman spectroscopy (Renishaw excitation source 514 nm Ar laser). The topographic images of grown sheets were acquired by scanning electron microscopy (Carl Zeiss SMT Auriga™) and a focus ion beam (Crossbeam® FIB Workstation with Gemini® FESEM Column).

The ultrafast TAS studies were performed using the pump–probe method. The fundamental laser pulses were obtained with a Ti:sapphire laser (Libra F, Coherent Inc., 800 nm, ~100 fs pulse width, repetition rate 1 kHz). Approximately 90% of the fundamental beam energy was directed to an optical parametric amplifier (Topas C, Light Conversion Ltd.) to produce the excitation pump pulses at 475 nm with approximately 1 mm beam diameter at the sample, attenuated to 0.4 mJ cm^{-2} with neutral density filters. The probe pulses were obtained directing the remaining fundamental laser beam energy through a motorized translational stage to a Ti:sapphire crystal for white continuum generation. The probe pulses were split into two beams for use as reference and signal beams. The measurement system (ExciPro, CDP systems) was equipped with a Si CCD for the visible part of the spectrum. A chopper synchronized with

the fundamental laser pulses was used to block every second pump pulse, and the absorbance change was calculated from consecutive pulses. The absorbance changes were averaged 10 000 times per delay time. The whole measurement sequence was performed five times for each sample and averaged to minimize variations caused by excitation power fluctuations. The samples were kept in a three electrode electrochemical cell with 0.1 M NaOH electrolyte and held at a constant bias of 1.23 V *vs.* the reversible hydrogen electrode to gain insight into the changes in time-resolved absorption under water splitting conditions.

Results and discussion

PE-CVD deposition of graphene

Homogeneous few layer graphene deposits with flakes of sizes over 100 μm were obtained by PECVD of 10 : 1 argon to methane (Fig. 1a). The pre-treatment of the copper foil increased the domain sizes of the as-grown graphene layers, due to the increase in the grain size of copper (ranging from 80 μm to 100 μm).

As-grown few layer graphene layers were characterized by STM (Fig. 1b), indicating the presence of a high quality low defect graphene layer, displayed a clear hexagonal honeycomb structure.

The defect density in the synthesized graphene sheets was found to be very low ($I_D/I_G < 1$, Fig. 2a). Raman spectra of the as-grown and transferred graphene layers showed 4 peaks at 1350 cm^{-1}, 1600 cm^{-1}, 2700 cm^{-1} and 2950 cm^{-1}, corresponding to the D, G, 2D, and 2D′ peaks, respectively.[25] CVD-grown graphene typically exhibits two prominent peaks recognized as G and D peaks occurring at 1560 cm^{-1} and 1360 cm^{-1}, due to individual bond stretching, compressing (G band) and breathing modes of the hexagonal rings of carbon atoms (D band).[26] The D peak's intensity shows the amount of defects in the graphene structure, whereas, the ratio I_{2D}/I_G of the G peak with the 2D peak, which is the first harmonic of the D peak, shows the number of graphene layers (1–5 layers).[27] In all spectra, the peak appearing at 2950 cm^{-1} is due to the combination of two phonons with different momentums.[28] Raman spectra of the transferred graphene layers exhibited the same Raman shift peaks (D, G and 2D). The only difference observed was a more intense D peak, which is explained by folding and cracking of the layers during the wet transfer process, thus increasing defect density and increasing the intensity of the D peak (Fig. 2b).[29]

PE-CVD deposition of MO_x and MO_x/graphene material

The crystalline phase of as deposited and annealed layers of α-Fe_2O_3 and TiO_2 were determined by X-ray diffraction analysis to be hematite and anatase, respectively (Fig. 3b).

A few layer graphene sheet was transferred over a α-Fe_2O_3 thin layer, and a layer of TiO_2 was deposited over it. The pristine and composite materials were both characterized and their composition was determined with Raman spectroscopy. The 2D graphene peak can be seen at 1690 cm^{-1}, whereas the G peak is not observed due to the thick layer of metal oxide over (TiO_2) and under (α-Fe_2O_3) the graphene layer overwhelming the intensity of the peak. The wide peak at 1310 cm^{-1} is the D peak of the graphene (Fig. 3a), the high D peak intensity arises from defects due to the interaction between the graphene and α-Fe_2O_3 layers.[30]

Photo electrochemical activity of MO_x and composite materials

To overcome the drawbacks of α-Fe_2O_3, TiO_2 was deposited over it (Fig. 4a), and to further enhance the interfacial properties of

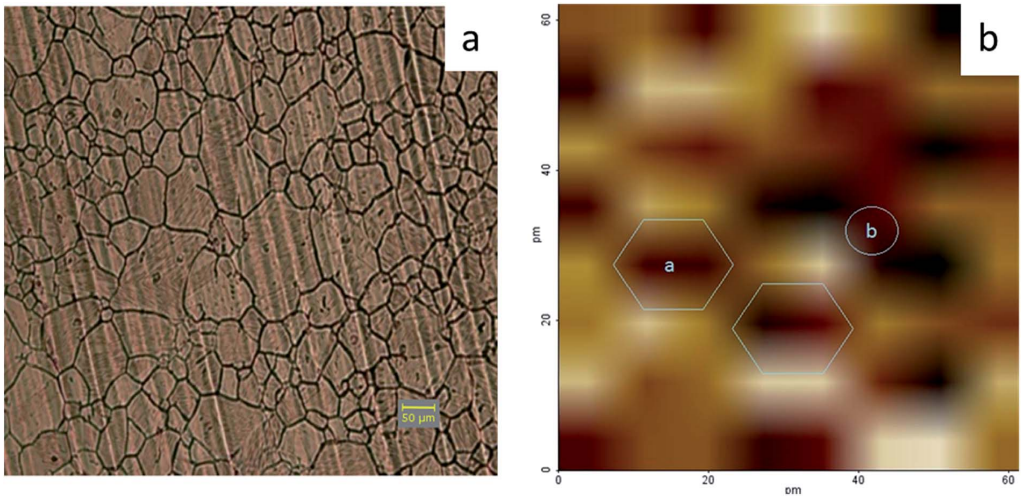

Fig. 1 Optical images of as-grown graphene on copper foil (a) and STM image of as-grown graphene on copper foil (bias voltage 1.3 V, scan size 5 nm) (b).

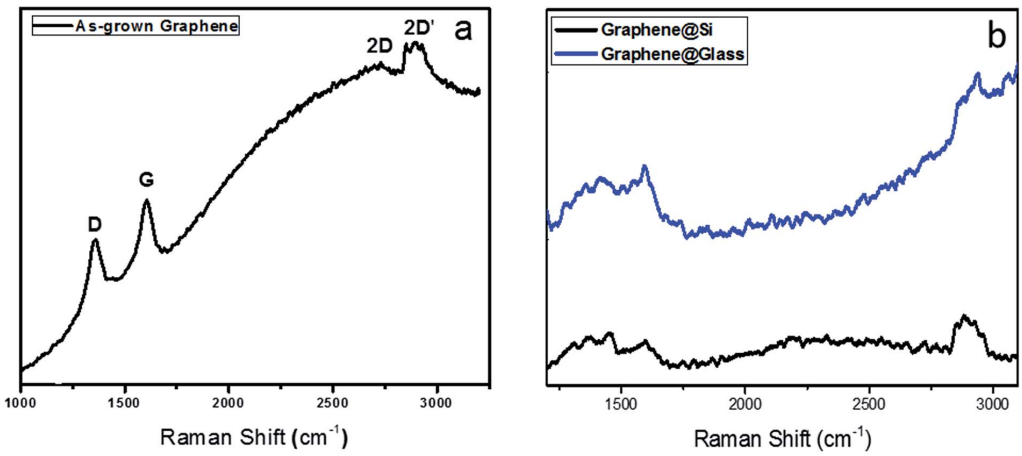

Fig. 2 Raman spectra of as-grown (a) and transferred (b) graphene on copper substrate.

the multilayer system graphene was intercalated in the metal oxide interface. Graphene's zero band gap property makes it an appropriate charge collector.[31] Photocurrent density and onset voltages of all studied photoanodes under solar illumination are displayed in Table 1. All mentioned potentials are presented against the reversible hydrogen electrode (RHE). The pristine α-Fe_2O_3 and TiO_2 electrodes showed photocurrent densities of 0.22 mA cm^{-2} and 0.43 mA cm^{-2} at 1.23 V, respectively (Fig. 5a).

Further enhancement of the photo electrochemical properties was achieved by depositing a layer of TiO_2 over pristine α-Fe_2O_3. This resulted in an onset potential of 0.3 V and an increase in the photocurrent density (0.32 mA cm^{-2} at 1.23 V) with respect to the pristine α-Fe_2O_3 electrode. The enhancement in onset potential is due to the favourable conduction band edge alignment of TiO_2 and α-Fe_2O_3, where photoelectrons generated in TiO_2 are injected to the conduction band of α-Fe_2O_3 due to its lower energy, leaving holes in the valence band of TiO_2 (Fig. 4).[32] With increased bias voltages photo holes generated in the α-Fe_2O_3 layer attain enough energy to possibly tunnel through the TiO_2 defect states, resulting in a rise in the level of photocurrent density of the double layer α-Fe_2O_3/TiO_2 electrode.

Photocurrent density was further enhanced by intercalating a few layer graphene sheet between the α-Fe_2O_3 and TiO_2 layers (Fig. 4b), the intercalated graphene layer cannot be seen in the cross-section image of the multilayer, due to its thickness (1–5 layers, <1.5 nm). The α-Fe_2O_3/FLG/TiO_2 composite electrode showed more than a 2-fold enhancement in photocurrent density over the α-Fe_2O_3/TiO_2 composite electrode (0.85 and 0.32 mA cm^{-2} at 1.23 V, respectively) while enhancing the onset

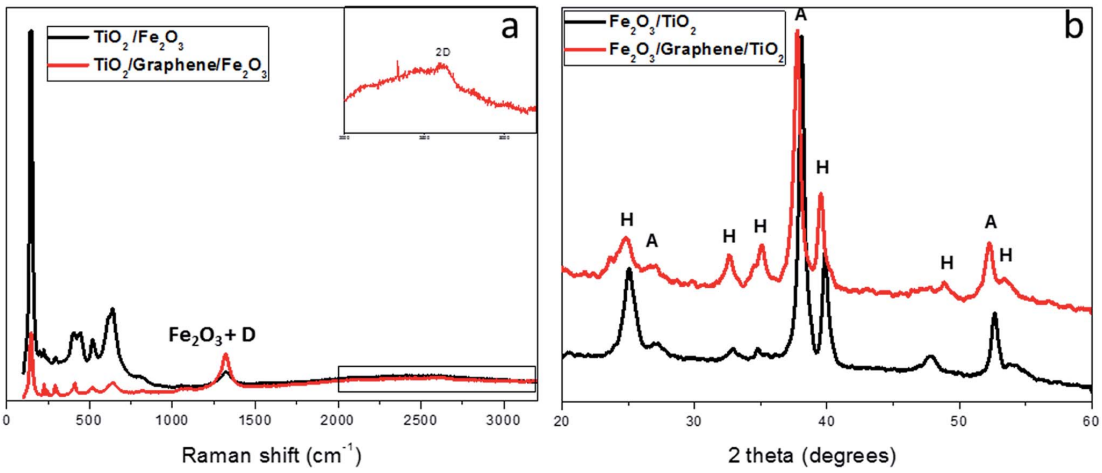

Fig. 3 Raman spectra (a) and X-ray diffraction patterns (b) of hematite α-Fe_2O_3 (H), anatase TiO_2 (A) and MO_x/graphene composite material.

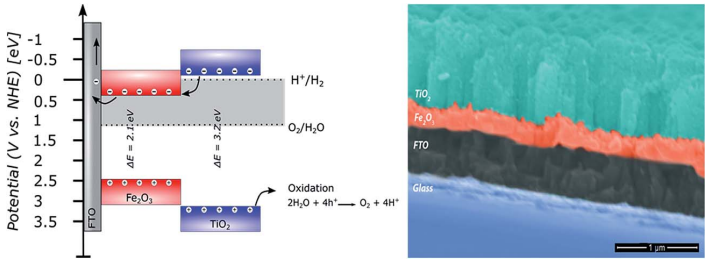

Fig. 4 Schematic band edge structure of α-Fe_2O_3/TiO_2 bilayer with the redox potentials of water (left); cross-section SEM image of the multilayer photoanode FTO/Fe_2O_3/FLG/TiO_2 (right).

Table 1 Photocurrent densities and onset potentials of fabricated electrodes

Sample	*J*@1.23 V *vs.* RHE (mA cm^{-2})	Onset potential (V *vs.* RHE)
TiO_2	0.43	0.3
Fe_2O_3	0.22	1
Fe_2O_3/TiO_2	0.32	0.3
Graphene/Fe_2O_3/TiO_2	0.67	0.75
Fe_2O_3/graphene/TiO_2	0.85	0.25

potential to 0.25 V (Table 1). The apparent enhancement arises from graphene's lower work function (−4.4 eV) compared to TiO_2 (−4.2 eV) making it easier for electrons to inject into the graphene layer rather than recombine at the MO_x/MO_x interface.[16] Thus, the presence of a graphene layer between the α-Fe_2O_3 and TiO_2 layers limits the electron/hole pair recombination at the α-Fe_2O_3/TiO_2 interface, which in turn increases the photocurrent density of the whole electrode. This fact is further proved in the FLG/α-Fe_2O_3/TiO_2 electrode where the measured photocurrent density (0.67 mA cm^{-2} at 1.23 V) is lower than that of α-Fe_2O_3/FLG/TiO_2 (Fig. 5b). This difference shows the role of the conductive band alignment in multi-layered systems (Fig. 4), making the α-Fe_2O_3/TiO_2 interface the optimal place for a layer of graphene to obtain the desired enhancing effect on the performance of the electrode.

Transient absorption spectroscopy

Ultrafast transient absorption spectroscopy was used to study the effects that lead to the increased photocurrent. The excitation wavelength (475 nm) was chosen to selectively excite hematite in the multilayer systems in water splitting conditions. Thus, the decay of the transient absorption reflects the recombination and charge separation efficiencies within the hematite layer in different samples. The normalized transient decays of the studied samples at a probe wavelength of 650 nm (Fig. 6), attributed to kinetics of photogenerated charge carriers in the ps time domain and holes on longer timescales.[33–35]

The TAS decay in the ps timescale is attributed to primary recombination processes, as indicated by similar decay dynamics up to 1 ps for all samples. On the other hand, the longer timescale decay is a mixture of electron–hole recombination, electron extraction and long-lived hole signal. The α-Fe_2O_3/TiO_2 electrode exhibits noticeably faster primary recombination processes than the single layer α-Fe_2O_3 electrode. This

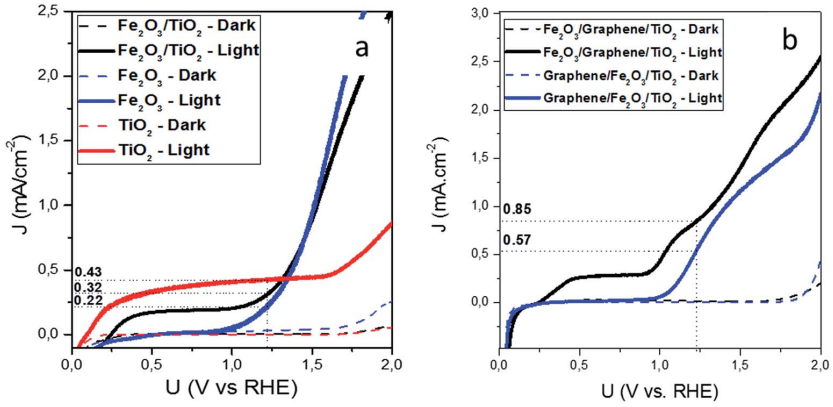

Fig. 5 Photocurrent densities under dark and light conditions of α-Fe_2O_3, TiO_2 and α-Fe_2O_3/TiO_2 (a) and Fe_2O_3/FLG/TiO_2 multilayer system (b).

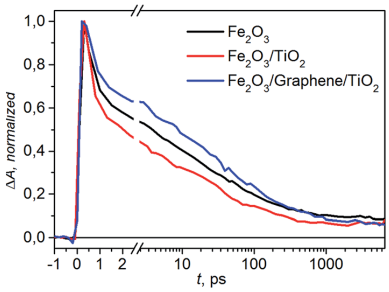

Fig. 6 Picosecond to nanosecond transient absorption decays probed at 650 nm for α-Fe_2O_3, α-Fe_2O_3/TiO_2 and α-Fe_2O_3/graphene/TiO_2.

is due to the fact that the valence band of TiO_2 is much lower than the valence band of α-Fe_2O_3,[36] creating a barrier for the photogenerated holes and increasing bulk recombination in the 1–1000 ps timescale. This results in a lower amount of long-lived holes in hematite that can take part in the water oxidation reaction due to the hole transfer barrier at the α-Fe_2O_3/TiO_2 interface. The higher photocurrent obtained with this sample over the single layer α-Fe_2O_3 can be explained by simultaneous excitation of both layers with simulated sunlight.

On the other hand, the α-Fe_2O_3/FLG/TiO_2 layer exhibits noticeably reduced recombination in the 1–1000 ps timescale. This is due to the fact that the photogenerated holes in hematite can now be transferred to the graphene layer, reducing recombination within the hematite layer and the interface between the metal oxide layers, thus allowing a greater number of photogenerated electrons to be conducted to the external circuit. The holes in graphene can recombine with photogenerated electrons from TiO_2, increasing the photohole lifetime within the titania layer. This explains the higher photocurrent at low bias voltages with this sample when compared with the α-Fe_2O_3/TiO_2 double layer.

Conclusions

PE-CVD α-Fe_2O_3/TiO_2 bilayer photoanodes were modified through intercalation of few layer graphene. The observed enhancement in photocurrent suggests that heterointerface α-Fe_2O_3/FLG/TiO_2 influences the band line-up, which is attributed primarily to modulation of dislocation density and charge carrier generation/recombination rates.

The α-Fe_2O_3/TiO_2 bilayer electrode exhibited enhanced PEC responses in terms of a lower onset potential and a higher photocurrent density when compared to the single layer α-Fe_2O_3 electrode. The incorporation of a graphene layer between the α-Fe_2O_3/TiO_2 double layer and the FTO substrate resulted in a doubling of the photocurrent, but lead to a loss of the synergistic effect between the two active metal oxide layers probably due to the change of band-alignment from staggered to broken bandgap. However, intercalating the graphene between the two active metal oxide layers resulted in an overall higher photocurrent, while retaining the enhanced onset potential of the double layer electrode. This enhancement was observed to be due to either the passivation of the oxide defect states or enhancement of the charge transfer between the two oxide layers. In conclusion, the results presented in this study illustrate the importance of interfacial modification of metal oxide photoanodes, resulting in greatly increased onset voltages and photocurrents that can be adapted to a broad range of metal oxide based systems.

Acknowledgements

The work was financially supported by SOLAROGENIX, Project (EC-FP7-Grant Agreement No. 214281) and the University of Cologne. AK and SM are thankful to the Lebanese National Council for Scientific Research for providing a fellowship to Mr Ali Kaouk. The authors are thankful to Dr Ing. Konstantinos Nalpantidis for Raman measurement, and Mr Ashish Lepcha for XRD measurement.

References

1 R. Dholam, N. Patel, A. Santini and A. Miotello, *Int. J. Hydrogen Energy*, 2010, **35**, 9581.
2 A. Fujishima, *Nature*, 1972, **238**, 37–38.
3 R. Dholam, N. Patel and A. Miotello, *Int. J. Hydrogen Energy*, 2011, **36**, 6519.
4 A. J. Cowan, C. J. Barnett, S. R. Pendlebury, M. Barroso, K. Sivula, M. Grätzel, J. R. Durrant and D. R. Klug, *J. Am. Chem. Soc.*, 2011, **133**, 10134.
5 I. Cesar, K. Sivula, A. Kay, R. Zboril and M. Grätzel, *J. Phys. Chem. C*, 2009, **113**, 772.
6 M. P. Dare-Edwards, J. Goodenough, A. Hamnett and P. Trevellick, *J. Chem. Soc., Faraday Trans. 1*, 1983, **79**, 2027.
7 R. Gardner, F. Sweett and D. Tanner, *J. Phys. Chem. Solids*, 1963, **24**, 1183.
8 R. Dholam, N. Patel and A. Miotello, *Int. J. Hydrogen Energy*, 2011, **35**(11), 6519.
9 R. Dholam, N. Patel and A. Miotello, *Int. J. Hydrogen Energy*, 2009, **34**(13), 5337.
10 K. Umar, M. M. Haque, M. Muneer, T. Harada and M. Matsumura, *J. Alloys Compd.*, 2013, **578**(25), 431–438.
11 C. Wang, Q. Hu, J. Huang, C. Zhu, Z. Deng, H. Shi, L. Wu, Z. Liu and Y. Cao, *Appl. Surf. Sci.*, 2014, **292**(15), 161.
12 Z. Fujishima and D. Tryk, *Surf. Sci. Rep.*, 2008, **63**, 515.
13 T. Choi and M. Hoffmann, *J. Phys. Chem.*, 1994, **84**, 13669.
14 J. Zhu, *Appl. Catal., B*, 2006, **62**, 329.
15 M. Khan, S. Woo and O. Yang, *Int. J. Hydrogen Energy*, 2008, **33**, 5345.
16 A. Kay, I. Cesar and M. Gratzel, *J. Am. Chem. Soc.*, 2006, **128**, 15714.
17 A. Mettenbörger, T. Singh, A. P. Singh, T. T. Järvi, M. Moseler, M. Valldor and S. Mathur, *Int. J. Hydrogen Energy*, 2014, **39**, 4828.
18 P. Sharma, P. Anjana Solanki, R. Shrivastav, S. Dass and V. R. Satsangi, *J. Solid State Electrochem.*, 2012, **16**, 1305.
19 M. Liu, M. Johnston and H. Snaith, *Nature*, 2013, **501**, 395.

20 M. Wang, M. Pyeon, Y. Gönüllü, A. Kaouk, S. Shen, L. Guo and S. Mathur, *Nanoscale*, 2015, **7**, 10094.
21 J. Wang, *et al.*, *Nano Lett.*, 2014, **14**(2), 724.
22 A. Singh, A. Mettenbörger, P. Golus and S. Mathur, *Int. J. Hydrogen Energy*, 2012, **37**, 13983–13988, DOI: 10.1016/j.ijhydene.2012.06.097.
23 M. Chhowalla, *J. Mater. Chem.*, 2011, **21**, 3324.
24 L. Colombo and R. Ruoff, *Nano Lett.*, 2009, **9**, 4359.
25 M. Dresselhaus, L. Malard, M. Pimenta and G. Dresselhaus, *Phys. Rep.*, 2009, **473**(5–6), 51.
26 A. C. Ferrari, J. C. Meyer, V. Scardaci, C. Casiraghi, M. Lazzeri, F. Mauri, S. Piscanec, D. Jiang, K. S. Novoselov, S. Roth and A. K. Geim, *Phys. Rev. Lett.*, 2006, **97**(18), 187401.
27 M. Pimenta, G. Dresselhaus, M. Dresselhaus, L. Cancado, A. Jorio and R. Saito, *Phys. Chem. Chem. Phys.*, 2007, **9**(11), 1276.
28 Z. Ni, T. Yu, Z. Luo, Y. Wang, L. Liu, C. Wong, J. Miao, W. Huang and Z. Shen, *ACS Nano*, 2009, **3**, 569.
29 X. Liang, B. A. Sperling, I. Calizo, G. Cheng, C. A. Hacker, Q. Zhang, Y. Obeng, K. Yan, H. Peng, Q. Li, X. Zhu, H. Yuan, A. R. Hight Walker, Z. Liu, L. Peng and C. Richter, *ACS Nano*, 2011, **5**(11), 9144.
30 M. Khenfouch, *et al.*, *Opt. Mater.*, 2013, **36**, 27.
31 R. Czerw, B. Foley, D. Tekleab, A. Rubio, P. Ajayan and D. Carroll, *Phys. Rev. B: Condens. Matter Mater. Phys.*, 2002, **66**(3), 033408.
32 S. Choudhary, S. Upadhyay, P. Kumar, N. Singh, V. R. Satsangi, R. Shrivastav and S. Dass, *Int. J. Hydrogen Energy*, 2012, **37**, 18712.
33 M. Barroso, S. Pendlebury, A. Cowan and J. Durrant, *Chem. Sci.*, 2013, **4**, 2724.
34 S. Pendlebury, X. Wang, F. le Formal, M. Cornuz, A. Kafizas, S. Tilley, M. Grätzel and J. Durrant, *J. Am. Chem. Soc.*, 2014, **136**, 9854.
35 A. Cowan, C. Barnett, S. Pendlebury, M. Barroso, K. Sivula, M. Grätzel, J. Durrant and D. Klug, *J. Am. Chem. Soc.*, 2011, **133**, 10134.
36 J. Baxter, C. Richter and C. Schmuttenmaer, *Annu. Rev. Phys. Chem.*, 2014, **65**, 423.

Publication IV

Ali Kaouk, Tero-Petri Ruoko, Myeongwhun Pyeon, Yakup Gönüllü, Kimmo Kaunisto, Helge Lemmetyinen, and Sanjay Mathur

"High water-splitting efficiency through intentional In and Sn codoping in hematite photoanodes"

The Journal of Physical Chemistry C, vol. 120, no. 49, pp. 28345 – 28353, 2016

THE JOURNAL OF PHYSICAL CHEMISTRY C

Article

pubs.acs.org/JPCC

High Water-Splitting Efficiency through Intentional In and Sn Codoping in Hematite Photoanodes

Ali Kaouk,[†] Tero-Petri Ruoko,[†,‡] Myeongwhun Pyeon,[†] Yakup Gönüllü,[†] Kimmo Kaunisto,[‡] Helge Lemmetyinen,[‡] and Sanjay Mathur*[,†]

[†]Institute of Inorganic Chemistry, University of Cologne, Cologne 50939, Germany

[‡]Department of Chemistry and Bioengineering, Tampere University of Technology, Tampere 33710, Finland

ABSTRACT: The effects of intermittent thin ITO layers on the water-splitting efficiency of α-Fe_2O_3 films grown by PECVD on FTO substrates are reported. The α-Fe_2O_3 was codoped with indium and tin by temperature-driven ionic transport and diffusion from the ultrathin ITO layer sputtered between the α-Fe_2O_3 layer and FTO substrate. The α-Fe_2O_3/ITO/FTO photoanodes showed a remarkable interdependence between the thickness of the ITO layer and PEC efficiency. Hematite photoanodes with a 32 nm thick ITO underlayer showed the highest photocurrent density of 2.5 mA cm^{-2}, corresponding to an approximate 3-fold enhancement over pristine α-Fe_2O_3 at 1.23 V vs RHE, whereas the thinner (8 nm) ITO underlayer yielded the lowest onset potential at 0.6 V vs RHE. Although the electrode with a thicker 72 nm ITO underlayer showed a higher onset potential of 0.9 V vs RHE, it still showed an enhancement in the photocurrent density at higher bias voltages. α-Fe_2O_3 was also deposited on metallic titanium substrates with intermittent sputtered tin and ITO layers. The codoping with indium and tin from ITO was observed to yield greatly enhanced performance when compared with both α-Fe_2O_3 alone and tin-doped α-Fe_2O_3. Transient absorption decays in the sub-nanosecond time scale were not affected by the doping, indicating that the doping had little effect on the primary charge carrier generation and recombination. On the other hand, fewer trapped electrons on the microsecond to millisecond time scale and a greatly increased amount of long-lived surface photoholes were observed for the ITO-doped samples. The transient absorption results imply that the large increases in photoelectrochemical efficiency were obtained due to higher electron mobility, which reduces recombination and leads to more efficient electron extraction from the electrodes.

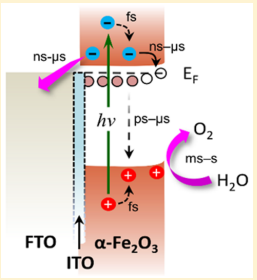

INTRODUCTION

Solar hydrogen produced by photoelectrochemical (PEC) splitting of water carries the potential of becoming an important pillar of the future energy economy based on renewable sources especially for decentralized small-scale applications, which explains the growing interest ever since the first observation made by Fujishima and Honda.[1] Hematite (α-Fe_2O_3) is a favorable candidate material as a water-splitting photoanode due to its earth abundance, low cost, high stability, narrow band gap of 2.0−2.2 eV,[2] high absorption capability, and environmentally benign impact. On the other hand, α-Fe_2O_3 does have intrinsic drawbacks, including a short hole diffusion length of 2−20 nm[3,4] and a valence band energy level that limits the hydrogen production reaction.[5] Several strategies have been adopted to overcome the intrinsic limitations of hematite, for instance, tuning of electrode morphology (nanoribbons, nanobelts, nanorods,[6−8] and mesoporous layers[9,10]), synergistic interfaces in two-dimensional stacks of semiconductors,[11] surface activation with electrocatalysts (e.g., Pt and Au),[12,13] and doping with various metal cations (Ca^{2+}, Mg^{2+}, Cu^{2+}, Zn^{2+}, Si^{4+}, Ge^{4+}, Ti^{4+}, Pt^{4+}, V^{5+}, and Nb^{5+}) to change the electronic structures.[12,14−23] Nanostructuring of the α-Fe_2O_3 thin film via various deposition techniques, such as chemical vapor deposition (CVD),[24] sol−gel,[25,26] electrospinning,[27,28] and plasma-enhanced chemical vapor deposition (PECVD),[29] can suppress the recombination processes, thereby increasing the number of photogenerated holes reaching the semiconductor−electrolyte interface and ultimately leading to a higher photocurrent density.

We report on the effects of codoping α-Fe_2O_3 thin films deposited by PECVD onto fluorine-doped tin oxide substrates (FTO) with indium and tin dopants. High temperature annealing was optimized to control tin diffusion into the hematite layer from the FTO substrate, which improves both photocurrent values and onset voltage. Indium and tin were codoped into α-Fe_2O_3 films grown on indium tin oxide (ITO) substrates followed by high temperature annealing; however, ITO conductivity degraded when annealed at temperatures above 500 °C. In this study, we were able to intentionally codope hematite with Sn and In by depositing a dc-sputtered overlayer of ITO on top of the FTO substrates before performing the hematite deposition. This step circumvented the voltage drop associated with the loss of conductivity when FTO was used alone. For a comparative analyses of the influence of intentional codoping with indium and tin through the sputtered ITO thin film, we also examined α-Fe_2O_3 films on

Received: October 16, 2016
Revised: November 13, 2016
Published: November 18, 2016

DOI: 10.1021/acs.jpcc.6b10432
J. Phys. Chem. C 2016, 120, 28345−28353

metallic titanium substrates with intermittent sputtered tin and ITO layers.

The effect of codopants on the charge carrier properties was monitored by ultrafast as well as long time scale transient absorption spectroscopy (TAS) studies. The transient absorption changes occurring upon laser excitation are useful in studying the evolution and transport of photogenerated charge carriers during their whole lifetime, spanning from picoseconds to seconds. TAS was shown to be a valuable tool in the study of both doped and pristine hematite photoanodes under working conditions and applied bias voltages.[11,30−38]

EXPERIMENTAL SECTION

Thin ITO layers were sputtered on FTO substrates using a solid target (Quorom TK8907) at 85 mA for varying times of deposition at a growth rate of 16 nm/min. Tin and ITO layers were sputtered also on metallic titanium substrates using the same parameters. The resulting double layer substrates were used as prepared. α-Fe_2O_3 films were deposited by radio-frequency PECVD using iron pentacarbonyl ($Fe(CO)_5$, Acros Organics) as the iron source and oxygen gas as the plasma source.[39] The as-grown amorphous films were annealed in air at 750 °C for 2 h followed by rapid quenching down to room temperature to obtain crystalline phases. The films prepared on metallic substrates were annealed at 750 °C for only 20 min to prevent the formation of thermally grown oxide on the titanium substrate.

The powder X-ray diffraction (XRD, STOE-STADI MP) patterns were measured in reflection mode using Cu Kα (λ = 0.154 06 nm) radiation. Scanning electron microscopy (SEM) was used to analyze the film morphology and thickness (FEI Nova Nano SEM 430). UV−visible absorption spectra were measured using a spectrophotometer in transmission mode (PerkinElmer Lambda 950). Photoelectrochemical (PEC) measurements were carried out in a three-electrode electrochemical cell with 1.0 M NaOH as the electrolyte using a potentiostat (PAR, Versa state IV) and a 150 W xenon lamp (Oriel) equipped with an AM1.5 filter to simulate the solar spectrum. X-ray photoelectron spectroscopy (XPS) measurements were carried out using a spectrometer (Φ 5600ci, PerkinElmer) at a pressure below 10^{-8} mbar under a non-monochromatic Al Kα excitation source (186.6 eV) with the help of ESCA M-Probe spectrometer (Surface Science Instruments SSI) with a pressure under 10^{-8} mbar. Correction to the binding energies was done in reference to the C 1s signal (284.8 eV). Spectral corrections and composition calculations were done with CasaXPS.

The transient absorption in the picoseconds to nanoseconds time scales was studied using the pump−probe method. The fundamental laser pulses of a Ti:sapphire laser (Libra F, Coherent Inc., 800 nm, ∼100 fs pulse width, repetition rate 1 kHz) were directed to an optical parametric amplifier (Topas C, Light Conversion Ltd.) to produce excitation pump pulses at 355 nm wavelength (about 0.5 mm beam diameter at the sample, attenuated to ∼1 mJ cm^{-2} with optical filters). About 10% of the fundamental laser beam energy was directed through a motorized translational stage to a Ti:sapphire crystal for white continuum generation of probe pulses. The probe pulses were split into two beams, used as reference and signal for the absorption change calculation. The detector system (ExciPro, CDP systems) was equipped with a Si CCD for measurements in the desired 500−725 nm wavelength range (range limited by sample absorption and Ti:sapphire fundamental, respectively). A chopper synchronized with the fundamental laser was used to block every second pump pulse. The measurements were averaged by taking 10 000 pulses per delay time and three consecutive scans over the whole measurement range.

The transient absorption in the microseconds to seconds time scales was studied using the flash-photolysis method. A Nd:YAG laser (LF117, Solar TII, 10 ns pulse width, 0.25 Hz repetition rate) was used to generate third harmonic (F015, Solar TII) at 355 nm wavelength used as excitation pump pulses (attenuated to 1.0 mJ cm^{-2}). A stabilized halogen lamp (SLS201/M, Thorlabs, 9 W) was used to provide the probe beam. The monochromatic (CM110, Digikröm) transient signal was detected with an amplified silicon photoreceiver (2051-FS, New Focus) and recorded on a digitizing oscilloscope (TDS3032B, Tektronix, 300 MHz). A flash photolysis control unit (mLFP-111, Luzchem) was used to manage the experiment. 30−80 decays were averaged for each measured wavelength, depending on the probe intensity and detector sensitivity.

RESULTS AND DISCUSSION

The thickness of sputtered ITO layers was monitored with a piezo crystal balance installed in the dc-sputter setup (Table 1),

Table 1. List of Used Photoanodes with Corresponding ITO and α-Fe_2O_3 Layer Thicknesses[a]

sample ID	ITO thickness (nm)	α-Fe_2O_3 thickness (nm)
Ref	0	100
IF30	8	100
IF120	32	100
IF300	72	100

[a]The α-Fe_2O_3 layer thickness was only measured for the reference sample but is expected to be the same for all samples prepared in the same experimental run.

while the surface morphology and thickness of the deposited pristine α-Fe_2O_3 and indium and tin codoped α-Fe_2O_3 thin films were characterized through SEM analyses (Figure 1). The sample notation and layer thicknesses of the samples prepared on FTO substrates are presented in Table 1.

A distinctive shift in the morphology of doped and undoped α-Fe_2O_3 thin films was observed (Figure 1). Whereas the undoped films were made of uniform spherical particles, a denser and coarse-grained morphology was observed in doped samples.[40,41] The thicknesses of pristine α-Fe_2O_3 (ref, 100 nm) and codoped ITO/α-Fe_2O_3 (IF120, 113 nm) were measured using cross-sectional SEM images (Figures 1c and 1d). The sum of individual as-deposited α-Fe_2O_3 (100 nm) and ITO (32 nm) layers was found to be larger than the total thickness of the annealed double layer (IF120; 113 nm). This decrease in total thickness in the codoped IF120 sample can be explained by the temperature-driven diffusion of indium oxide (In_2O_3) and tin oxide (SnO_2) into the iron oxide (α-Fe_2O_3) film, resulting in the codoping of the deposited hematite layer and densification of the sandwich layers.

The phase composition of the deposited thin films through XRD analysis (Figure 2a) confirmed the presence of hematite (33-0664). The observed peaks at 2θ = 24°, 33°, 36°, and 74° were indexed to the α-Fe_2O_3 crystal planes at (012), (104), (110), and (220), respectively. Furthermore, ITO peaks were indexed from the XRD patterns reported by Son et al.[42]

DOI: 10.1021/acs.jpcc.6b10432
J. Phys. Chem. C 2016, 120, 28345−28353

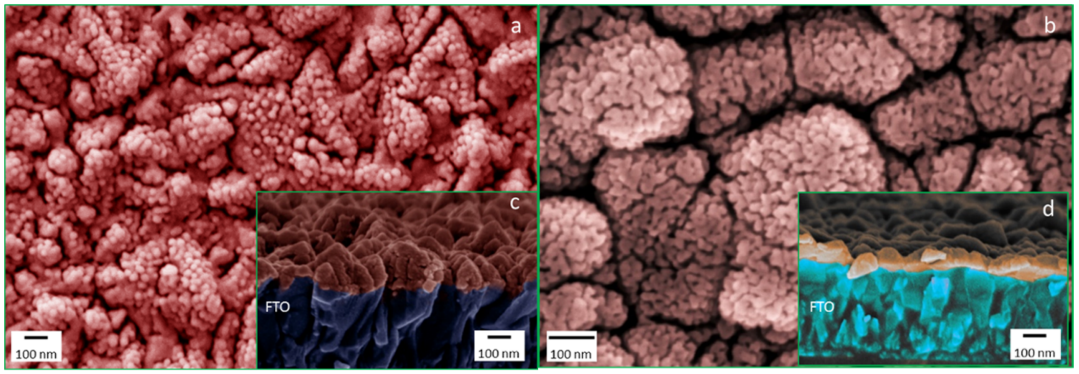

Figure 1. SEM images of (a) α-Fe_2O_3 (ref), (b) codoped α-Fe_2O_3 (IF120), and cross sections of (c) α-Fe_2O_3 (ref) and (d) codoped α-Fe_2O_3 (IF120).

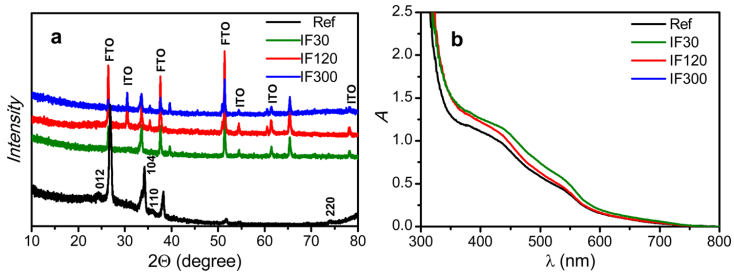

Figure 2. (a) XRD patterns and (b) UV−vis spectra of reference and codoped α-Fe_2O_3 films.

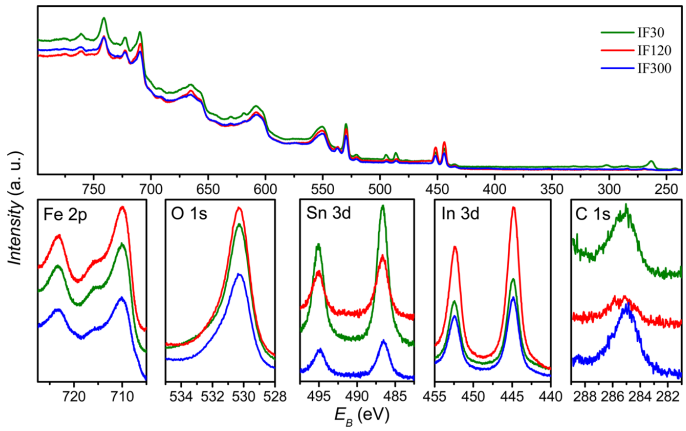

Figure 3. XPS survey of codoped α-Fe_2O_3 thin films with different ITO sputtering times.

Absorption spectra of the deposited samples were determined using UV−vis spectroscopy (Figure 2b). The absorbances of the different α-Fe_2O_3 layers are rather close to each other, which indicates that the α-Fe_2O_3 layer thickness remains uniform independent of the thickness of the ITO underlayer. The small variation in the layer absorption is presumably caused by the differential diffusion kinetics that can lead to phase boundaries (α-Fe_2O_3|SnO_2|In_2O_3) of variable thickness (Figure 1). The effect of the thickness of the underlying ITO layer on the photoanode composition was investigated by systematic XPS measurements (Figure 3) to reveal the chemical environments around different various metal centers.

The lowest carbon content observed in sample IF120 partially (Table 2) explains the high photocurrent density (2.51 mA cm^{-2} at 1.23 V vs RHE) seen in the current density−voltage (J−V) measurements (Figure 4). Carbon contamination reduces conductivity in iron oxide films due to the

DOI: 10.1021/acs.jpcc.6b10432
J. Phys. Chem. C 2016, 120, 28345−28353

Table 2. Elemental Composition Calculated from XPS Plots

sample	Fe 3p	O 1s	Sn 3d	In 3d	C 1s
IF30	30.76	52.57	1.33	5.65	9.69
IF120	37.74	50.88	0.53	10.7	0.14
IF300	29.9	53.04	0.55	7.62	6.88

formation of iron carbides.[43] The higher content of tin in the IF30 sample results from the diffusion of tin from the FTO substrate during annealing procedure.

While the IF120 and IF300 samples exhibited lower tin content due to the thicker ITO underlayer acting as a buffer zone for tin diffusion (ITO is a mixture of tin and indium oxides with approximately 10 wt % Sn/In ratio, whereas FTO is mainly fluorine-doped tin oxide). The significant cathodic shift of 150 mV in the onset potential in IF30 (0.60 V vs RHE), when compared with the reference sample (0.75 V vs RHE), is due to the higher tin content of the photoanode, even though the work function of ITO is slightly larger than that of FTO (see Figure 5 for work functions of the materials). This work function difference should inhibit electron flow from ITO to FTO; however, this effect is extremely small when the two materials are both conductors, the electrode is under external anodic bias voltage, and the ITO layer thickness remains small. An increase in the tin (Sn^{4+}) doping level leads to an increase in the formation of Fe^{2+} sites[44,45] through reduction of Fe^{3+} during the annealing process in order to maintain net charge neutrality,[46] leading to an increase in the conductivity of hematite due to the polaron hopping mechanism (between consecutive Fe^{2+} sites).[47] On the other hand, the Fe^{2+} sites can act as scattering centers when the SnO_2 concentration is above 1 mol %, decreasing conductivity and increasing charge carrier recombination at higher concentrations. However, hematite layers with even larger SnO_2 concentrations than 1 mol % still exhibit an increase in the electrical conductance compared to pure hematite layers.[44]

Both the reference and IF30 samples are composed of over 1 mol % SnO_2 according to the XPS results (Table 2), indicating that charge scattering is the main reason for the lower photocurrents observed for these samples. The higher photocurrent density displayed by sample IF120 can be related to the higher indium content of the material, which is thought to decrease the charge carrier recombination rate of the photoanode by the introduction of In^{3+} ions. The increase in trivalent dopant ion concentration in the hematite layer leads to a decrease in the concentration of Fe^{2+} sites and consequently to a decrease in the number of charge carrier recombination.

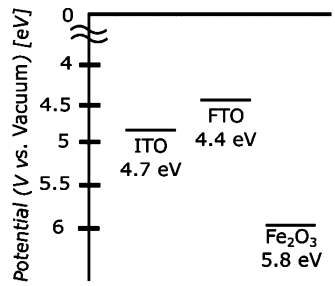

Figure 5. Work functions of used substrates and metal oxides.[50]

Since the ITO layer is composed of less SnO_2 than the FTO layer, a lower amount of tin is diffused into the hematite layer, thus lowering the occurrence of scattering events. The increases observed in the onset potential with thicker sputtered ITO layers are due to the loss of conductivity in the ITO layer during high temperature annealing in the presence of oxygen (air). This oxygen-rich annealing atmosphere at high temperatures (750 °C) leads to the trapping of Sn donors in the so-called Frank−Köstlin associate, reducing the overall conductance of the material.[48,49]

The tin doping of the PECVD deposited α-Fe_2O_3 through migration of tin ions from the FTO substrate during annealing was eliminated by depositing thin films of tin metal and ITO on a metallic titanium substrate. The growth of a TiO_2 underlayer via thermal oxidation of the titanium substrate was prohibited by using a flash annealing process. The improved PEC performance of the samples (Figure 6) displayed the enhancing

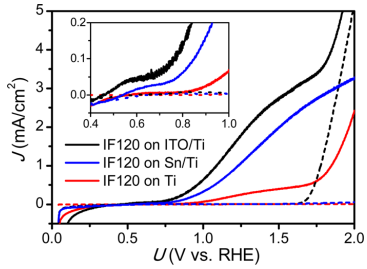

Figure 6. Photocurrent density−voltage curves of reference α-Fe_2O_3, tin-doped α-Fe_2O_3, and codoped α-Fe_2O_3 on titanium substrates; inset plot shows the change in onset potential of the different samples.

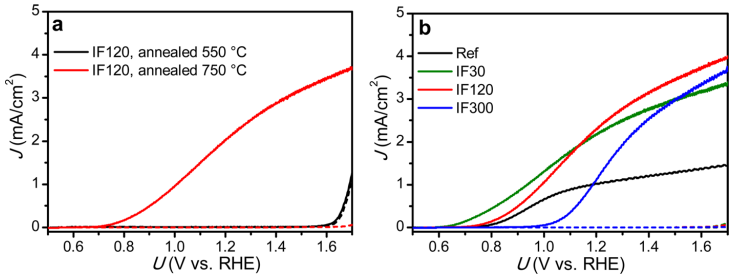

Figure 4. Photocurrent density−voltage curves of (a) α-Fe_2O_3 annealed at different temperatures showing the effect of codoping achieved only at high annealing temperatures and (b) codoped α-Fe_2O_3 with different ITO layer thicknesses.

DOI: 10.1021/acs.jpcc.6b10432
J. Phys. Chem. C 2016, 120, 28345−28353

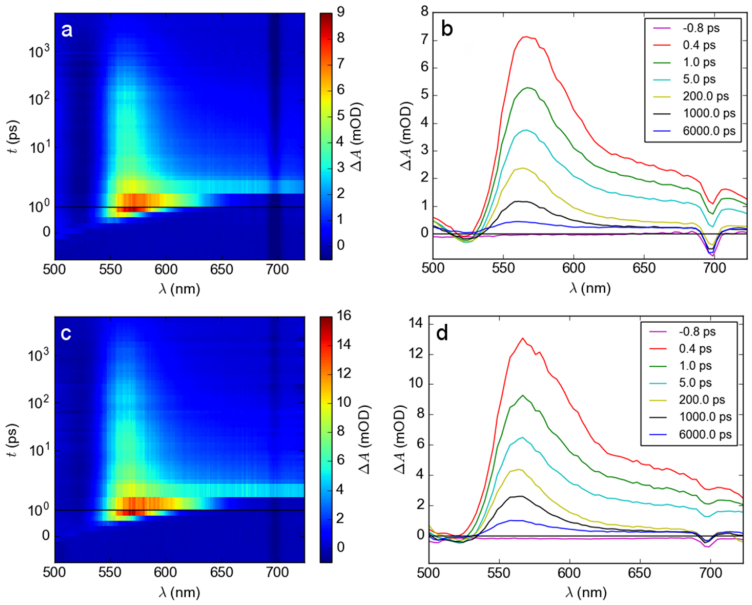

Figure 7. Time-resolved absorption spectra of (a, b) α-Fe_2O_3 and (c, d) codoped α-Fe_2O_3 (IF120). The color maps (a) and (c) are not corrected for group velocity dispersion, whereas the spectra at different delay times in (c) and (d) are corrected. The time scales in (a) and (c) are linear up to 1 ps delay time, indicated with a solid black line, and logarithmic for longer delay times.

effect of codoping with In/Sn over doping with Sn. A cathodic shift of 100 mV can be seen in the codoped sample compared to the tin-doped sample, in addition to an increase in photocurrent density over the whole voltage range with a maximum of over 3 mA cm^{-2} at 1.7 V vs RHE.

To gain insight into the effects the sputtered ITO layer has on the charge transport and recombination processes, we used the TAS measurements. All TAS experiments were performed under water-splitting conditions in a three-electrode photoelectrochemical cell with a constant applied bias of 1.23 V vs RHE.

On the picoseconds−nanoseconds time scale both reference hematite and IF120 featured broad transient absorption spectra centered on a positive absorption change located just above the band gap at 555−575 nm (Figure 7). The bleaching of the signal (negative change in absorption) below 550 nm is due to a decrease in the ground state absorption, whereas the strong bleach visible around 700 nm (dark blue) is due to scattered light originating from the optical parametric amplifier. The positive absorption and ground state bleach both have similar multiexponential decay dynamics. The positive absorption showed a fast initial decay in the picoseconds time scale that matches the formation half-life of the bleach signal, whereas the longer-lived decays of both features last up to the nanoseconds time scale. The fast decay phase in the picoseconds time scale corresponded to the relaxation of hot electrons, after which the recombination, trapping, and charge transport processes inherent to the material begin.

The TAS decays of the reference and IF120 are virtually the same in the picoseconds−nanoseconds time scales, as can be seen in the normalized TAS decays at a probe wavelength of 565 nm (Figure 8). Taken together with the great similarity of the spectra shown in Figure 7, this illustrated that the primary

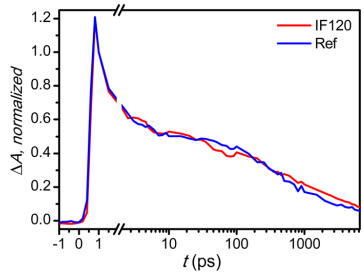

Figure 8. Normalized TAS decays in the subpicosecond to nanosecond time scale of referenceand codoped α-Fe_2O_3 (IF120).

recombination and charge transport dynamics of the hematite layer are not greatly affected by the ITO underlayer, although differences in sample conductivity can show up on the nanosecond and longer time scales.

In the microseconds to seconds time scale the TAS decays have two distinct exponential components for both IF120 and reference hematite, as shown in Figure 9 at a probe wavelength of 580 nm. On this time scale the TAS signal at 580 nm is composed of the signal originating from filled (reduced) trap states[35,37] as well as the signal originating from the photogenerated surface holes. The filled trap states cause a negative component in the transient absorption due to reduced ground state absorption, with exponential lifetimes of 1.8 and 3.0 ms for reference and IF120, respectively (Figure 9a). The bleach recovery is assigned to the removal of trapped electrons into the external circuit.[37] After the recovery, a long-lived exponential decay component remains with similar lifetimes of 360 and 310 ms for IF120 and reference hematite,

DOI: 10.1021/acs.jpcc.6b10432
J. Phys. Chem. C 2016, 120, 28345−28353

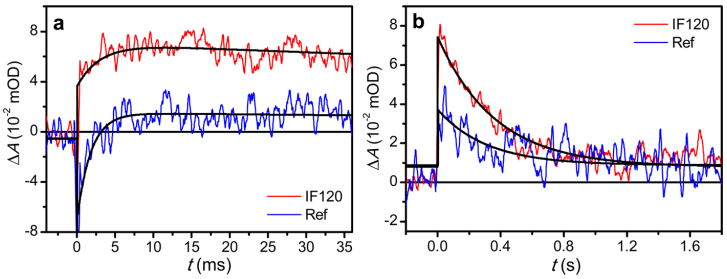

Figure 9. TAS decays in the (a) microseconds to (b) seconds time scales of reference and codoped α-Fe_2O_3 (IF120) at 580 nm. Solid lines show the (a) biexponential and (b) single-exponential fits to raw data, whereas the colored dashed lines present the raw data smoothed with a 20 point Savitzky−Golay filter.

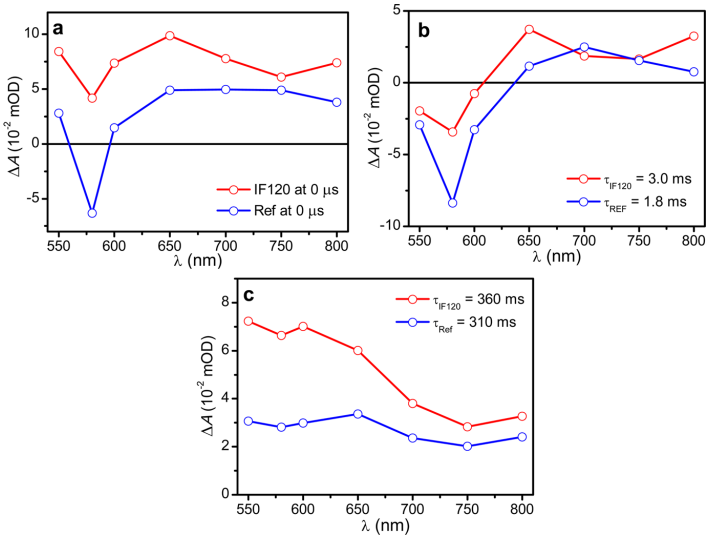

Figure 10. Decay component spectra in the microseconds to seconds time scales of reference and codoped α-Fe_2O_3 (IF120). (a) Sum component spectrum, representing the amplitude after excitation. (b) Decay component spectrum with a lifetime in the millisecond time scale. (c) Decay component spectrum with a lifetime in the 300−400 ms range.

respectively (Figure 9b), assigned to the reaction of surface holes with surface bound hydroxyl species as well as back electron recombination.[36]

The measured raw decays were fitted with a biexponential function of the form

$$\Delta A(t, \lambda) = \Delta A_1(\lambda)e^{-\tau_1/t} + \Delta A_2(\lambda)e^{-\tau_2/t} \quad (1)$$

where $\Delta A(t,\lambda)$ is the measured change in absorption with respect to time, t, and wavelength, λ, $\Delta A_1(\lambda)$ and $\Delta A_2(\lambda)$ are the amplitudes of the separate exponential components at wavelength λ, and τ_1 and τ_2 are the exponential lifetimes of the components. The fitting was performed globally for all measured wavelengths to enable the spectral deconvolution of the decay components. The time-resolved spectrum after excitation is obtained as the sum of the amplitudes of the two components (Figure 10a), whereas the individual components can be presented as separate decay component spectra (Figures 10b and 10c).

The millisecond decay component spectrum for both samples (Figure 10b) illustrates clearly the localized nature of the fast bleach component in the wavelength range between 550 and 600 nm, with maximum bleach at 580 nm. The lifetime of the bleaching recovery is slightly faster for reference α-Fe_2O_3 than for IF120, but this is presumably due to the limited coverage of the measurement setup in the nanoseconds to microseconds time scale. However, it is clearly evident that more trapped electrons remain in the reference α-Fe_2O_3 in the measured time scale, with over 2 times larger bleach amplitude in the decay component spectra (Figure 10b).

The long-lived decay component's lifetime and spectrum (Figure 10c) match those we have previously obtained for long-lived holes in hematite[38] for both reference α-Fe_2O_3 and IF120. The lifetimes for the long-lived holes are similar for both samples, indicating that no increases in the catalytic efficiency are observed for the codoped sample. However, the signal attributed to surface holes is over twice as large for IF120 than for reference α-Fe_2O_3. Thus, a much larger number of

DOI: 10.1021/acs.jpcc.6b10432
J. Phys. Chem. C 2016, 120, 28345−28353

photogenerated surface holes remain in IF120 after electron−hole recombination and electron extraction processes have occurred. This indicates a greatly reduced amount of recombination on the submillisecond time scale. Taken together with the reduced number of trapped electrons remaining in the millisecond time scale in IF120, the greater amount of photoholes is a clear indication that the electrons are more efficiently removed from the ITO-doped photoanodes. These processes are illustrated in Scheme 1 along with the

Scheme 1. Illustration of the Electron and Hole Transfer Processes in Reference and Codoped α-Fe_2O_3 over ITO[a]

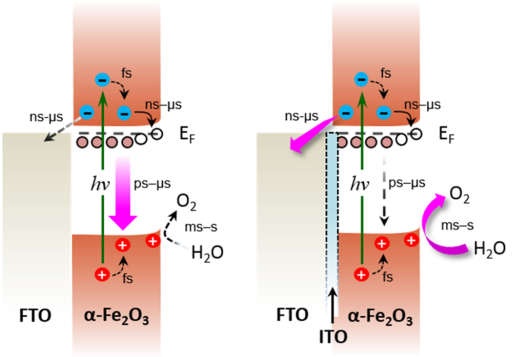

[a]The lifetimes of the processes were similar for both samples. However, the larger number of long-lived ms−s time scale surface holes in the codoped sample indicates both reduced recombination in the ns−μs time scale and increased photoelectrochemical performance due to increased electron extraction. The dashed and magenta arrows indicate the magnitudes of the processes, occurring either weakly or strongly, respectively.

associated time ranges at which they occur, showing more efficient electron extraction and reduced recombination in the codoped sample that lead to an increased photoelectrochemical efficiency due to a larger amount of long-lived surface holes.

CONCLUSION

Indium and tin codoping of hematite photoanodes showed superior photoactivity and enhancement in both photocurrent densities and onset potential over Sn-doped hematite. The enhancing effect of In and Sn codoping is mainly due to improved electron mobility that reduces recombination in the nanoseconds to microseconds time scale as confirmed by transient absorption measurements. The improved mobility of charge carriers is possibly due to redox processes (Fe^{2+}/Fe^{3+}) that can be influenced by trivalent In and tetravalent Sn centers that alter charge neutrality in the hematite matrix. Consequently, a greatly increased number of photoholes reach the surface of the photoanode in order to augment the water-splitting reactions in the milliseconds to seconds time scale. On the other hand, the primary recombination processes in the picoseconds to nanoseconds time scale were not affected by the implementation of an ITO underlayer and the following indium doping. These findings show that the photoelectrochemical performance of hematite can be largely influenced by introducing intermediate layers of transparent conducting substrate and can be greatly increased by using a simple dopant deposition procedure at the metal oxide and substrate interface, which demonstrate an effective strategy for circumventing the intrinsic limitations of hematite.

AUTHOR INFORMATION

Corresponding Author

*E-mail sanjay.mathur@uni-koeln.de (S.M.).

ORCID

Yakup Gönüllü: 0000-0001-9708-9846

Present Address

A.K.: Institute of Materials Physics in Space, German Aerospace Center (DLR), Cologne 51170, Germany.

Author Contributions

A.K. and T.-P.R. contributed equally.

Funding

The work was financially supported by SOLAROGENIX, Project (EC-FP7-Grant Agreement No. 214281), and the University of Cologne.

Notes

The authors declare no competing financial interest.

ACKNOWLEDGMENTS

A.K. and S.M. are thankful to the Lebanese National Council for Scientific Research for providing a fellowship to Mr. Ali Kaouk. The authors are thankful to Dr. Selina Olthof for XPS measurement and Mr. Ashish Lepcha for XRD measurement.

ABBREVIATIONS

TAS, transient absorption spectroscopy; XPS, X-ray photoelectron spectroscopy; XRD, X-ray diffraction.

REFERENCES

(1) Fujishima, A.; Honda, K. Electrochemical Photolysis of Water at a Semiconductor Electrode. *Nature* **1972**, *238*, 37−38.

(2) Bailey, P.C. J. Absorption and Reflectivity Measurements on Some Rare Earth Iron Garnets and α-Fe_2O_3. *J. Appl. Phys.* **1960**, *31*, S39.

(3) Dare-Edwards, M. P.; Goodenough, J. B.; Hamnett, A.; Trevellick, P. R. Electrochemistry and Photoelectrochemistry of Iron(III) Oxide. *J. Chem. Soc., Faraday Trans. 1* **1983**, *79*, 2027−2041.

(4) Gardner, R. F. G.; Sweett, F.; Tanner, D. W. The Electrical Properties of Alpha Ferric Oxide—II.: Ferric Oxide of High Purity. *J. Phys. Chem. Solids* **1963**, *24*, 1183−1196.

(5) Walter, M. G.; Warren, E. L.; McKone, J. R.; Boettcher, S. W.; Mi, Q.; Santori, E. A.; Lewis, N. S. Solar Water Splitting Cells. *Chem. Rev.* **2010**, *110*, 6446−6473.

(6) Beermann, N.; Vayssieres, L.; Lindquist, S. E.; Hagfeldt, A. J. Photoelectrochemical Studies of Oriented Nanorod Thin Films of Hematite. *J. Electrochem. Soc.* **2000**, *147*, 2456−2461.

(7) Lindgren, T.; Wang, H. L.; Beermann, N.; Vayssieres, L.; Hagfeldt, A.; Lindquist, S. E. Aqueous Photoelectrochemistry of Hematite Nanorod Array. *Sol. Energy Mater. Sol. Cells* **2002**, *71*, 231−243.

(8) Wu, C.; Yin, P.; Zhu, X.; OuYang, C. Z.; Xie, Y. J. Synthesis of Hematite (α-Fe_2O_3) Nanorods: Diameter-Size and Shape Effects on Their Applications in Magnetism, Lithium Ion Battery, and Gas Sensors. *J. Phys. Chem. B* **2006**, *110*, 17806−17812.

(9) Brezesinski, T.; Groenewolt, M.; Antonietti, M.; Smarsly, B. Crystal-to-Crystal Phase Transition in Self-Assembled Mesoporous Iron Oxide Films. *Angew. Chem., Int. Ed.* **2006**, *45*, 781−784.

(10) Prakasam, H. E.; Varghese, O. K.; Paulose, M.; Mor, G. K.; Grimes, C. A. Synthesis and Photoelectrochemical Properties of Nanoporous Iron (III) Oxide by Potentiostatic Anodization. *Nanotechnology* **2006**, *17*, 4285−4291.

DOI: 10.1021/acs.jpcc.6b10432
J. Phys. Chem. C 2016, 120, 28345−28353

(11) Barreca, D.; Carraro, G.; Gasparotto, A.; Maccato, C.; Warwick, M. E. A.; Kaunisto, K.; Sada, C.; Turner, S.; Gönüllü, Y.; Ruoko, T.-P.; et al. Water Splitting: Fe_2O_3−TiO_2 Nano-heterostructure Photoanodes for Highly Efficient Solar Water Oxidation. *Adv. Mater. Interfaces* **2015**, *2*, 1500313−1−11.
(12) Sartoretti, C. J.; Alexander, B. D.; Solarska, R.; Rutkowska, I. A.; Augustynski, J.; Cerny, R. J. Photoelectrochemical Oxidation of Water at Transparent Ferric Oxide Film Electrodes. *J. Phys. Chem. B* **2005**, *109*, 13685−13692.
(13) Watanabe, A.; Kozuka, H. J. Photoanodic Properties of Sol−Gel-Derived Fe_2O_3 Thin Films Containing Dispersed Gold and Silver Particles. *J. Phys. Chem. B* **2003**, *107*, 12713−12720.
(14) Murphy, A. B.; Barnes, P. R. F.; Randeniya, L. K.; Plumb, I. C.; Grey, I. E.; Horne, M. D.; Glasscock, J. A. Efficiency of solar water splitting using semiconductor electrodes. *Int. J. Hydrogen Energy* **2006**, *31*, 1999−2017.
(15) Mohanty, S.; Ghose, J. Studies on some α-Fe_2O_3 photoelectrodes. *J. Phys. Chem. Solids* **1992**, *53*, 81−91.
(16) Glasscock, J. A.; Barnes, P. R. F.; Plumb, I. C.; Savvides, N. Enhancement of Photoelectrochemical Hydrogen Production from Hematite Thin Films by the Introduction of Ti and Si. *J. Phys. Chem. C* **2007**, *111*, 16477−16488.
(17) Arai, T.; Konishi, Y.; Iwasaki, Y.; Sugihara, H.; Sayama, K. High-Throughput Screening using Porous Photoelectrode for the Development of Visible-Light-Responsive Semiconductors. *J. Comb. Chem.* **2007**, *9*, 574−581.
(18) Shinar, R.; Kennedy, J. H. Photoactivity of Doped α-Fe_2O_3 Electrodes. *Sol. Energy Mater.* **1982**, *6*, 323−335.
(19) Leygraf, C.; Hendewerk, M.; Somorjai, G. A. Photodissociation of Water by p- and n-Type Polycrystalline Iron Oxides by using Visible Light ($\leq$2.7 eV) in the Absence of External Potential. *Proc. Natl. Acad. Sci. U. S. A.* **1982**, *79*, 5739−5741.
(20) Turner, J. E.; Hendewerk, M.; Parmeter, J.; Neiman, D.; Somorjai, G. A. The Characterization of Doped Iron Oxide Electrodes for the Photodissociation of Water Stability, Optical, and Electronic Properties. *J. Electrochem. Soc.* **1984**, *131*, 1777−1783.
(21) Khader, M. M.; Vurens, G. H.; Kim, I. K.; Salmeron, M.; Somorjai, G. A. Photoassisted Catalytic Dissociation of H_2O to Produce Hydrogen on Partially Reduced α-Fe_2O_3. *J. Am. Chem. Soc.* **1987**, *109*, 3581−3585.
(22) Duret, A.; Grätzel, M. Visible Light-Induced Water Oxidation on Mesoscopic α-Fe_2O_3 Films Made by Ultrasonic Spray Pyrolysis. *J. Phys. Chem. B* **2005**, *109*, 17184−17191.
(23) Aroutiounian, V. M.; Arakelyan, V. M.; Shahnazaryan, G. E.; Stepanyan, G. M.; Khachaturyan, E. A.; Wang, H.; Turner, J. A. Photoelectrochemistry of Semiconductor Electrodes Made of Solid Solutions in the System Fe_2O_3−Nb_2O_5. *Sol. Energy* **2006**, *80*, 1098−1111.
(24) Mathur, S.; Veith, M.; Sivakov, V.; Shen, H.; Huch, V.; Hartmann, U.; Gao, H.-B. Phase-Selective Deposition and Microstructure Control in Iron Oxide Films Obtained by Single-Source CVD. *Chem. Vap. Deposition* **2002**, *8*, 277−283.
(25) Wu, N. L.; Wang, S.; Rusakova, I. A. Inhibition of Crystallite Growth in the Sol-Gel Synthesis of Nanocrystalline Metal Oxides. *Science* **1999**, *285*, 1375−1377.
(26) Gash, A. E.; Tillotson, T. M.; Satcher, J. H., Jr.; Poco, J. F.; Hrubesh, L. W.; Simpson, R. L. Use of Epoxides in the Sol−Gel Synthesis of Porous Iron(III) Oxide Monoliths from Fe(III) Salts. *Chem. Mater.* **2001**, *13*, 999−1007.
(27) Macías, M.; Chacko, A.; Ferraris, J. P.; Balkus, K. J., Jr. Electrospun Mesoporous Metal Oxide Fibers. *Microporous Mesoporous Mater.* **2005**, *86*, 1−13.
(28) Kim, I. D.; Rothschild, A. Nanostructured Metal Oxide Gas Sensors Prepared by Electrospinning. *Polym. Adv. Technol.* **2011**, *22*, 318−325.
(29) Mathur, S.; Ruegamer, T.; Donia, N.; Shen, H. Functional Metal Oxide Coatings by Molecule-Based Thermal and Plasma Chemical Vapor Deposition Techniques. *J. Nanosci. Nanotechnol.* **2008**, *8*, 2597−2603.
(30) Pendlebury, S. R.; Barroso, M.; Cowan, A. J.; Sivula, K.; Tang, J.; Grätzel, M.; Klug, D. R.; Durrant, J. R. Dynamics of Photogenerated Holes in Nanocrystalline α-Fe_2O_3 Electrodes for Water Oxidation Probed by Transient Absorption Spectroscopy. *Chem. Commun.* **2011**, *47*, 716−718.
(31) Pendlebury, S. R.; Cowan, A. J.; Barroso, M.; Sivula, K.; Ye, J.; Grätzel, M.; Klug, D. R.; Tang, J.; Durrant, J. R. Correlating Long-Lived Photogenerated Hole Populations with Photocurrent Densities in Hematite Water Oxidation Photoanodes. *Energy Environ. Sci.* **2012**, *5*, 6304−6312.
(32) Barroso, M.; Cowan, A. J.; Pendlebury, S. R.; Grätzel, M.; Klug, D. R.; Durrant, J. R. The Role of Cobalt Phosphate in Enhancing the Photocatalytic Activity of α-Fe_2O_3 toward Water Oxidation. *J. Am. Chem. Soc.* **2011**, *133*, 14868−14871.
(33) Barroso, M.; Mesa, C. A.; Pendlebury, S. R.; Cowan, A. J.; Hisatomi, T.; Sivula, K.; Grätzel, M.; Klug, D. R.; Durrant, J. R. Dynamics of Photogenerated Holes in Surface Modified α-Fe_2O_3 Photoanodes for Solar Water Splitting. *Proc. Natl. Acad. Sci. U. S. A.* **2012**, *109*, 15640−15645.
(34) Cowan, A. J.; Durrant, J. R. Long-Lived Charge Separated States in Nanostructured Semiconductor Photoelectrodes for the Production of Solar Fuels. *Chem. Soc. Rev.* **2013**, *42*, 2281−2293.
(35) Barroso, M.; Pendlebury, S. R.; Cowan, A. J.; Durrant, J. R. Charge Carrier Trapping, Recombination and Transfer in Hematite (α-Fe_2O_3) Water Splitting Photoanodes. *Chem. Sci.* **2013**, *4*, 2724−2734.
(36) Le Formal, F.; Pendlebury, S. R.; Cornuz, M.; Tilley, S.; Grätzel, M.; Durrant, J. R. Back Electron−Hole Recombination in Hematite Photoanodes for Water Splitting. *J. Am. Chem. Soc.* **2014**, *136*, 2564−2574.
(37) Pendlebury, S. R.; Wang, X.; Le Formal, F.; Cornuz, M.; Kafizas, A.; Tilley, S.; Grätzel, M.; Durrant, J. R. Ultrafast Charge Carrier Recombination and Trapping in Hematite Photoanodes under Applied Bias. *J. Am. Chem. Soc.* **2014**, *136*, 9854−9857.
(38) Ruoko, T.-P.; Kaunisto, K.; Bärtsch, M.; Pohjola, J.; Hiltunen, A.; Niederberger, M.; Tkachenko, N. V.; Lemmetyinen, H. Subpicosecond to Second Time-Scale Charge Carrier Kinetics in Hematite−Titania Nanocomposite Photoanodes. *J. Phys. Chem. Lett.* **2015**, *6*, 2859−2864.
(39) Singh, A. P.; Mettenbörger, A.; Golus, P.; Mathur, S. Photoelectrochemical Properties of Hematite Films Grown by Plasma Enhanced Chemical Vapor Deposition. *Int. J. Hydrogen Energy* **2012**, *37*, 13983−13988.
(40) Kim, J.; Magesh, G.; Youn, D. H.; Kubota, J.; Kazunari, D.; Lee, J. S. Single-crystalline, wormlike hematite photoanodes for efficient solar water splitting. *Sci. Rep.* **2013**, *3*, 2681.
(41) Emin, S.; de Respinis, M.; Mavric, T.; Dam, B.; Valant, M.; Smith, W. A. Photoelectrochemical water splitting with porous α-Fe_2O_3 thin films prepared from Fe/Fe-oxide nanoparticles. *Appl. Catal., A* **2016**, *523*, 130.
(42) Son, P. K.; Choi, S.-W.; Kim, S. S. Indium Tin Oxide Exhibiting High Poly-Crystallinity on Oxygen Plasma-Treated Polyethylene Terephthalate Surface. *Nanoscale Res. Lett.* **2012**, *7*, 118−121.
(43) Kaouk, A.; Ruoko, T.-P.; Gönüllü, Y.; Kaunisto, K.; Mettenbörger, A.; Gurevich, E.; Lemmetyinen, H.; Ostendorf, A.; Mathur, S. Graphene-Intercalated Fe_2O_3/TiO_2 Heterojunctions for Efficient Photoelectrolysis of Water. *RSC Adv.* **2015**, *5*, 101401−101407.
(44) Zhang, M.; Luo, W.; Li, Z.; Yu, T.; Zou, Z. Improved Photoelectrochemical Responses of Si and Ti Codoped α-Fe_2O_3 Photoanode Films. *Appl. Phys. Lett.* **2010**, *97*, 042105−1−3.
(45) Iordanova, N.; Dupuis, M.; Rosso, K. M. Charge Transport in Metal Oxides: a Theoretical Study of Hematite α-Fe_2O_3. *J. Chem. Phys.* **2005**, *122*, 144305.
(46) Yang, T.-Y.; Kang, H.-Y.; Sim, U.; Lee, Y.-J.; Lee, J.-H.; Koo, B.; Nam, K. T.; Joo, Y.-C. A New Hematite Photoanode Doping Strategy for Solar Water Splitting: Oxygen Vacancy Generation. *Phys. Chem. Chem. Phys.* **2013**, *15*, 2117−2124.

DOI: 10.1021/acs.jpcc.6b10432
J. Phys. Chem. C 2016, 120, 28345−28353

(47) Aroutiounian, V. M.; Trakelyan, V. M.; Shanazayan, G. E.; Hoinannisyan, H. R.; Wang, H.; Tuner, G. A. Photoelectrochemistry of Tin-Doped Iron Oxide Electrodes. *Sol. Energy* **2007**, *81*, 1369−1376.
(48) Klein, A.; Körber, C.; Wachau, A.; Säuberlich, F.; Gassenbauer, Y.; Harvey, S. P.; Proffit, D. E.; Mason, T. O. Transparent Conducting Oxides for Photovoltaics: Manipulation of Fermi Level, Work Function and Energy Band Alignment. *Materials* **2010**, *3*, 4892−4914.
(49) Frank, G.; Köstlin, H. Electrical Properties and Defect Model of Tin-Doped Indium Oxide Layers. *Appl. Phys. A: Solids Surf.* **1982**, *27*, 197−206.
(50) Schlaf, R.; Murata, H.; Kafafi, Z. H. Work Function Measurements on Indium Tin Oxide Films. *J. Electron Spectrosc. Relat. Phenom.* **2001**, *120*, 149−154.

DOI: 10.1021/acs.jpcc.6b10432
J. Phys. Chem. C 2016, 120, 28345−28353

Tampereen teknillinen yliopisto
PL 527
33101 Tampere

Tampere University of Technology
P.O.B. 527
FI-33101 Tampere, Finland

ISBN 978-952-15-3951-0
ISSN 1459-2045